Distribution Agreement

In presenting this thesis or dissertation as a partial fulfillment of the requirements for an advanced degree from Emory University, I hereby grant to Emory University and its agents the non-exclusive license to archive, make accessible, and display my thesis or dissertation in whole or in part in all forms of media, now or hereafter known, including display on the world wide web. I understand that I may select some access restrictions as part of the online submission of this thesis or dissertation. I retain all ownership rights to the copyright of the thesis or dissertation. I also retain the right to use in future works (such as articles or books) all or parts of this thesis or dissertation.

Signature:

_____ _____

Jessica Hernández Guzmán Date

^{14}N electron spin echo envelope modulation Spectroscopy of Cu(II)-imidazole coordination structure in the amyloid-β protein of Alzheimer's disease and in model Aβ peptides and complexes

By
Jessica Hernández Guzmán
Doctor of Philosophy
Physics

_____
Prof. Kurt Warncke
Advisor

_____
Prof. Laura Finzi
Committee Member

_____
Prof. David G. Lynn
Committee Member

_____
Prof. Ivan Rasnik
Committee Member

_____
Prof. Eric R. Weeks
Committee Member

Accepted:

_____

Lisa A. Tedesco, Ph. D.
Dean of the James T. Laney School of Graduate Studies

_____
Date

^{14}N Electron Spin Echo Envelope Modulation Spectroscopy of Cu(II)-Imidazole Coordination Structure in the Amyloid-β protein of Alzheimer's Disease and in Model Aβ Peptides and Complexes

By

Jessica Hernández Guzmán

B.A., Hollins University, Roanoke 2004

Advisor: Kurt Warncke, Ph. D.

An abstract of
A dissertation submitted to the Faculty of the
James T. Laney School of Graduate Studies of Emory University
in partial fulfillment of the requirements for the degree of
Doctor of Philosophy

2010

Abstract

^{14}N Electron Spin Echo Envelope Modulation Spectroscopy of Cu(II)-Imidazole Coordination Structure in the Amyloid-β protein of Alzheimer's Disease and in Model Aβ Peptides and Complexes

By **Jessica Hernández Guzmán**

Aggregation and fibrillization of the amyloid-β (Aβ) protein and deposition in the form of plaques are the hallmarks of Alzheimer's disease. The coordination of Cu(II) by Aβ has been proposed to play a role in these processes. To gain insight into factors that govern fibrillization, electron paramagnetic resonance and electron spin echo envelope modulation (ESEEM) spectroscopies have been used to reveal features of the molecular structure of the Cu(II)- imidazole coordination in cryotrapped soluble and fibrillar forms of Aβ peptides [Aβ(1-40), Aβ(1-16), Aβ(13-21)] and model complexes [Cu(II)-diethylenetriamine 2-methylimidazole, Cu(II)-bis-histamine-bis-nitrate, Cu(II)-bis-(acetate)-bis-(2-methylimidazole)]. The relative orientation of the imidazoles is determined through the $2\nu_{dq}$ line shape. A method is developed for determination of the mutual orientation of the imidazole ligands, which is based on hybrid optimization simulations (OPTESIM) of the ^{14}N ESEEM from the remote imidazole nitrogen in Cu(II) model complexes with particular focus on the double quantum harmonic component. The technique reveals a bis-*cis*-imidazole coordination geometry in Aβ(13-21)H14A fibrils. Orientation selection ESEEM was performed on the Cu(II) model complexes, to relate the imidazole and Cu(II) molecular axes. Qualitative agreement with X-ray crystallographic results was obtained and the method was applied to Aβ(13-21) peptides. The number of coordinated histidine imidazoles in Cu(II)-Aβ(1-40) is addressed by ESEEM of ^{15}N-His13 or ^{15}N-His14 peptides. Fibrillar ^{15}N-labeled Aβ(1-40) gave comparable ESEEM, which is characteristic of His_2 coordination. Soluble Aβ(1-16) and Aβ(1-40) showed ESEEM that is intermediate between His_2 and His_3 coordination. Additional data is required for a consistent interpretation of these results. Overall, the results demonstrate the power of ESEEM for the determination of the three-dimensional molecular structure of Cu(II)-imidazole coordination, which can be applied to gain insight into the fibrillization process in Cu(II)-Aβ peptide complexes.

^{14}N Electron Spin Echo Envelope Modulation Spectroscopy of Cu(II)-Imidazole Coordination Structure in the Amyloid-β protein of Alzheimer's Disease and in Model Aβ Peptides and Complexes

By

Jessica Hernández Guzmán

B.A., Hollins University, Roanoke 2004

Advisor: Kurt Warncke, Ph. D.

A dissertation submitted to the Faculty of the James T. Laney School of Graduate Studies of Emory University in partial fulfillment of the requirements for the degree of Doctor of Philosophy in Physics

2010

Acknowledgments

After six years of constant perseverance, I have reached a completion point that marks the beginning of a new chapter of my life. This piece of work would have not been possible without the constant challenge, encouragement and guidance of my dearest advisor, Kurt Warncke, to whom I am most indebted. My gratitude to him is endless. In addition, I want to extend my gratitude to each member of my committee: Eric R. Weeks for always giving me his unconditional support, and helpful suggestions; David G. Lynn for explaining new concepts and challenging me with new ideas; Laura Finzi and Ivan Rasnik for sharing their thoughts and comments about my project.

This journey would have not been possible without the support, love and encouragement that my lovely family provided me in both the good and hard times when I thought I was not able to keep going. They always believed in me, and provided emotional and economical support. There are not enough words to thank them.

I also want to extend my gratitude to the department of physics staff, who helped me in various ways from administrative paper work to research involvement, and also for putting up with all my requests. Also, I want to show my appreciation to the faculty that shared their wisdom in and outside the classroom; to previous and present post-doctoral fellows who shared and nourished me with their ideas and experiences, particularly, Bill Gunderson who provided me with unconditional support for the completion of this work;

to the graduate-fellows for making the physics department an enjoyable environment to grow as a scientist. Especially, to my graduate-fellow and friend Wesley D. Robertson, who I shared not only an office with and the same advisor, but who was always the person who I could rely on at any moment, without him this journey would have been tougher.

Outside of the physics department, I am very grateful to my friends who brought great memories, experiences and made Atlanta feel like home. Especially, Rayane and her lovely family: Rabieh, Randa and her brother Elias. Also, I am thankful to Julianne, Tia, and the entire Chung family, as well as my friends Nashiely, Anna, Ha and Vu, Sara, Vinz, Dougly, Jose, Mike.

During my Ph.D. career, I encountered beautiful people, some of them I became much closer with than others. But everyone has a special place in my heart, and I am truly thankful to every single one for making these six years of my life an unforgettable experience. Thank you everyone!

Dedicated to my beloved parents,

Francisco Hernandez Segura and Margarita Guzman Alonso

who rest in peace.

Table of Contents

List of Figures

Chapter 1: Introduction to Aβ and metal ions interactions with Aβ

Chapter 2: Fundamentals

Chapter 3: Selection and synthesis of Cu(II) model complexes

Chapter 4: Applications of $2\nu_{dq}$, double quantum harmonic, analysis to Cu(II) model and Cu(II)-Aβ complexes

Chapter 5: Orientation selection ESEEM of Cu(II) model complexes

Chapter 6: Powder ESEEM of ^{15}N- and ^{13}C-labeled Cu(II)-Aβ complexes

List of Table

Chapter 4: Applications of $2\nu_{dq}$, double quantum harmonic, analysis to Cu(II) model and Cu(II)-Aβ complexes

Chapter 5: Orientation selection ESEEM of Cu(II) model complexes

Chapter 6: Powder ESEEM of ^{15}N- and ^{13}C-labeled Cu(II)-Aβ complexes

Chapter 1: Introduction to Aβ and metal ions interactions with Aβ

Alzheimer's disease (AD) is a progressive and devastating neurogenerative pathology that affects roughly 26 million people worldwide,[1] primarily aging adults. Characteristics of AD include memory disorders, degradation of personality and other behavioral abnormalities, which are correlated with the loss of neurons from the cortex and hippocampus.[2] These events are accompanied by the manifestation of progressive accumulation of neurofibrillary tangles (NFT) within neurons, and amyloid fibers surrounded by neuritic (senile) plaques in AD patient's brains, and within the walls of blood vessels.[3] The principal component of the AD amyloid deposits is an amphiphilic polypeptide, amyloid-β (Aβ). The Aβ peptide is a cleavage product of a transmembrane protein, known as the amyloid-β precursor protein (APP). The Aβ is cleaved from APP by two enzymes, β- and γ-secreatase,[4-5] as a soluble protein, which is detected in biological fluids and tissues.[6-8] This polypeptide is present in the brain and cerebrospinal fluid (CSF) of healthy humans throughout their lives, so that the presence of Aβ does not necessarily lead towards neuropathy.[9] In contrast, when a neuronal injury occurs, the Aβ aggregates into oligomers and large Aβ fibrils, which are considered to be a crucial event in the onset of AD.[10] Therefore, a major question, which remains unanswered, is the following: What triggers Aβ to become prone to aggregate, and form highly toxic oligomers, protofibrils and mature fibrils that accumulate in plaques?

1.1 Structure and assembly of amyloid-β

The Aβ is formed after sequential cleavage of the APP by the *β*- and *γ*-secretases in a two step process.[5,11] As shown in Figure 1.1.1, APP is first cleaved by β-secreatase, which allows for the APP large ectodomain to be released into the extracellular fluid, leaving a membrane-bound C-terminal fragment.[5] The remaining portion of the APP (99 amino acids) is then cleaved by *γ*-secreatase to produce Aβ, which is then released in the extracellular space.

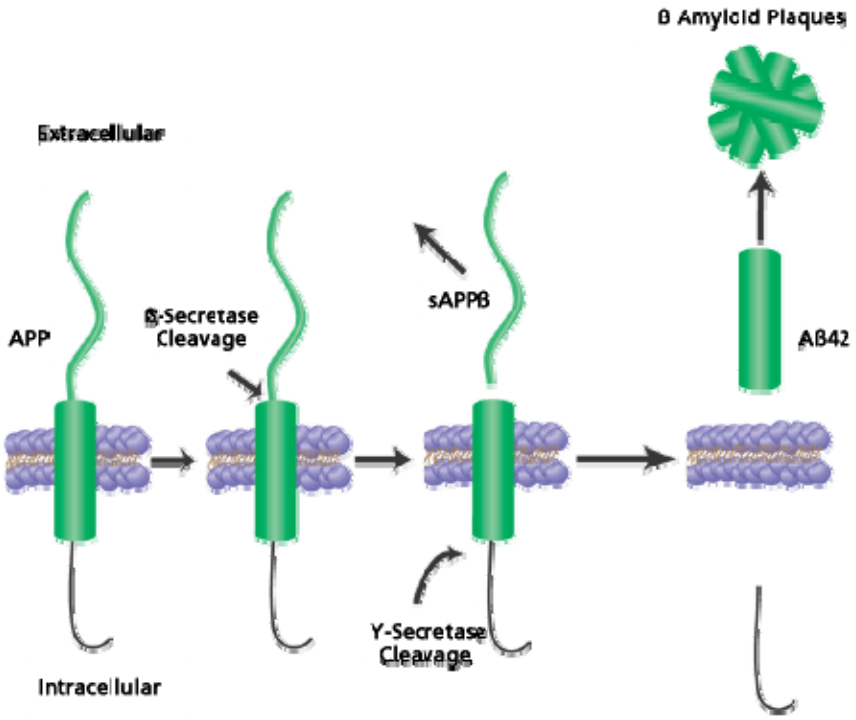

Figure 1.1.1 The Aβ peptide is formed by cleavage of the Amyloid Precursor Protein. APP is cleaved by β-secretase allowing its large ectodomain to be released into the extracellular fluid. The remains of APP is cleave of by γ-secretase, producing Aβ to be release into the extracellular. The Aβ(1-42) fragments then form the extracellular senile plaques common to Alzheimer's disease.[12]

The length of Aβ depends on the exact point of cleavage of the γ-secretase. Three principal forms of Aβ, comprising 39, 40 and 42 amino acid residues, are produced.[5,11] There are four distinct domains in Aβ, as depicted in Figure 1.1.2: a hydrophilic N-terminus (residues ^{1}DAEFRHDSGYEVHHQ^{16}K), a small hydrophobic region (residues ^{17}LVFF^{21}A), a small hydrophilic region (residues ^{22}EDVGSN^{28}K), and a long hydrophobic C-terminus (residue ^{29}GAIIGLMVGGVVI^{42}A).

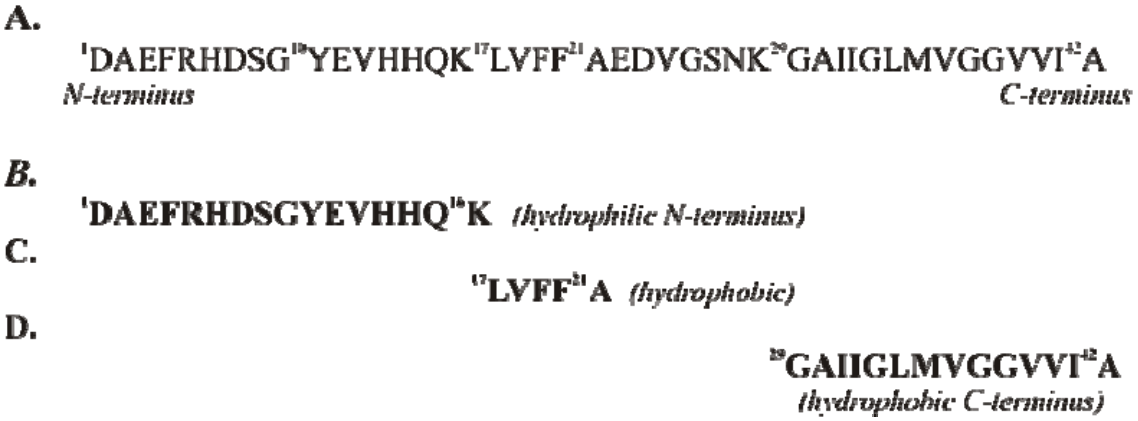

Figure 1.1.2 A. The amino acid sequence of Aβ can be separated into distinct domains: **B.** a hydrophilic N-terminus (aa 1-16), **C**. a central hydrophobic region, and a long hydrophobic C-terminus (aa 29-42).

The hydrophobic core region, Aβ(17-21), has been identified as essential for the formation of fibrils, and the C-terminus plays a major role in the aggregation process.[13-14] Aβ(1-40) is the most prevalent Aβ sequence found in AD, but it appears to be a minor component in Aβ deposits and likely contributes only to later phases of the disease pathology.[15] The major component in the deposits is Aβ(1-42).[16]

The Aβ peptide is capable of binding to multiple biomolecules, including lipids, proteoglycans and proteins,[17] on the surface of neurons, glial and endothelial cells through several mechanisms.[18-19] This property makes the Aβ an essential factor for the onset and progress of AD.[20] Therefore, great emphasis has been placed on the understanding of the mechanism of fibrillogenesis in simple conditions, *in vitro*. [19,21-26]

Although the Aβ peptide is a relatively short polypeptide of 39-40 amino acids compared to other proteins responsible for neurodegenerative disorders (i.e α-synuclein, 140 residues;[27] cellular prion protein, 231 residues[28]), it is difficult to determine the molecular basis of the recognition and assembly process which leads to amyloid-fibril formation. Moreover, due to insolubility and non-crystallinity of the peptide, characterization of the molecular structure of Aβ has been difficult.[6] *In vitro*, Petkova et al.,[26] showed that, depending on the conditions of fibril formation, the morphology of the fibril can differ. Therefore, the study of amyloid formation, with truncated versions of the Aβ polypeptide, can act as useful models for the full-length Aβ.[25,29-30] The synthetic Aβ(1–40/42) peptide and certain truncated versions have been able to produce fibrils *in vitro* with the same morphological, histochemical, immunological and spectroscopic properties as *in vivo* fibrils.[31-32] Consequently, different techniques, including high-resolution imaging and structural determination, have been used in an effort to understand the structural nature of amyloid fibrils, elucidate their self-assembly pathway and resolve the factors that affect it. The understanding of all of the key steps in the process of oligomerization, including nucleation and fibrillization can help to create an appropriate therapeutic strategy.

1.2 Metals ions and β-amyloid

The cerebrospinal fluid and blood plasma of humans has been found to contain soluble forms of Aβ(1-40) and Aβ(1-42) at concentrations of approximately 5 nM.[33-34] The trigger factor of soluble Aβ to amyloidogenic form has not yet been found, but physiological levels of Cu(II), Zn(II), and Fe(III) have been found to mediate the aggregation of Aβ.[35-37] In postmortem AD-affected brains, metal ions such as Cu(II) are found in high concentrations (0.4 mM) within plaques in the AD brain.[37] For the metal ions, Zn(II) and Fe(III), higher concentrations were found in the neuropil of the AD affected brain, (up to 1 mM). The high concentration of metal ions implicates their involvement in Aβ assembly, *in vitro,* and neuropathology of AD.[37-40]

The observation that Cu(II) and Zn(II)-selective chelators enhance the solubility of Aβ peptide from postmortem brain tissue of AD patients suggests that these metal ions play a role in the cerebral amyloid assembly.[41-42] Even though the full mechanism of amyloid plaque formation is not fully understood, *in vitro* evidence has shown that Cu(II) alters the self-assembly kinetics and toxicity of fibrils.[38,43] Different truncated and/or mutated versions of Aβ can develop different types of morphologies.[38]

For example, if Aβ is modified to Aβ(13-21)H14A, the metal ions Cu(II) and Zn(II) can bind and form fibrils.[38] The Aβ(13-21)H14A can self assemble and form a mixture of tightly twisted and non-twisted fibers (Figure 1.2.1A). In the presence of the metal ions, however, it aggregates to form smooth fibrils with almost no twist, as shown in Figure 1.2.1B-C.[39]

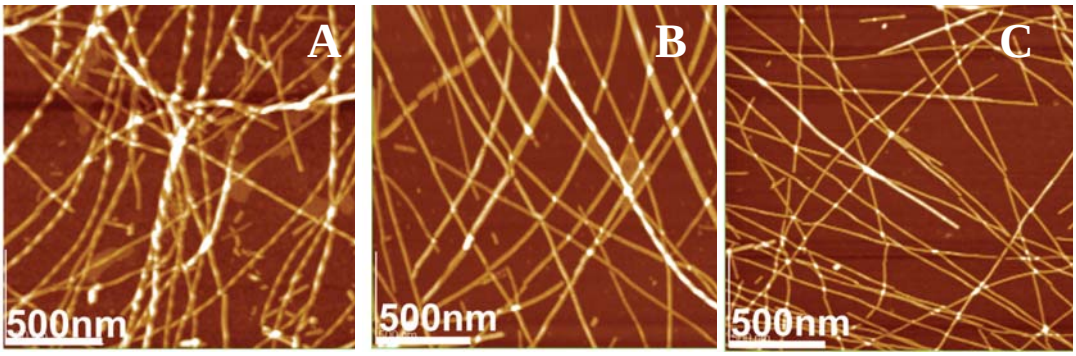

Figure 1.2.1 AFM images of amyloid fibrils for Ac-Aβ(13-21)H14A without and in the presence of Zn(II) and Cu(II). **A.** Ac-Aβ(13-21)H14A in absence of metal complexes. **B.** In the presence of 1 mMZn(II) **C.** 1 mM Cu(II). Images provided by Dong, J. et al.,[38]

Different truncated versions of Aβ bind the metal ions in two distinct ways, generally termed as the inter- and intra-molecular modes.[44] The inter- molecular mode corresponds to Aβ-metal binding with adjacent sheets as "Aβ-metal-Aβ" bridges, while the intra-molecular mode is the Aβ binding between a single β-strands (i.e the atoms participating in the metal coordination all belong to the same peptide). Different metal coordination structures for each binding mode result in distinct self-assembled morphologies, ranging from the amyloid fibrils to twisted ribbons and homogenous nanotubes.[39]

Despite all the evidence that Cu(II) plays an important role in AD, the precise coordination geometry and the residues involved in Cu(II) ligation and the dependence on the length of the peptide are still under debate.[45-46]

1.3 Structural models for metal ion binding to Aβ fibrils

1.3.1 Three dimensional proposed models for Aβ fibrils

Amyloid fibrils are sets of filamentous aggregates that result from the spontaneous self-assembly of the Aβ. Although all amyloid fibrils contain the β-sheets, formed by β-strand segments that run perpendicular to the fibril growth axis in a "cross-β motif",[47] the detailed molecular structures of the fibrils are not yet fully understood.[24]

Using Aβ(10-35), and a combination of techniques; including solid-state NMR, electron microscopy, and small angle neutron scattering (SANS), a 3-dimensional model was proposed by Burkoth et al.,[25] as shown in Figure 1.3.1.1. The suggested model has parallel in-register peptides, allowing the side chains of histidines 13 and 14 to be directed to opposite surfaces of the β-sheets. The fibril is formed of parallel in-register peptides, with six β-sheet laminations separated by 10 Å.[25] Within each sheet, the peptide is parallel in-register, and the distance between each peptide is 5 Å (Figure 1.3.1.1). This model suggests that the sheets within the fibril are parallel to each other and that the possible arrangements for Zn(II) binding would be intra-sheet binding or inter-sheet binding, or in some combination of intra-sheet binding and inter-sheet binding.

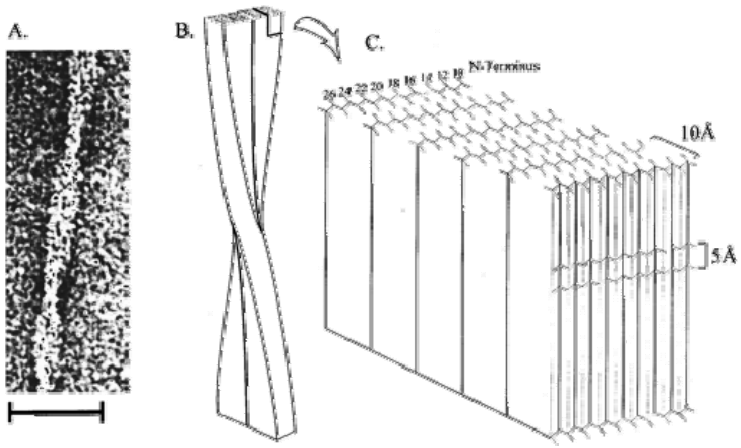

Figure 1.3.1.1 Three dimensional structure of Aβ(10-35).**A.** Electron micrograph of a fiber from Aβ(10-35). **B.** Structure of the paired fibrils as proposed by Burkoth et al.[25] **C**. Enlarged view of a portion of the paired fibril.

In addition, a model for the structure of the Aβ(1-40) fibril was proposed,[24,30] (Figure 1.3.1.2) based on solid state NMR, electron microscopy (EM), and X-ray diffraction. The fibril consists of three units of two spatially separated β-strands that are folded over one another to form a molecular double layer of β-sheets, in the form of a triangle, with each side having a "sandwich" (as depicted in Figure 1.3.1.2).[24,30] This model shows how favorable hydrophobic interactions can be maximized within the context of a cross-β structure with parallel β-sheets. Moreover, the proposed model reveals how an amyloid structure may contain both structurally ordered and disordered regions, with a combination of β-strand and non-β-strand segments in the ordered regions.

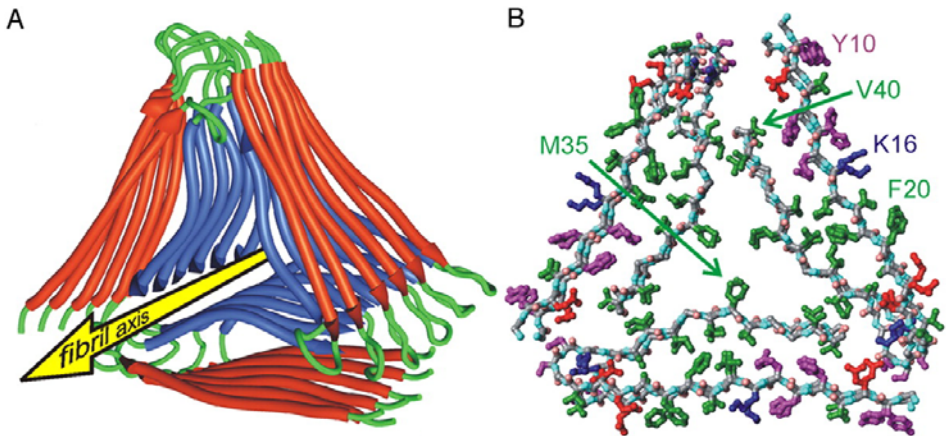

Figure 1.3.1.2 Proposed three dimensional structured model for Aβ(1-40). **A.** Ribbon representation of the lowest-energy model for fibrils with twisted morphology. **B.** Atomic representation of Ab(1-40) view down the fibril axis. Color code: hydrophobic (green), polar (magenta), negatively-charged (red), and positively charge (blue).[24]

1.3.2 Metal Ions in the association of Aβ fibrils

The overall structure as well as the N-terminal region of Aβ capable of metal-ion coordination within the Aβ fibrillization, plays a critical role in the neurotoxicity of the fibril.[38,48] The solubility and deposition of amyloid is affected by this binding, leading to either beneficial or toxic effects on neuron health, which depends on the concentration of metal ions.[37,45,49-50] This leads to the question of what is the beneficial concentration of metal and when this amount is too high that becomes harmful.

In vitro, metal ions have been shown to accelerate the rate of formation of the peptide, and modify the morphology.[40,51] Cu (II) has been shown to bind to the Aβ(1-40) fibril, which causes dissociation and formation of an aggregate structure.[40,52] However, Zn(II) can bind to Aβ(10-21), and form fibrils without forming aggregates.[36]

Several techniques have been used to investigate fibril formation with and without metal ions, but so far, no technique has been able to resolve the position of metals along the fibril. AFM has been used to determine the large scale structure of metal free, solution-grown Aβ protofibrils, fibril intermediates, and mature fibers on hydrophilic surfaces.[53] However, an in-depth study has not yet been conducted relating copper and zinc's role in large-scale fibril structure, nor has copper or zinc's location along the fibril been directly verified.[54]

Raman spectroscopy was recently used to demonstrate that the metal ions, Zn(II) and Cu(II), bind to the peptide via histidine residues.[55] This result is confirmed by solid-state NMR[38] and electron paramagnetic resonance (EPR) spectroscopy,[56] where the results show that the binding of the metal ions occurs via the histidines. But, there still ambiguity if all the histidines are involved or not.[20]

Metal ions have shown to bind to Aβ in different sites, depending on the length of the Aβ, and the specific sequence. For Aβ(1-40), different groups have proposed that the binding occurs through histidine[38,57] and possibly through tyrosine.[48] However, other models have shown that tyrosine does not affect the metal binding while histidines 6, 13, and 14 are involved in the metal binding.[40] Solid state NMR studies have suggested that the binding of metal ions is through histidines 13 and 14 for the whole peptide.[44]

Whereas, for a truncated and modified Aβ peptide, such as Aβ(13-21)H14A, the metal ions Cu(II) and Zn(II) can bind and form fibrils.[38] As previously explained, the metal-free Aβ(13-21)H14A can self assemble and form a mixture of twisting and non twisting fibers, Figure 1.2.1A, while in the presence of zinc or copper, the rate of fibrillizationis changed.[38] The position of the metal ion along the fibril is still unknown,

but Dong et al.,[38] suggested that Zn(II) and Cu(II) coordinate with the His13 residues from adjacent peptides arranged along the growing β-sheet surface (Figure 1.3.2.1).

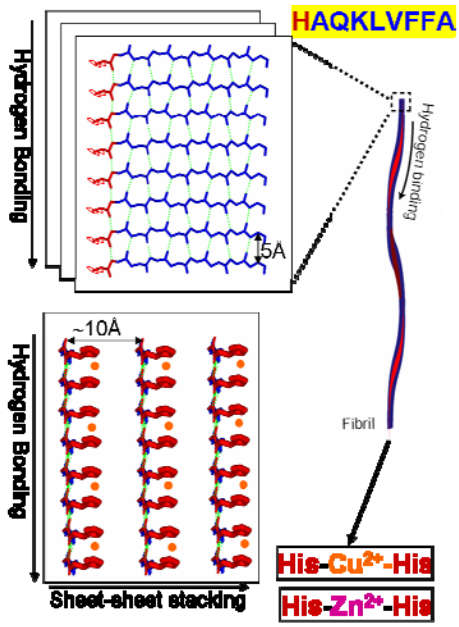

Figure 1.3.2.1. Possible model of Ac-Aβ(13-21)H14A fibril**. A.** Ac-Aβ(13-21)H14A assembles amyloid fibrils with hydrogen bonds parallel to the fibril axis **B.** Amyloid fibril composed of parallel in-register β-sheets, with or without metal ions. **C.** Side view of the amyloid fibril with either Zn(II) (magenta) or Cu(II) (orange) bound through the two histidines, both of which come from β-strands within the sheets.[38]

As introduced above, the process of aggregation and fibrillization of Aβ are key events in AD. Metal ions have been shown to either accelerate or arrest fibrillization depending on the length and amino acid sequence in truncated and mutated Aβ peptides.[38] In addition, the morphology of the fibrils can be altered by the presence of metal ions.[58] The focus of this dissertation is to developed different techniques of X-band electron spin echo envelope modulation (ESEEM) spectroscopy to determine the molecular structure of the Cu(II)-Aβ histidine imidazole coordination in cryotrapped

soluble and fibrillar forms of Aβ peptides, in order to gain insight into the factors that govern fibrillization.

Three-pulse ESEEM spectroscopy can describe the structure of the local environment of the remote ^{14}N nuclei. Calculation of the Euler angles, which relates the superhyperfine principal axis system of one imidazole to the other imidazole, can distinguish a *cis*- or a *trans*- molecular conformation. Additionally, from the simulations of the ESEEM data, the dipolar superhyperfine tensor form was determined to relate the orientation of the superhyperfine principal axis with the g_z-tensor of Cu(II).

Three Cu(II)-imidazole model complexes are synthesized to serve as models for the Aβ complex. These complexes have a known molecular coordination established through X-ray crystallographic analysis. These Cu(II)-imidazole models include a single imidazole, a bis-*trans* and a bis-*cis* imidazole. Each model complex was examined using three-pulse ESEEM spectroscopy. The Fourier transform for all three models showed the remote imidazole ^{14}N nuclear quadrupole, and double quantum features that are typical of "exact cancellation", as will be explained in Chapter 2. The bis-imidazole Cu(II) model complexes also show combination lines and the double quantum harmonic, $2\nu_{dq}$, which is consistent with bis-imidazole coordination. The $2\nu_{dq}$ line shape is dependent on the relative orientation of the two ^{14}N hyperfine principal axis system (as explained in Chapter 4). For each model complex, a powder simulation of the three-pulse ESEEM data provides the ^{14}N nuclear quadrupole and hyperfine tensors. In addition, for the bis-imidazole complexes, the Euler angles that specify the relative orientation of the two ^{14}N hyperfine principal axis system were obtained. A physical model was created which allows each molecular conformation (*cis*- or *trans*-) to be distinguished. Results from the

model complexes were compared to the results for the Aβ(13-21) peptide. By inspection, the line shape for the $2\nu_{dq}$ feature for the Aβ(13-21) peptide has the same shape as the bis-*cis* complex. Using the simulation analysis for the model complexes, Cu(II)-Aβ binding was proposed to have a bis-*cis* conformation, allowing a physical model to be proposed.

Orientation selection ESEEM was performed for each of the Cu(II) model complexes and for the two congeners of the Aβ(13-21) peptide to determine the coordination geometry of the g_z-tensor of Cu(II) with respect to the superhyperfine principal axis system. This approach will be explained in Chapter 5. The analysis was based on the movement of the double quantum feature, ν_{dq}, with the variation of the magnetic field. The results from the Cu(II) model complexes are in good agreement with the X-ray crystallographic structure. Orientation selection was also performed for the Cu(II)-Ac Aβ(13-21)H14A, and Cu(II)-Aβ(13-21)K16A peptides. For these peptides, the $2\nu_{dq}$ feature shifts in frequency indicating that the $2\nu_{dq}$ is orientation selection dependent.

ESEEM spectroscopy can also be used to identify the number of imidazoles that are equatorially coordinated to a metal center such as Cu(II). This technique was performed on both the fibrillar and soluble Aβ(1-40) peptide, as well as Aβ(1-16), in an attempt to resolve the conundrum of the number histidines binding to the Cu(II)-Aβ polypeptide. Three-pulse ESEEM was performed on uniformly labeled ^{13}C, ^{15}N Aβ(1-40) at either His13 or His14. The ESEEM waveform shows characteristics in the modulation that depend on the number of imidazoles binding to the Aβ peptide. These

results allow the binding of one ^{14}N or 4 identical ^{14}N to be ruled out. However, a final conclusion as to the binding between two or three ^{14}N nuclei was not resolved.

Chapter 2: Fundamentals

2.1 Continuous Wave Electron Paramagnetic Resonance (CW-EPR)

For more than 60 years, continuous wave (CW)-EPR spectroscopy has been one of the most powerful techniques capable of determining the structure, dynamics and the spatial distribution of paramagnetic species. It does this by characterizing the interaction of a paramagnetic center with an applied magnetic field. This is measured through the absorption of electro-magnetic radiation, typically microwave radiation. CW-EPR is a spectroscopic technique capable of measuring the absorption of electromagnetic radiation by molecules, ions, or atoms with at least one unpaired electron spin (S>0).[59] Also, CW-EPR has played an important role in characterizing the active site structures of paramagnetic metalloproteins. For some metal centers, EPR has identified metal ligands by using model compounds.[43,60-63]

The fundamentals of EPR can be explained through the simple case of a free electron. For an electron with mass m_e and a charge $-e$, the angular momentum gives rise to a magnetic moment

$$\vec{\mu}_e = -g_e \beta_e \vec{S} \qquad [2.1.1]$$

where, β_e is the Bohr magneton and is defined by $\beta_e = \frac{e\mathsf{h}}{2m_e}$. The g_e factor, (free electron g value), is required to account for deviations of the behavior of a quantum object from the behavior of a classical charged particle, and has a value of $g_e = 2.0023$. The $\vec{S}$ is the

electron spin, $\vec{S} = 1/2$, which can have two possible states m_s = -1/2 and m_s = + 1/2. When no magnetic field has been applied, $\mathbf{B}_0$ = 0, the electron states are degenerate, meaning they have the same energy. In the presence of a strong static magnetic field, the energy of the electron's magnetic moment separates the two possible states, m_s = -1/2 and m_s = + 1/2. This splitting of states is called the Zeeman effect.[64] The corresponding Hamiltonian for this condition is expressed as:

$$H = g_e \beta \vec{B} \cdot \vec{S} = m_s g_e \beta B_0 \qquad [2.1.2]$$

Classically, lower energy state is created when the two states are aligned parallel to the static magnetic field. The energy difference between the lower state and the upper state corresponds to:

$$\Delta E = g_e \beta B_0 \qquad [2.1.3]$$

Therefore, the energy difference of the two electron states is proportional to the magnetic field strength, $\mathbf{B}_0$, as can be inferred from equation [2.1.3]. Furthermore, the transition between the two electron states can be induced by an electromagnetic field with a frequency, ν, if the photon energy $h\nu$ matches this energy separation as:

$$\Delta E = h\nu = g_e \beta B_0 \qquad [2.1.4]$$

where, B_0 is the magnetic field at which the resonance condition is met. Equation [2.1.4] corresponds to the fundamental equation of EPR spectroscopy. This is depicted in the scheme (Figure 2.1.1.A) below:

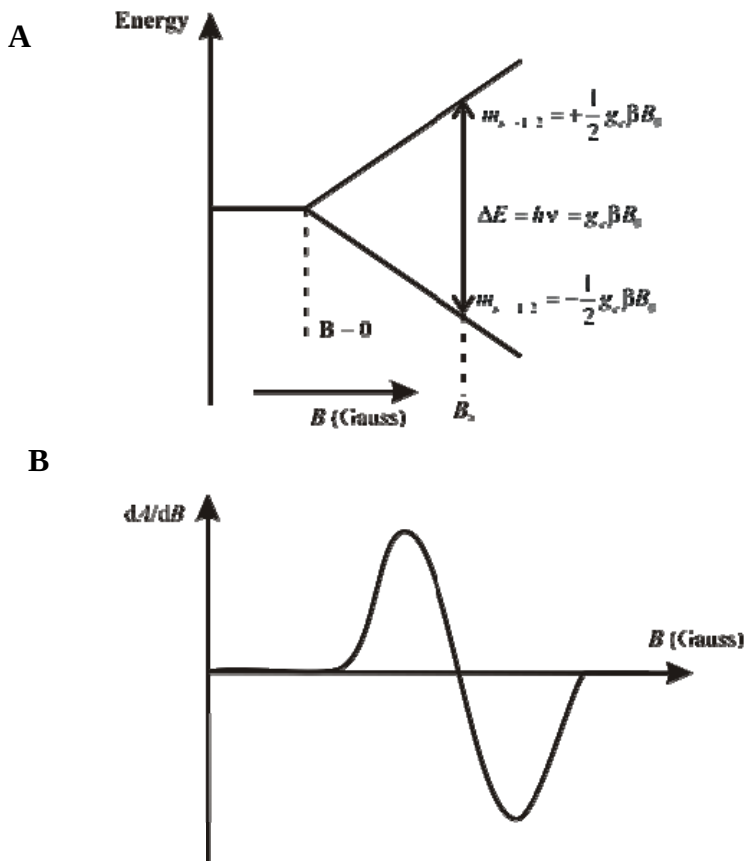

Figure 2.1.1 A. Energy level diagram for electron Zeeman splitting in an external magnetic field for a single electron ($S = 1/2$). **B**. Typical EPR spectrum for an electron.

At thermal equilibrium, the population ratio of the two electron states m_s, is given by the Boltzmann distribution:[65]

$$\frac{n_{+1/2}}{n_{-1/2}} = \exp\left(-\frac{\Delta E}{kT}\right) = \exp\left(-\frac{h\nu}{kT}\right) \qquad [2.1.5]$$

when this ratio is less than one, and the electron spin-lattice relaxation is present, which causes the spin to return from the upper state to the lower state (i.e. $m_s = +1/2$ to $m_s = -1/2$), an absorption of the electromagnetic radiation is observed when the resonance condition is met.

Furthermore, from the resonance condition (equation [2.1.4]), different frequency and magnetic field values are permitted. Typically, in EPR experiments the radiation frequency is fixed and the magnetic field is varied to achieve the resonance condition.[64] Experimentally, a typical EPR spectrum at resonance condition is recorded by the derivative of the amplitude versus the magnetic field (Figure 2.1.1.B).

For a more complex system like Cu(II), there are additional terms in the Hamiltonian due to the nuclear spin, $\vec{I}$. The corresponding Hamiltonian has the form:

$$H = H_{Ze} - g_n \beta_n B_0 \cdot \vec{I} + \vec{S} \cdot A \cdot \vec{I} \qquad [2.1.6]$$

where H_{Ze} is the electron Zeeman term as defined in equation 2.1.2, the second term is the nuclear Zeeman term ($I = 3/2$ for Cu(II)), and the last term is the hyperfine term. The $\vec{S}$ and $\vec{I}$ are the electron and nuclear spin operators, respectively, and A is the hyperfine tensor.

The above description assumes an isotropic *g*-value (a single value, independent of the field direction). For randomly oriented spin systems (i.e. powder samples), in which the molecular orientations are present, such as transition metal ions in condensed phase (solid or liquid), the *g*-values can differ along various molecular orientations.[64,66] The principal axes of the *g*-tensor are often roughly aligned along the principle axes of the molecule (Figure 2.1.2).[64] Furthermore, when the powder sample is oriented at some particular direction with respect to the magnetic field, $\mathbf{B_0}$, will exhibit a *g*-value, $g(\theta\phi)$, given by the equation

$$g^2(\theta,\phi) = \left[g_{xx} \sin\theta\cos\phi\right]^2 + \left[g_{yy} \sin\theta\sin\phi\right]^2 + \left[g_{zz} \cos\theta\right]^2 \qquad [2.1.7]$$

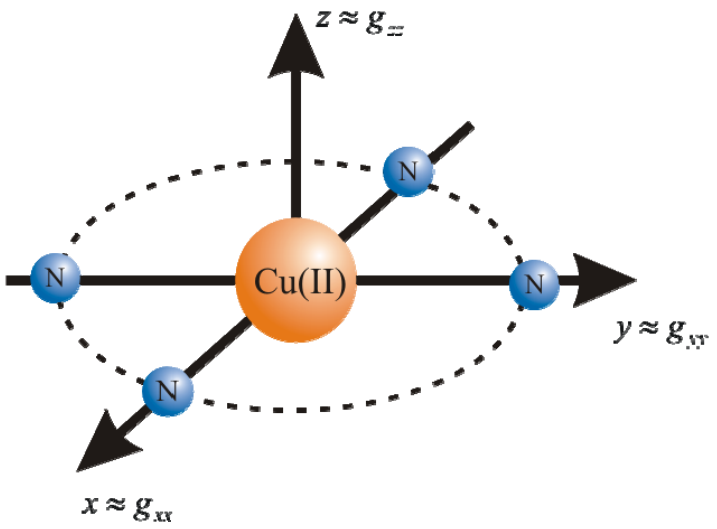

Figure 2.1.2 Alignment of the *g*-tensor in the molecular frame. The scheme depicts an axial symmetry of the molecular system with four equivalent ligands, and therefore the molecular symmetry of the *g*-tensor.

The *g*-value observed in a particular direction (specified by the angles θ and ϕ) is the weighted mean of the three principal values of g_{xx}, g_{yy}, and g_{zz}. The weighting factors are the projections of the direction of the magnetic field onto the principal axes of the *g*-tensor and are given in terms of θ and ϕ, the polar and azimuthal angles between the principal axis of the *g*-tensor and the direction of $\mathbf{B_0}$ (Figure 2.1.3).[67] For this reason, a *g*-tensor is used to describe the EPR spectrum.

When the molecule in a Cu(II) complex has axial symmetry, the *g*-tensor will also have axial symmetry and the *g*-values in the *x,y*-plane are equal. The axial symmetry of the *g*-tensor is represented by the notation $g_{xx} = g_{yy} = g_{\perp}$ and $g_{zz} = g_{\|}$. For axial symmetry, the average *g*-value is obtained from:

$$g^2(\theta) = [g_{\perp} \sin\theta]^2 + [g_{\|} \cos\theta]^2 \qquad [2.1.8]$$

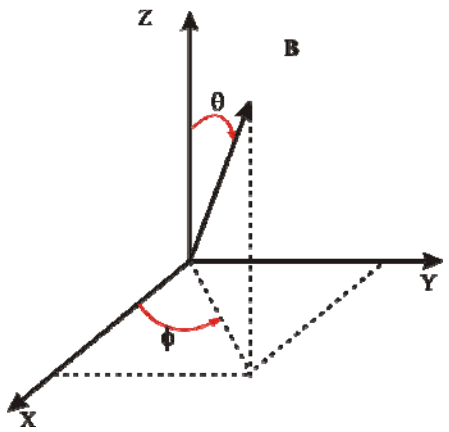

Figure 2.1.3 Alignment of the external magnetic field with respect to the principal axis system of the molecule. The vector represents the external magnetic field, θ is the polar angle between the *z*-axis of the molecule and the magnetic field, and ϕ is the azimuthal angle of the projection of the magnetic field in the *x*-*y* plane from the *x*-axis.

In addition, Cu(II) has a nuclear spin of $I = 3/2$, therefore, the energy manifold will have four allowed transitions. These transitions depend on the EPR selection rules. The selection rules state that the transitions are allowed only between states that differ by one unit in $\Delta m_s = \pm 1$, while there is no change in the nuclear spin $\Delta m_I = 0$. This is observed in the energy diagram (Figure 2.1.4), and the EPR spectrum will have four distinctive features corresponding to the allowed transitions. However, Cu(II) centers exhibit a wide range of stereochemistries (tetra-, penta-, and hexa- coordination). For a tetragonal coordination, which is commonly used for studies on metalloproteins, the *g*-tensor is usually axially symmetric, with $g_{zz} > g_{xx} = g_{yy} > 2.0023$, the free-electron *g*-value.[68] The *g*-tensor *z*-axis is set to be normal to the plane of the copper and the four equatorial ligands (Figure 2.1.2). Furthermore, anisotropy of the hyperfine interactions is manifest by components parallel and perpendicular to the molecular symmetry axis, designated $A_{\parallel}$ and $A_{\perp}$.

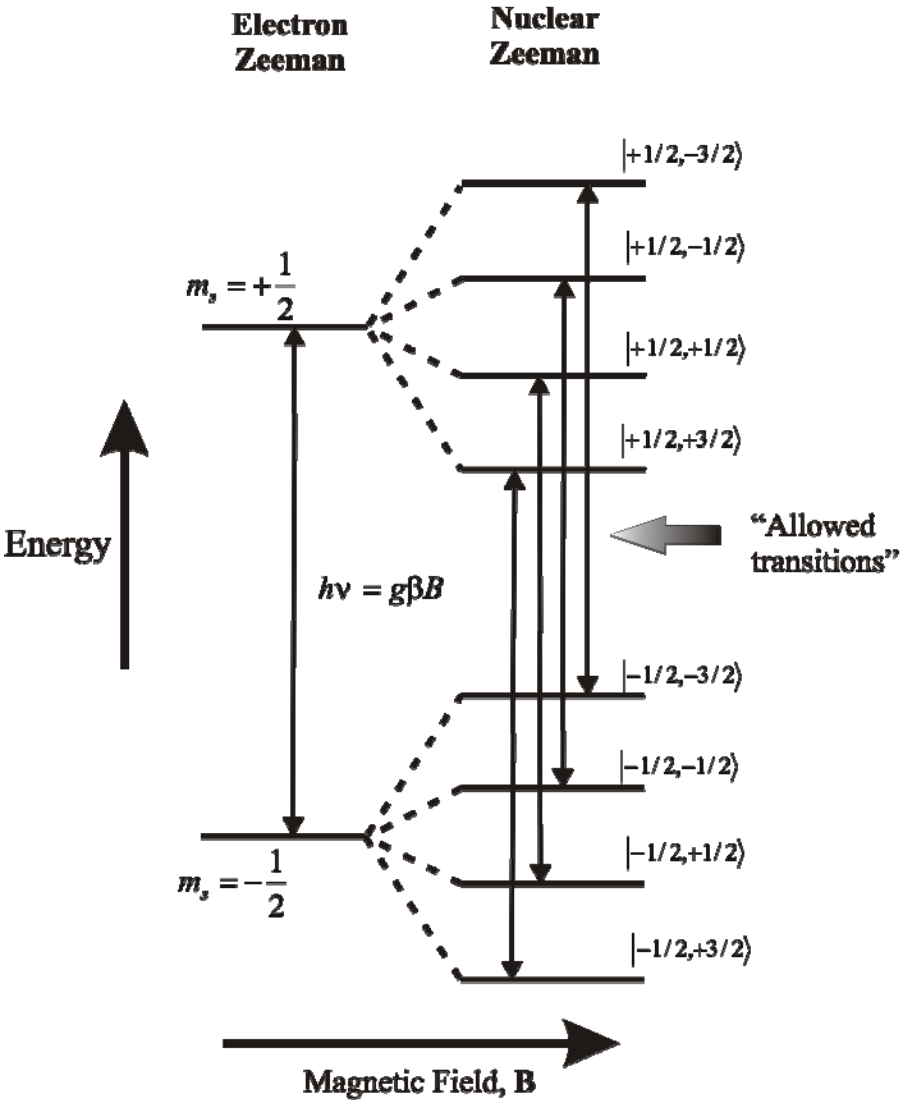

Figure 2.1.4 Energy level diagram for Cu(II) with a nuclear spin of $I = 3/2$ and an electron spin of $S = 1/2$.

When copper is equatorially coordinated to a single ^{14}N nucleus, the nuclear spin of ^{14}N is unity, so the splitting is observed as a triplet having intensities in the ratio 1:1:1. Therefore, for an electron exposed to *n* equivalent nuclei, the number of lines is equal to $2nI+1$ but the intensity of the individual lines varies in a specific pattern, determined by over lapping transitions ratios as 1:2:3:2:1 for 2 equivalent nuclei, 1:3:6:7:6:3:1 for 3 nuclei, while 1:4:10:16:19:16:10:4:1 for 4 equivalent nuclei. The EPR spectrum of a typical Cu(II) complex $(H_2O)_6$ (copper aquo), is shown in Figure 2.1.5.

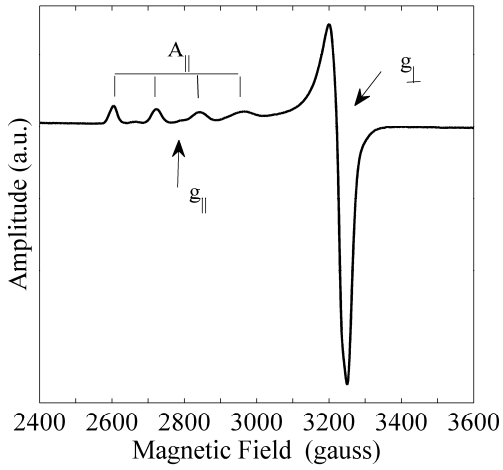

Figure 2.1.5 EPR spectrum of aqueous Cu(II) [Cu(II)$(H_2O)_6$]. The spectrum shows the characteristics features of Cu(II). The $g_x = g_y = g_{\|}$ and $g_{\perp}$. $A_{\|}$ represents the hyperfine term.

For Cu(II) in solution, which has sufficiently large anisotropic magnetic interactions, particular orientations of the spins are excited depending on the *g*-tensor orientation with respect to the $\mathbf{B}_0$ field. For N_0 axial molecules, the number of systems at a particular angle, θ (the angle between the magnetic field and the *z*-axis of the molecule, as shown in Figure 2.1.3), is proportional to the $\sin\theta d\theta$ term:

$$dN = \frac{N_0}{2}\sin\theta d\theta \qquad [2.1.9]$$

where, dN is proportional to the area of the surface of a sphere included with an angle variation of $d\theta$.[69] The factor two is included because it is only necessary to cover a hemisphere to include all of the spins. In addition, the $sin\theta$ factor shows the predominance of molecules with axes nearly perpendicular to the field direction relative to those with axes, which are more nearly aligned along the field direction. For simplicity, the transition probability can be assumed to be independent of orientation, the number of dN molecules lying between θ, and $\theta + d\theta$, is proportional to the absorption intensity of the EPR spectrum as a function of the angles covered (0 - 90°).

The g value is a function of θ (equation 2.1.8), and therefore, for a specific frequency, ν, the corresponding Hamiltonian is given by:

$$H = \frac{h\nu}{\beta}\left(g_{\|}{}^2\cos^2\theta + g_{\perp}{}^2\sin^2\theta\right)^{-1/2} \qquad [2.1.10]$$

The intensity of absorption in a range of magnetic field dH is proportional to

$$\left|\frac{dN}{dH}\right| = \left(\frac{dN}{d\theta}\right)\cdot\left|\frac{d\theta}{dH}\right| \qquad [2.1.11]$$

At the two extreme cases ($\theta = 0°$, and $\theta = 90°$), the intensity of absorption varies from

$\left|\frac{dN}{dH}\right| = \frac{N_0 g_{\|}{}^3}{2g^0 H^0 (g_{\|}{}^2 - g_{\perp}{}^2)}$ (at $\theta = 0°$) and $\left|\frac{dN}{dH}\right| = \infty$ (at $\theta = 90°$). As depicted in Figure 2.1.6A, the intensity absorption line versus the magnetic field will increase in amplitude

as larger numbers of the nuclear spins in the sample are oriented perpendicular to the magnetic field. Experimentally, the sharp angles in Figure 2.1.6A, are rounded, as shown in Figure 2.1.6B, because the natural width of the lines of the individual molecules contributing to the absorption spectrum is considered. If there are hyperfine interactions in the randomly oriented molecules, the EPR line pattern in Figure 2.1.6C, will be split into *2I + 1* patterns as shown for the case of copper aquo (Figure 2.1.5).

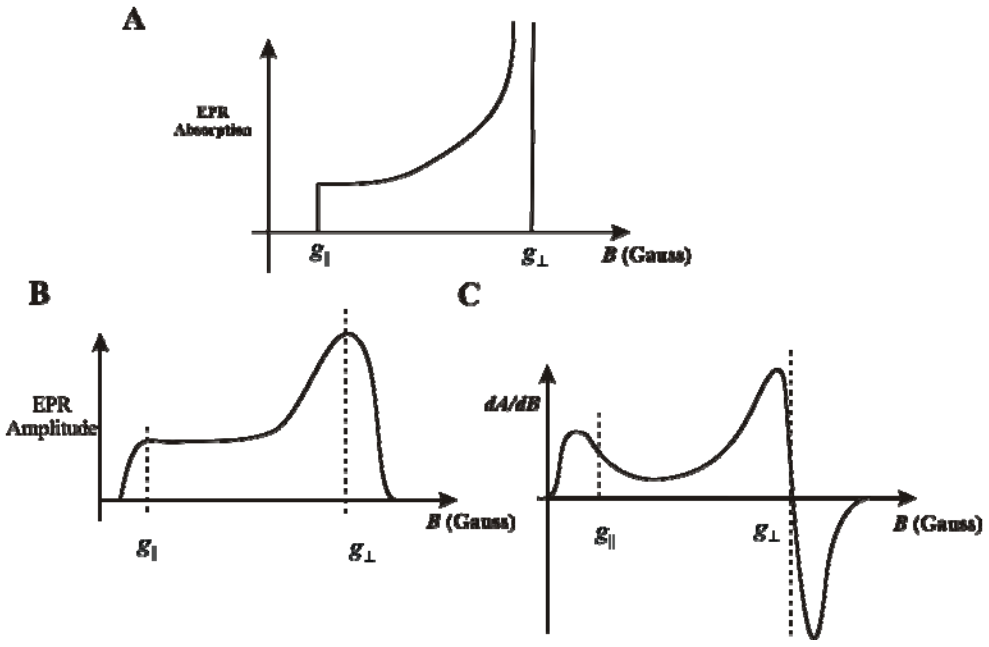

Figure 2.1.6 A. The intensity of absorption for an EPR spectrum plotted versus the magnetic field. **B.** A typical EPR absorption spectrum. **C.** The first derivative of an EPR absorption spectrum; due to experimental conditions the first derivative absorption curve is typically observed.

The relative intensity of absorption of observed transitions is determined by the orientation the angle, θ, of the molecule relative to the magnetic field, ***B***, or approximately, by $\sin\theta\left|\frac{d\theta}{dB}\right|$. This angle weighting leads to the characteristic EPR line

shape. The magnetic field moves from along the *z*-axis into the *x,y*-plane, as θ increases from 0°, when the magnetic field is aligned with the *z*-axis, to 90°, when the magnetic field is in the *x,y*-plane (Figure 2.1.7).

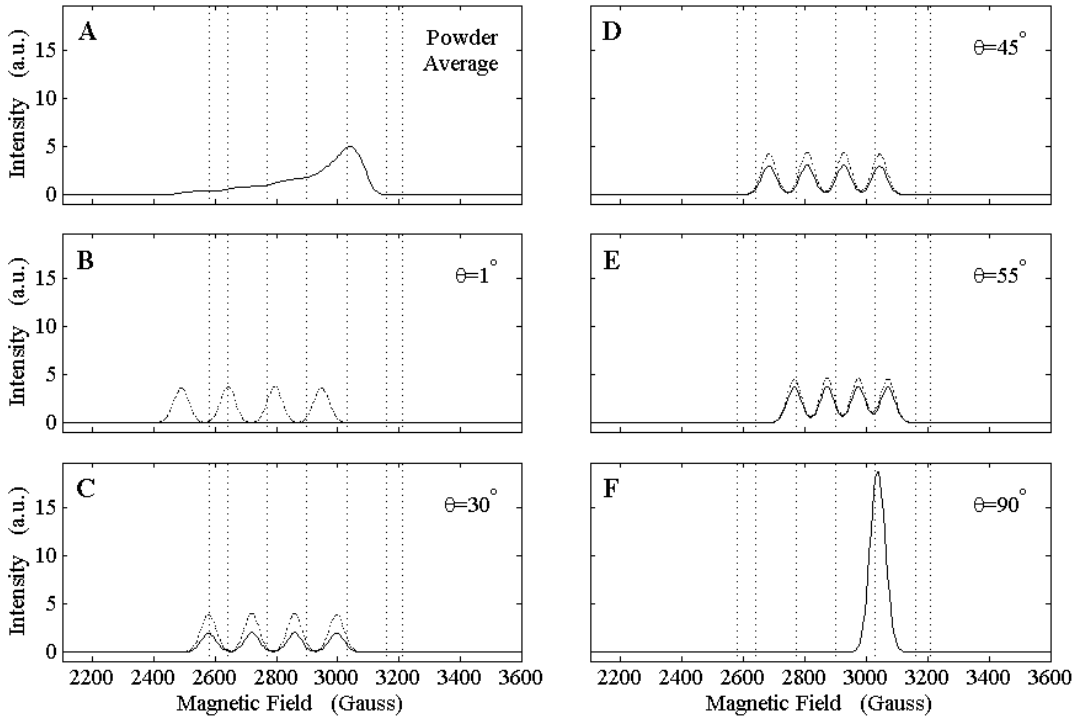

Figure 2.1.7 A. EPR absorption spectrum for a powder sample (i.e. all ϕ and θ orientations) of a Cu(II)-bis-*cis* imidazole complex (see chapter 5 for further details). **B-F.** EPR absorption spectra for a particular orientation of θ, at a fixed ϕ value ($\phi = 45^{0}$). The dotted line corresponds to the EPR absorption spectra at a particular θ value, and the solid line is the EPR absorption line multiplied by $\sin\theta$, (to observe the angle weighting effect). The spectrum was collected at 120 K, 9.34 GHz, 12 scan averages.

This causes a greater area of the segment, dθ, around the *z*-axis, and thus more electron spin systems are included as θ increases. As the field approaches the *x,y*-plane, more transitions are excited and thus there is greater microwave power absorption. As shown in Figure 2.1.7, at θ = 90°, the EPR absorption spectrum has a larger absorption

compared to the other orientations of θ. In addition, a plot of EPR absorption versus θ, Figure 2.1.8, illustrates the probability of the spin to orient at a specific θ angle, where the powder position occurs at 3030 G.

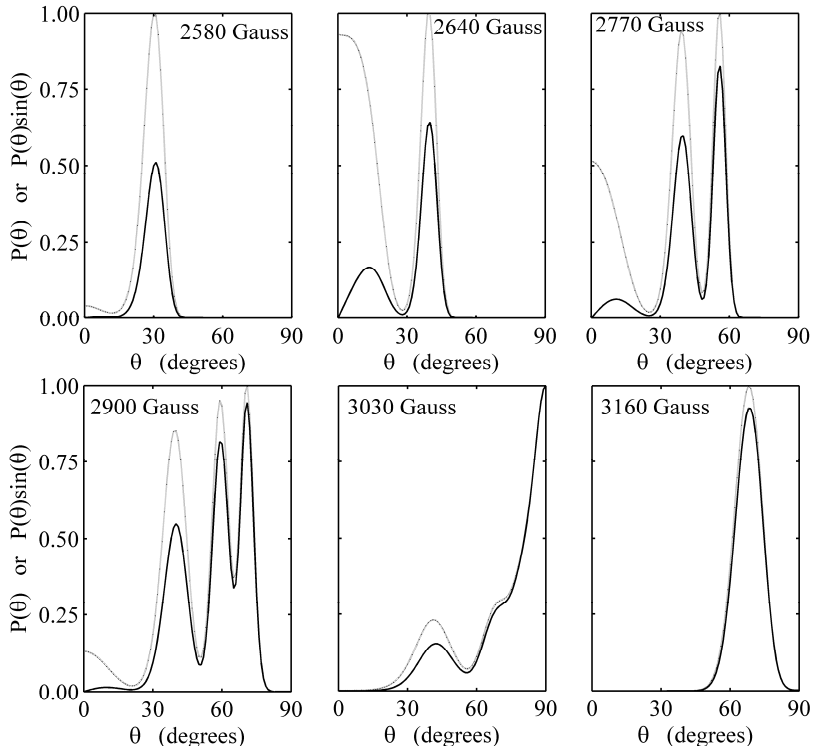

Figure 2.1.8 Orientation of the magnetic field with respect to the principal axis of the *g*-tensor. Six different magnetic fields, 2580, 2640, 2770, 2900, 3030 and 3160 Gauss, are shown. The "powder position" corresponds to 3030 G, where all the spins orientations of the molecule are excited at this specific magnetic field. The dotted curve shows an experimental EPR absorption line. The solid line corresponds to the experimental EPR absorption line multiplied by $sin\theta$ (corresponding to the angle weighting effect).

CW-EPR has played an important role in identifying metal ligand structures in Cu(II) proteins,[70] using the unique spectral signature of the *g*-tensor and hyperfine term (Figure 2.1.5). The EPR spectrum of Cu(II) can be used to identify one or more nuclear spins coordinated to the Cu(II) through the superhyperfine splittings. These

superhyperfine splittings arises from the magnetic interaction of the electron spin of the metal ion with the nuclear magnetic moment of a coordinated nucleus. Therefore, the superhyperfine pattern provides information about the type and number of interacting nuclei.

In a Cu(II) protein, the presence of superhyperfine lines can be taken as proof of a coordinating nucleus (i.e. ^{14}N). However, quantifying the number of interacting nuclei can sometimes be complex. In some cases, the spectra resolution is poor, owing to strain broadening. Or, the superhyperfine patterns could overlap in the EPR spectrum, especially in the region of $g_{\perp}$, leading to inaccurate structural assignment.

The ability to accurately make structural assignments ultimately rests in the ability to resolve spectral components. Pulse-EPR methods provide a mean of overcoming homogeneous line broadening, allowing for determination of the structure, function and dynamics of proteins, free radicals, and magnetic material.

2.2 Electron Spin Echo Envelope Modulation (ESEEM)

Electron Spin Echo Envelope Modulation (ESEEM) spectroscopy is a pulsed-EPR technique,[71-72] in which a paramagnetic sample is subjected to a series of microwave pulses, and the formation of a spin echo is studied. In particular, ESEEM is capable of detecting splittings arising from the superhyperfine structure (shfs) in the EPR resonance line, which are obscured by inhomogeneous line broadening in continuous wave EPR.[73]

This provides information on the structure of the nearest environment, coordination with certain molecules, the bond type,[74] for almost every paramagnetic center of biological interest.[74-76]

The simplest way to understand the electron spin echo (ESE) formation is through the classical description of the spin echo phenomenon. Although, EPR must be based on quantum mechanics, because quantum objects are involved on a microscopic level, experiments are usually done on an ensemble of electron spins.[72] The macroscopic magnetization of the sample due to these spins is created and manipulated by applying static and time-dependent magnetic fields. Consequently, a classical description of the spin echo formation will at least provide the basic aspects of ESEEM.

2.2.1 Spin Echo Phenomenon: Classical description

A classical description of the spin echo formation is based on the concept of an inhomogeneously broadened resonance line. This inhomogeneous line can be considered to be composed of an ensemble of "homogenous spin packets", forming the magnetization vector. From the Stern-Gerlach experiment, the electrons are known to possess an intrinsic angular momentum, $\hbar\vec{S}$. As previously mentioned, the electron has a magnetic moment, μ_e, (equation 2.1.1). For an ensemble of electrons, the magnetic moment for the ensemble will be the sum of each magnetic moment, i.e. $\mu=\sum\mu_i$. The quantity that is detected in the measurement of spin ensembles is the net magnetic moment per unit volume, which is called the macroscopic magnetization, **M**. The

minimal energy state occurs when all of the electron spins are aligned parallel to the external magnetic field, $\mathbf{B}_0$. The direction of the static field is chosen as the z_L-axis of the laboratory frame with coordinates x_L, y_L, z_L. The time dependence of the magnetization associated with each ensemble of electron spins (spin packets) in the static field, $\mathbf{B}_0$, yields

$$\frac{d\vec{M}}{dt} = \vec{M} \times \frac{-g_e \beta_e}{\hbar} \vec{B}_0 \qquad [2.2.1.1]$$

The magnetization **M** is invariant when it is aligned along the static field, $\mathbf{B}_0$. Otherwise, there is always a torque perpendicular to **M**. Only the angle between **M** and $\mathbf{B}_0$ and the length of the vector **M** will remain invariant and **M** will precess on a cone about the B_0 axis with an angular frequency of

$$\omega_s = \frac{g_e \beta_e}{\hbar} B_0 \qquad [2.2.1.2]$$

which is called the Larmor frequency, as seen in Figure 2.2.1.1.

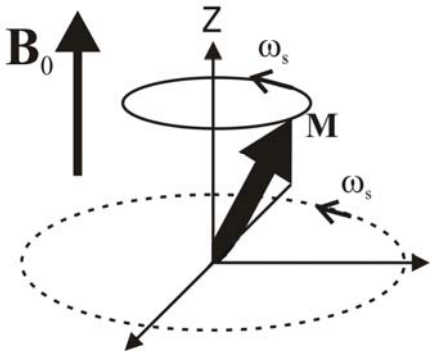

Figure 2.2.1.1 Magnetization vector precessing with a Larmor frequency ω_s in the lab frame. **M** represents the electron magnetization vector and $\mathbf{B}_0$ the static magnetic field under resonance condition.

Due to inhomogeneous broadening, the spin packets will precess with a frequency of $\omega_s = \frac{g_e \beta_e}{\hbar} B_0 - \omega_0$, where ω_0 is the frequency corresponding to a frame that rotates around the direction of $\mathbf{B}_0$ (the rotating frame). The spins packets will precess with the same Larmor frequency, but with different phases. Therefore, in a steady state, the resultant magnetic moment of every spin packet is aligned along $\mathbf{B}_0$.

In addition to the static magnetic field $\mathbf{B}_0$, in the experiment, microwave radiation is applied with frequency ω_0 and polarized in the *xy*-plane. The linear polarized electromagnetic wave can be decomposed into two counter-rotating circular polarized electromagnetic waves, one of which is rotating in the same direction as the Larmor precession of the spins (often referred as the rotating frame), and the other one is neglected since is off resonant. Therefore, if the microwave radiation were stronger (larger than the spread of the Larmor frequency) the magnetization would get oriented along $\mathbf{B}_1$. The magnetization will rotate (typically by $\pi/2$ or π radians) to the *x*,*y*-laboratory plane. The rotation angle depends on the pulse width, microwave frequency, and microwave phase. The spin packets will dephase (i. e. "fan–out in the *xy*-plane") after the pulse is turned off. A second pulse applied at a time, τ, after the first pulse will rotate the spin packets by π, generating an echo at τ after the second pulse. This corresponds to the one dimensional two-pulse ESEEM experiment, as illustrated in Figure 2.2.1.2a, where the varying parameter is τ. As τ is incremented, the spin echo does not decrease monotonically, but instead, modulations in the echo envelope are observed (Figure 2.2.1.2b). These echo envelope modulations arise from the magnetic interaction

of the electron spin of the paramagnetic with nuclear spins in the vicinity. The pattern of modulations is related to the precession frequencies of these nuclei.

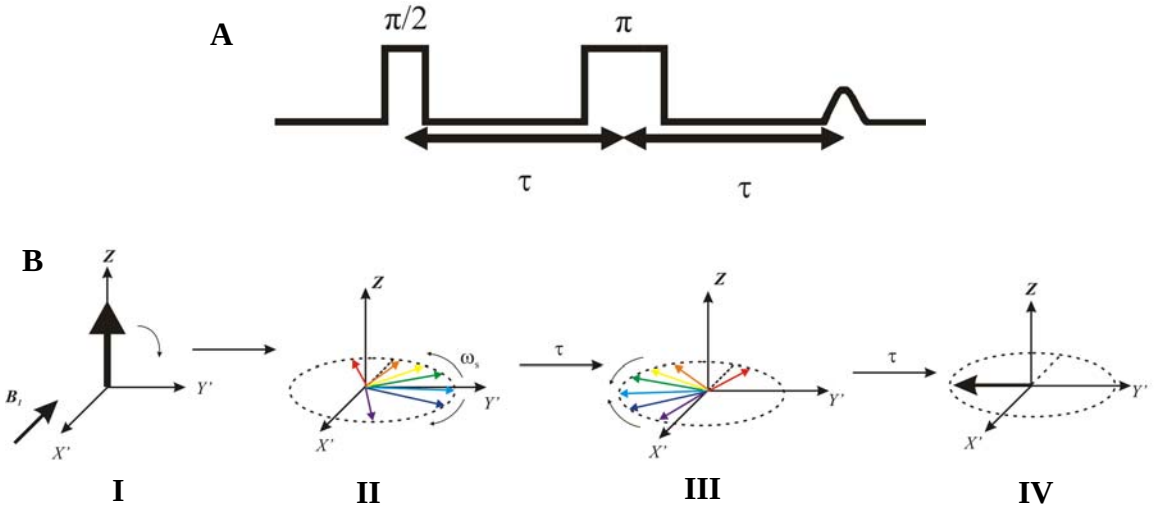

Figure 2.2.1.2 A. Pulse timing diagram for two-pulse ESEEM sequence. The echo envelope is obtained by incrementing τ and observing the echo intensity as a function of τ. The two pulse sequence is $\pi/2$-τ- π-τ-detection. **B**. Schematic representation of the Magnetization vector during the two-pulse experiment. **I**. Before the first $\pi/2$ pulse; **II.** After the first pulse ($\pi/2$) is applied. **III**. After the second pulse ($\pi/2$). **IV** Echo formation at $t = 2\tau$.

The modulation envelope obtained by this method consists of periodicities that are related to a superhyperfine frequencies associated with the various electron spin states on a spin manifold. This suggest that a careful analysis of the echo envelope can be useful to find superhyperfine splitting which are obscure by inhomogeneous line broadening in straight forward resonance experiments.[73]

The one dimensional two-pulse experiment measures the "phase memory time" that corresponds to the time during which a spin can "remember" its position in the dephased pattern after the first pulse. However, the phase memory time is rather short, (≈ 1 μs), which limits the time over which the modulations can be obtained. This is partly an

instrumental limitation. In the case where the periodicities are long or where the modulations are quickly damped, the lines in the Fourier transform will be broad. Additionally, spin-spin interaction may broaden lines, making analysis difficult.

An alternative procedure is the one-dimensional three pulse experiment. As illustrated in Figure 2.2.3.a, two pulses are separated by a time τ, and a third pulse is applied at a time T after the second pulse, where each pulse is a $\pi/2$ pulse. The spin echo is observed at time τ after the third pulse. The schematic of the echo formation is shown in Figure 2.2.3b. In this experiment, τ is fixed and the value of T is varied. The echo intensity is modulated with periodicities related to the magnetic interaction of the electron spin and nearby nuclei. In addition, the three-pulse experiment allows the resonance of the proton to be suppress, by setting a value of τ which corresponds to a whole number multiple of the periodicity of protons (i.e. $\tau = \frac{n}{\nu_{1_H}}$).

The three-pulse experiment has longer characteristic envelope decay times, which make it possible to determine the frequencies more accurately in the Fourier transform.[73] Therefore, three-pulse ESEEM offers highest resolution for nuclear quadrupole paramenters, and superhyperfine coupled nuclei. ESEEM spectroscopy studies[77-82] have proven to be capable of identifying the binding of metal sites in various Cu(II) proteins by the nuclear quadrupole interations (nqi) arising from the remote nitrogen of the coordinated ligand.[83] Futhermore, nuclear quadrupole parameters can be altered by changes in the local environment of the remote nitrogen.[82]

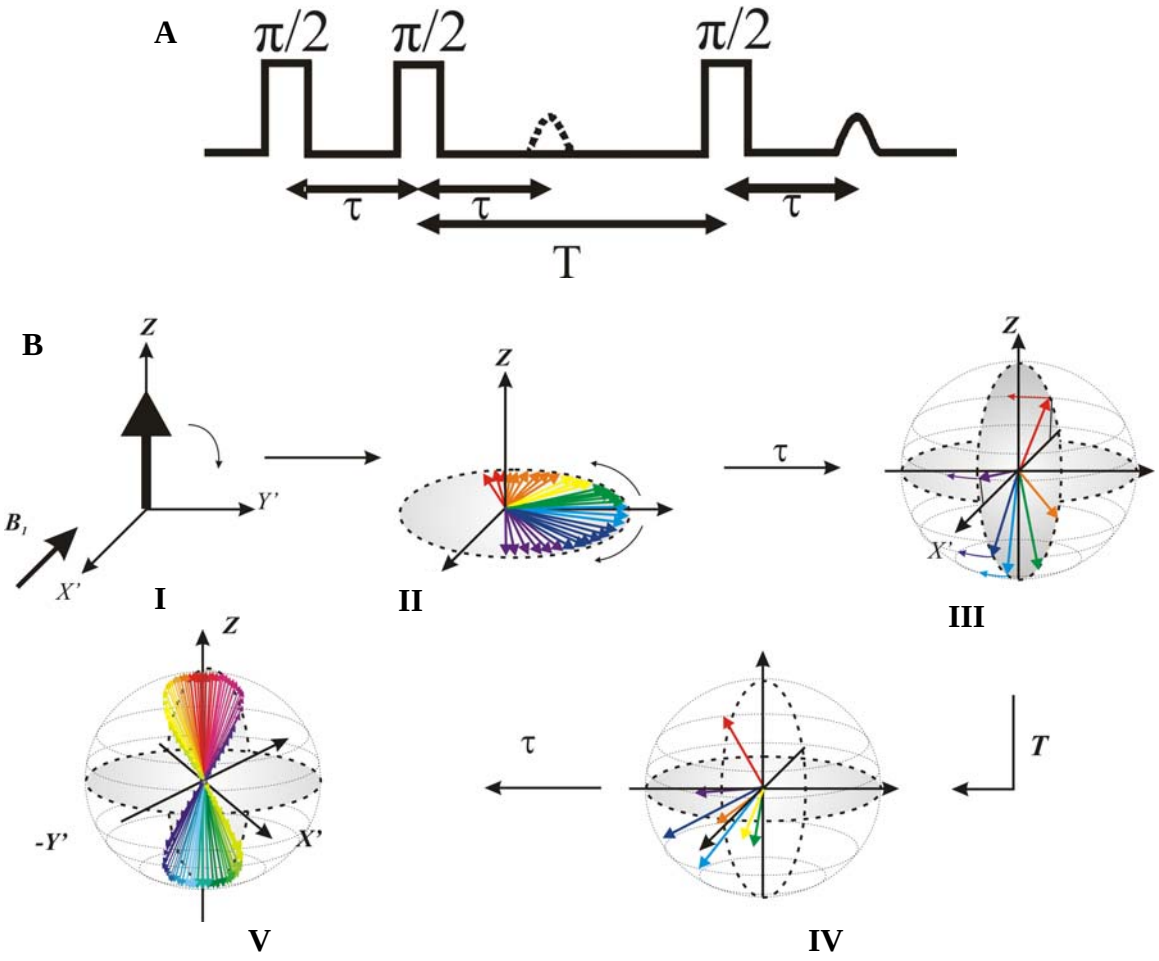

Figure 2.2.1.3 A. Pulse timing diagram for a three-pulse ESEEM pulse sequence. The time τ is set and T is incremented. The echo envelope is then obtained from the observation of the echo intensity as a function of $T + \tau$. **B**. Vector diagram of the Magnetization pattern during the three-pulse experiment. The static magnetic field $\mathbf{B}_0$ is along the z-axis. I. Before the first pulse. II. Right after the first pulse ($\pi/2$). III. After time τ, the second pulse is applied ($\pi/2$). IV. After the third pulse ($\pi/2$). V. After time τ, echo formation occurs at $t = 2\tau + T$.

2.2.2 Nuclear Modulation Effect

In ESEEM spectroscopy the periodic pattern which is commonly observed in the electron spin echo decay envelope arises as a result of coupling between an electron spin and nuclear moments in its immediate vicinity.[73,84-87] In ESEEM spectroscopy it is often possible to detect a periodic "modulation" which results from superhyperfine structure in the resonance line as shown in Figure 2.2.2.1. This phenomenon is referred to the "nuclear modulation effect". The modulation effect is briefly described, for the case of the two-pulse ESEEM.

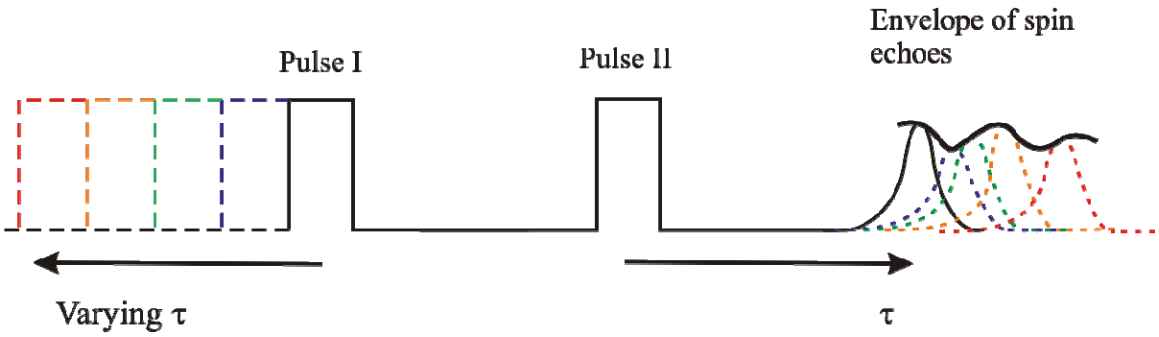

Figure 2.2.2.1 Schematic of two-pulse echo signals obtained by repeating the spin echo cycle of events with increasing values of τ. Periodic modulation of the echo envelope reveals superhyperfine structure in the microwave resonance interval.

In ESEEM spectroscopy the modulation of the echo intensity, as a function of pulse separation, arises from the simultaneous excitation of nuclear spin allowed ($\Delta m_s = \pm 1$, $\Delta m_I = 0$) and semiforbidden ($\Delta m_s = \pm 1$, $\Delta m_I = \pm 1, 2$) transitions. This mix of transitions, starting from one level of the manifold (i.e. $m_s = -1/2$) and ending at different ones of the other manifold (i.e. $m_s = +1/2$) is called "branching of transitions". This "branching" of the transitions is essential for envelope modulation to be observed.

Figure 2.2.2.2 shows a six energy level diagram for an electron spin, S = 1/2, coupled with a nuclear spin, I = 1. Only those levels of the overall-all quantized system for which the transition between m_s = + 1/2 and m_s = - 1/2 have a significant amplitude are shown. These transitions can be assigned to two classes, allowed and semiforbidden.

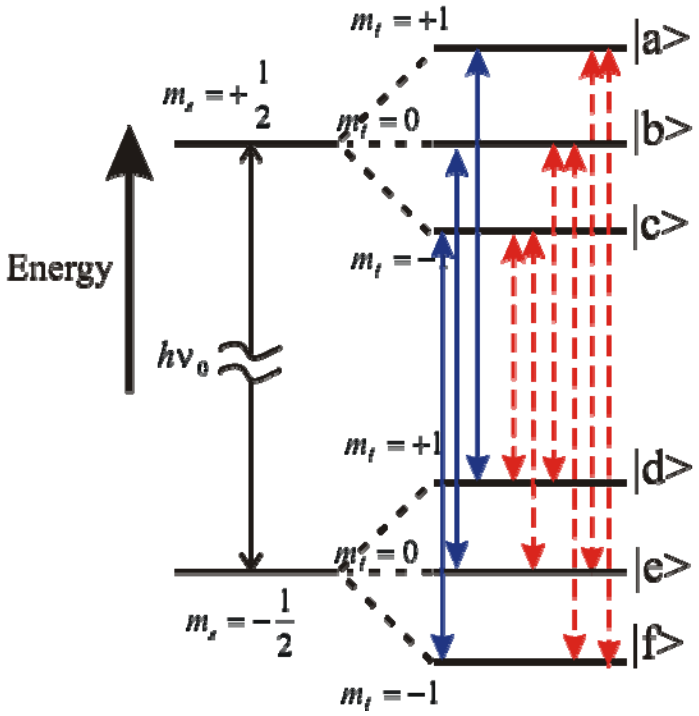

Figure 2.2.2.2 Energy level diagram for an nuclear spin I = 1 (e.g. ^{14}N) weakly coupled to an S = 1/2 electron spin. The nuclear states are mixed (e.g., by electron nuclear dipolar coupling). The allowed transitions are shown in solid blue lines and the semiforbidden transitions are shown in broken red lines. Simultaneous excitation of both types of transitions by the microwave pulses leads to interference effects in spin echo generation, and results in the echo envelope modulation phenomenon.

For example, consider an electron spin in state |f> before the microwave pulse I. When pulse I is applied the allowed transition |f> to |c> is induced and, to a lesser degree, the semiforbidden transitions |f> to |a> and |f> to |b> are induced as depicted in Figure 2.2.2.2. After pulse I the wave function for the system corresponds to a coherent superposition of wave functions corresponding to states |a>, |b>, and |c>, with |c> being

the major component in the sum. During the first interval, τ, between pulses I and II the terms corresponding to states |a>, |b>, and |c> evolve with phase factors $\exp(-iE_a\tau/h)$, $\exp(-iE_b\tau/h)$, and $\exp(-iE_c\tau/h)$ respectively. The second microwave pulse then induces the allowed transitions (shown in solid blue line in Figure 2.2.2.2), |a> to |d>, |b> to |e>, |c> to |f>, and the semiforbidden lines (shown in broken red lines Figure 2.2.2.2) |a> to |e>, |a> to |f>, etc. Further phase evolution occurs during the time τ between the pulse II and the echo, and additional phase factors [$\exp(-iE_d\tau/h)$, $\exp(-iE_e\tau/h)$ and $\exp(-iE_f\tau/h)$] are attached to various components of the wave function. Finally, the echo is formed (generated by the allowed transitions, and, in part, by the semiforbidden transitions), and interference between the components of the wave function are manifest as a change in echo amplitude.

Therefore, the phenomenon of the "nuclear modulation effect" is the effect of the echo envelope being modulated by the superhyperfine frequencies.[74] This is true as long as the superhyperfine levels associated with one electron spin state are connected to superhyperfine levels associated with the other by allowed and also by semiforbidden transitions (i.e. the transitions must branch), and also provided that the microwave field in the pulse is large enough to encompass the superhyperfine splitting of the electron spin states.

2.2.3 Exact Cancellation: Nuclear quadrupole interactions

ESEEM spectroscopy is a technique well suited for studying the remote nitrogens of the copper ligating histidines or imidazoles (i.e. those imidazole nitrogens that are not directly coordinated to copper).

The quadrupole moment in ^{14}N gives rise to the modulation patterns observed in ESEEM spectra. The corresponding spin Hamiltonian for ^{14}N is:

$$H_N = -g_N \beta_N \cdot \vec{I} + h\vec{S} \cdot A_N \cdot \vec{I} + \vec{I}' \cdot Q \cdot \vec{I}' \qquad [2.2.3.1]$$

The first term is the nuclear Zeeman interaction, where g_N and β_N are nuclear *g*-factor and Bohr magneton, $\mathbf{B}_0$ is the external magnetic field, and $\vec{I}$ is the nuclear spin operator. The second term is the electron-nuclear superhyperfine interaction, where A_N is the superhyperfine tensor and $\vec{S}$ is the electron spin operator. The third term is the nuclear quadrupole interaction, where Q is the quadrupole interaction tensor.

At frequencies in the X-band range (8-12 GHz), the nuclear Zeeman term is approximately equal to one-half the electron-nuclear superhyperfine term, $h\vec{S} \cdot A \cdot \vec{I}$. This feature is characteristic of the "exact cancellation"[83,88] condition (Figure 2.2.3.1). Therefore, for one of the ^{14}N spin manifolds, the nuclear Zeeman terms are almost canceled by the electron-nuclear superhyperfine term so that the energy level splittings are determined solely by the nuclear quadrupole interactions.[82] Figure 2.2.2.3A shows the ESEEM spectrum at exact cancellation.

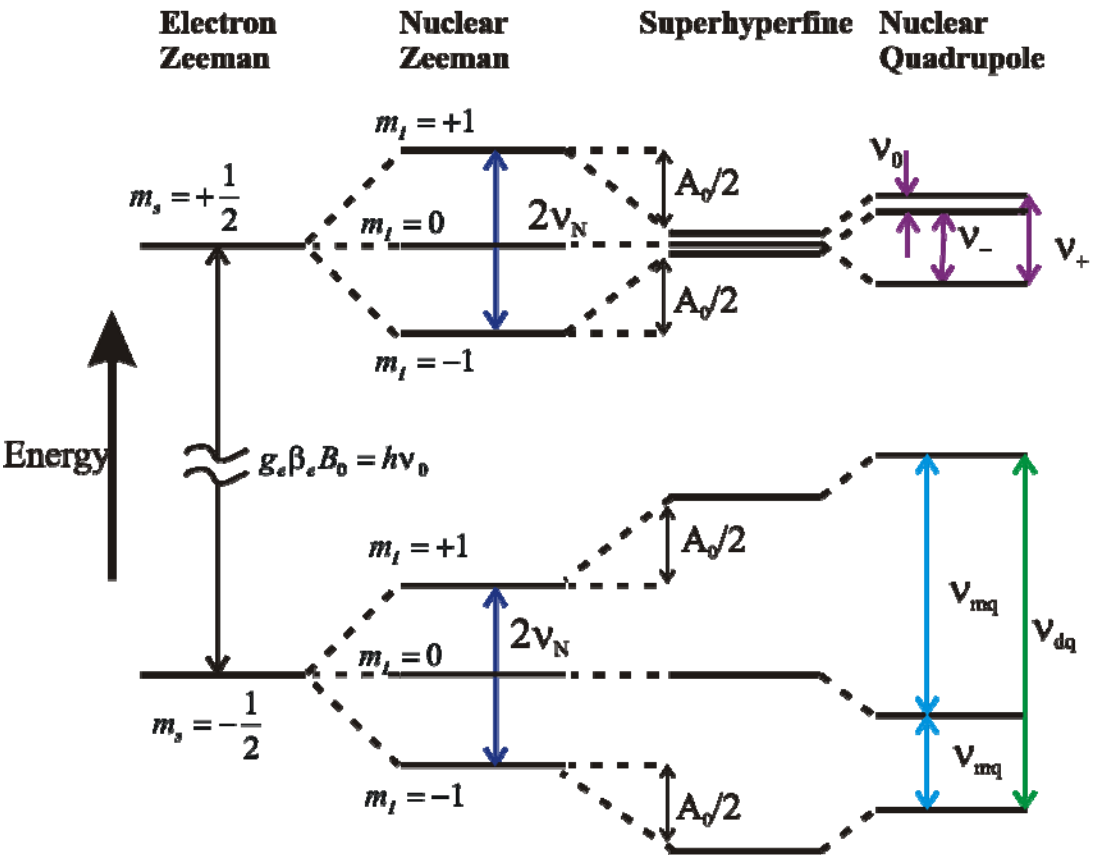

Figure 2.2.3.1 Electron spin energy level diagram for ^{14}N with an I = 1 nucleus interacting with an S = 1/2 electron spin at "exact cancellation". The three corresponding nuclear quadrupole interactions are designated ν_0, ν_-, and ν_+. The ν_{dq} corresponds to the $\Delta m_I = 2$ transition.

The nuclear quadrupole interactions give rise to three sharp lines in the Fourier transform ESEEM spectrum, which corresponds to the transitions at ν_0, ν_- and ν_+, nuclear quadrupole frequencies. The other spin manifold, the nuclear Zeeman and superhyperfine terms are additive, consequently, the nuclear Zeeman term is doubled by the electron-nuclear coupling, giving rise to a single broad line at about four times the nuclear Zeeman frequency, creating a $\Delta m_I = \pm 2$ transition, commonly known as the "double quantum" feature.[89-90]

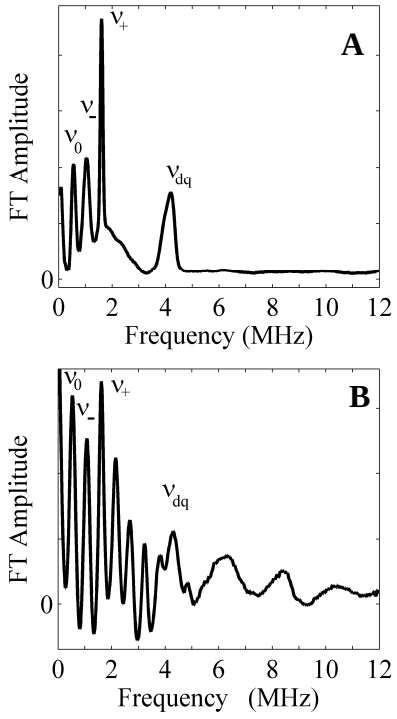

Figure 2.2.3.2 ESEEM spectra of Cu(II) coordinated to **A.** single and **B.** four methylimidazole molecules. The sharp, low frequency lines in the spectra corresponds to the zero field quadrupolar frequencies of the remote ^{14}N of Cu(II)-coordinated imidazole. The combination lines are present only for the four-imidazole complex.

One advantage of the ESEEM method, as compared to other pulse-EPR methods, is the ability to quantify the number of coupled nuclei associated with a paramagnetic center. For example, when more than a single imidazole ^{14}N is coupled to Cu(II), in addition to the fundamental features, the appearance of "combination lines" are observed in the ESEEM spectrum.[81] In the case of a single imidazole ^{14}N coupled to Cu(II), a four line spectrum is seen, which contains three zero field quadrupolar lines and a broader component at higher frequency, (≈ 4 MHz), corresponding to the $\Delta m_I = \pm 2$ transition. As the number of interacting, equivalent coupled nuclei is increased, new lines appear in the spectrum whose frequencies are combinations of the nuclear quadrupole frequencies of the single-imidazole Cu(II) complex and the double quantum feature (Figure 2.2.3.2B).

This method is useful in differentiating populations containing a single or multiple ^{14}N coordination. Distinguishing between 2 and 3 or 3 and 4 nuclei becomes more complicated, as this is based on comparisons with appropriate models. ESEEM simulations serve as a tool to distinguish the different subtleties of the spectra. In addition, from the analysis of the spectrum based on spectra simulation, the simulation can provide detailed information about the nuclear and electronic structure of the molecular paramagnet, such as the superhyperfine tensor and electric field gradient (efg) tensor (nuclear quadrupole interaction).[83,91] Other information that can be inferred from the spectra simulation, includes the effective distance between the unpaired electron and its interacting nucleus and the relative orientation of the principal axis of the superhyperfine tensors of the ^{14}N in question to that of the *g* tensor for Cu(II).[82,92-93]

2.2.4 Orientation Selection

ESEEM has been used to investigate hyperfine and quadrupole interactions of nitrogen nuclei. The determination of the quadrupole coupling constants and the orientations of the quadrupole tensor principal axes with the *g*-tensor principal axes directly yielding valuable information regarding structure and bonding at the nitrogen site.[88] As mentioned previously (section 2.1), in randomly oriented spin systems with sufficiently large anisotropic magnetic interactions, particular orientations are selected depending on the setting of the $\mathbf{B}_0$-field.

2.2.4.1 Anisotropic dipolar hyperfine

For the ^{14}N system, the hyperfine part of the Hamiltonian (equation 2.2.3.1) is composed of two terms: the isotropic and anisotropic hyperfine. The isotropic hyperfine, $hA_{iso}\vec{S}_z \cdot \vec{I}_z$, is a result of the transfer of the electron's spin orbital with the spin orbital of the nucleus. The magnetic field does not affect the splitting caused by the interaction of the spin with surrounding nuclei, so the molecular orientation of the system is not affected. The second term is the anisotropic dipolar hyperfine, $\vec{S} \cdot A_{dip} \cdot \vec{I}$, which expresses the dependence of the hyperfine splitting on the orientation. The classical expression for the dipolar interaction energy between a fixed electron and nucleus separated by a distance *r* is:

$$E_{dip} = \frac{\mu_e \cdot \mu_N}{r^3} - \frac{3(\mu_e \cdot r)(\mu_N \cdot r)}{r^5} \qquad [2.2.4.1.1]$$

where, μ_e, and μ_N are the corresponding magnetic moments, with their respective operators ($\hat{\mu}_{e_z} = -g_e \beta_e \hat{S}_z$ and $\hat{\mu}_{N_z} = g_N \beta_N \hat{I}_z$).[64] The corresponding Hamiltonian is thus:

$$H_{dip} = -g_e \beta_e g_N \beta_N \left[\frac{\hat{S} \cdot \hat{I}}{r^3} - \frac{3(\hat{S} \cdot r)(\hat{I} \cdot r)}{r^5} \right] \qquad [2.2.4.1.2]$$

The H_{dip} involves a tensor interaction, which can be seen by expanding the vectors. For simplicity, the z-component of the H_{dip} is explained. This interaction can be assigned because both $\hat{S}$ and $\hat{I}$ are quantized along H (considering as the z-axis), so the x and y components of $\hat{S}$ and $\hat{I}$ in the expanded version of equation [2.2.4.1.2] can be neglected. If we consider spherical coordinates, $z = r\cos\theta$, so equation [2.2.4.1.2] is reduced to:

$$H_{dip} = A_{dip}(3\cos^2\theta - 1)\hat{S}_z \hat{I}_z \qquad [2.2.4.1.3]$$

where, θ is the angle between the external magnetic field and $A_{dip} = -\frac{g_e \beta_e g_N \beta_N}{r^3}$. This term corresponds to the point-dipole approximation of the electron-nucleus interaction, and implies a dipolar hyperfine tensor of axial symmetry. In this treatment of the Hamiltonian, only the component of the dipolar hyperfine coupling that arises from the canonical values of θ (0° and 90°) is given. The frequency range of the hyperfine spectrum for $0° < \theta < 90°$ is inferred from the $\sin\theta d\theta$ weighting.

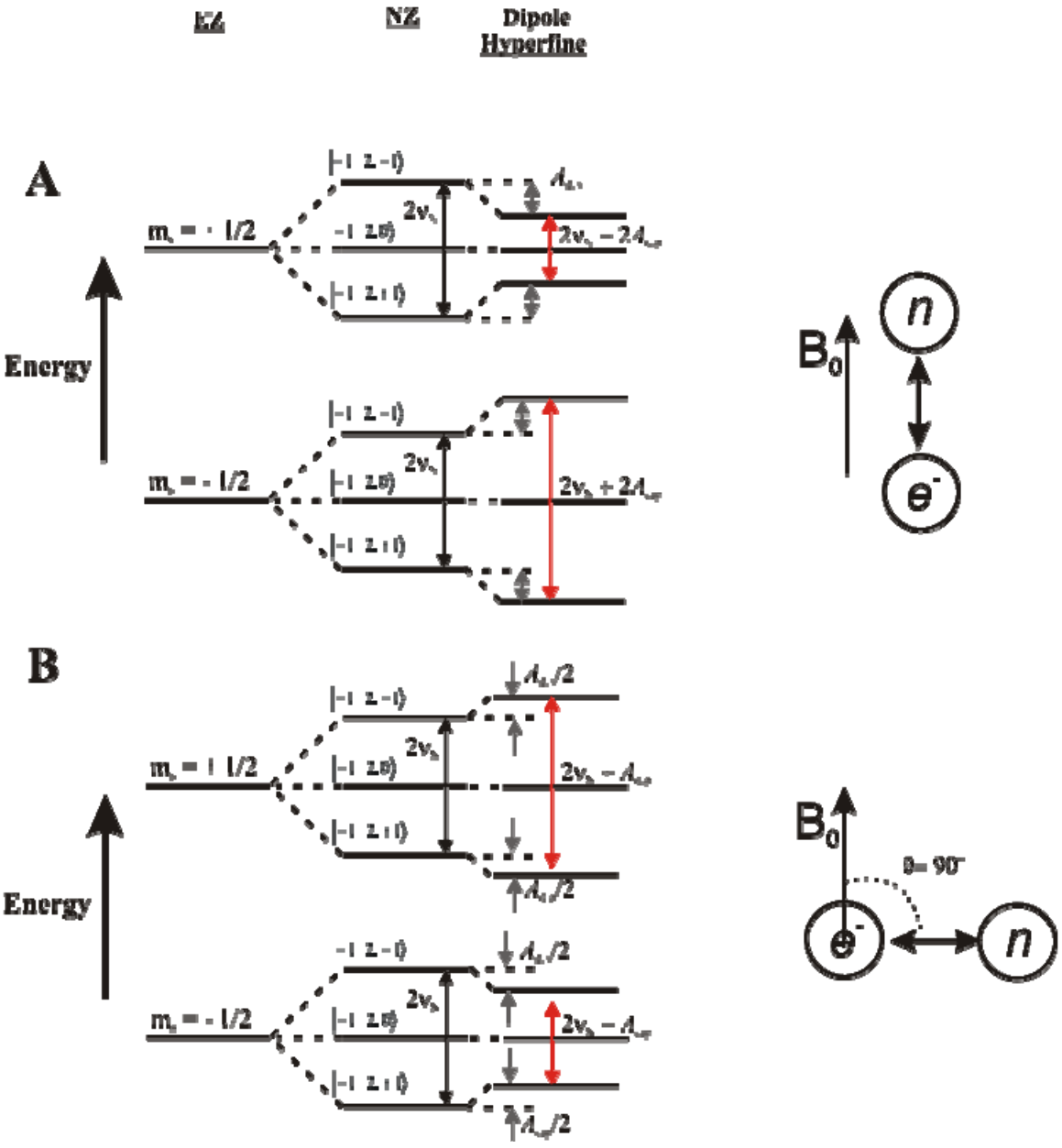

Figure 2.2.4.1 Energy level diagram of the electron Zeeman, nuclear Zeeman, and the dipole hyperfine for case of $S = 1/2$ and $I = 1$.

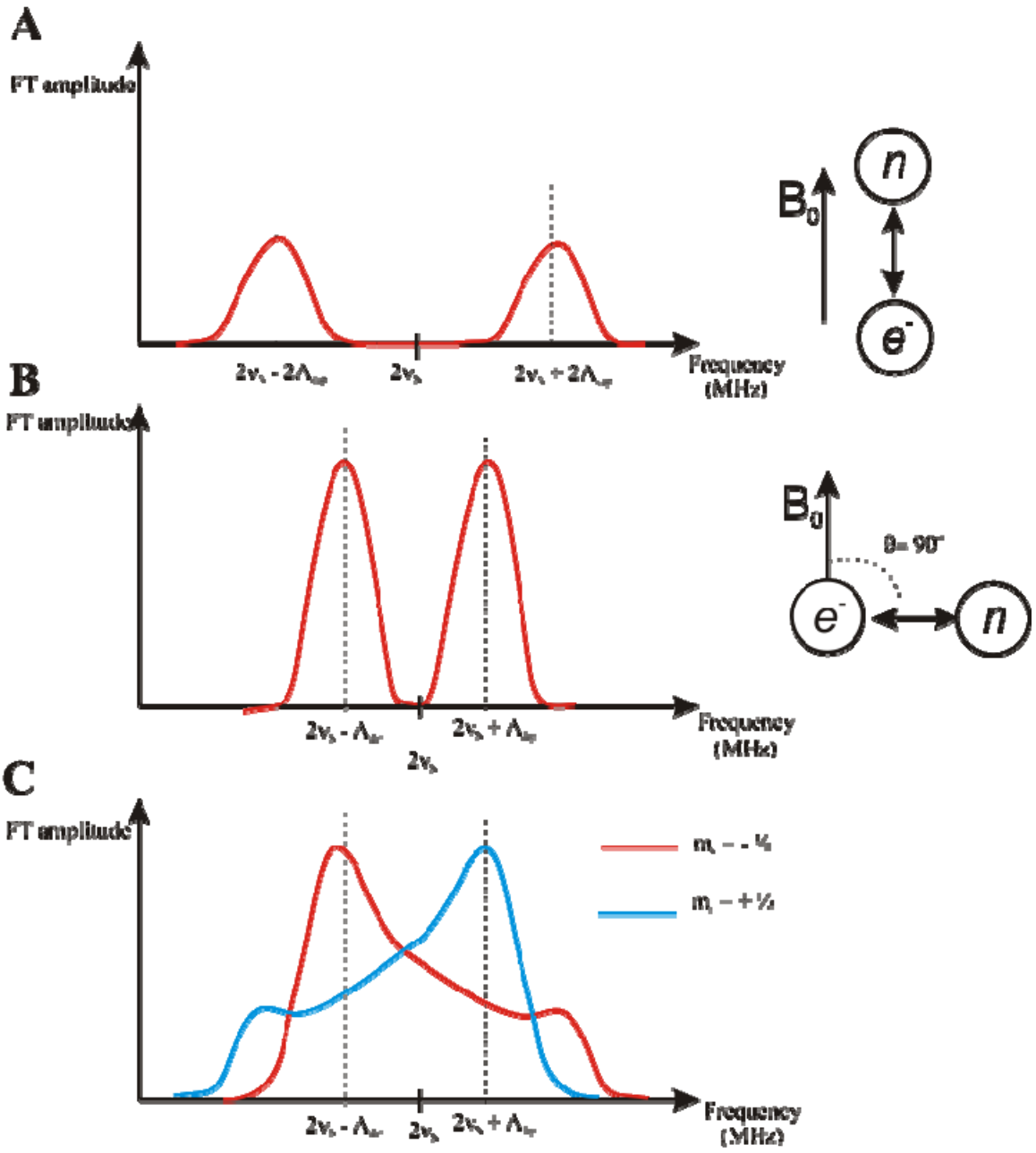

Figure 2.2.4.2 Depiction of the double quantum feature, for the two extremes, **A**. 0° **B**. 90° and **C.** the powder position, where all the angles are present.

The energy diagrams for the two extreme cases (i.e. 0°, 90°) are shown in Figure 2.2.4.1. The lineshape of the double quantum, ν_{dq}, feature is depicted in Figure 2.2.3.2. The difference between the two cases (i.e. 0°, 90°) is the polar angle between the magnetic field, and the electron-nucleus dipolar vector. At the powder position (when all angles are considered), the ν_{dq} lineshape is skewed either towards lower or higher frequencies depending on the energy level manifold being considered. If the $m_s = 1/2$ is considered, the powder pattern for ^{14}N of the ν_{dq} is skewed to higher frequencies (i.e the 90° is at higher frequency). For ms = - 1/2 , the ν_{dq} feature is inversed to the other manifold; the ν_{dq} is skewed to lower frequencies.

In ESEEM spectroscopy, angle-selection has been observed and, in some cases, the orientation of the nitrogen quadrupole coupling tensor with respect to the *g* principal axes has been estimated.[89] All of the analyses for the ESEEM spectra have been made with computer simulations, under the condition of exact cancellation.[83,88-89] In this case one of the m_s manifolds is expressed by a nearly pure quadrupole Hamiltonian because the nuclear Zeeman energy nearly cancels the nitrogen hyperfine interaction energy. This will give rise to a strong ESEEM effect and the frequencies are insensitive to the molecular orientation with respect to the external magnetic field.

Studies have shown that the orientation of the quadrupole coupling tensor to the external magnetic field strongly affects the branching of the electron spin excitations.[83] The intensity of the double quantum transition line is strongly affected by the orientation of the quadrupole coupling tensor with respect to the magnetic field.[89] When the field is in the $g_{||}$ region of the EPR spectrum, the ESEEM spectrum shows a weak double

quantum transition feature. This line increases in intensity as the magnetic field position moves from low field to high field ($g_{\perp}$ region). Changes in the double quantum can be used to estimate the orientation of the imidazole-type-ligand plane in the molecular framework.[66,81,89,92,94]

2.2.5 Double quantum harmonic analysis

ESEEM and angle-selective spectral simulations have been use to characterize the magnetic interaction between the Cu(II) and weakly coupled magnetic nuclei (^{14}N) for the metal binding site.[88-89,95] As mentioned previously, at "exact cancellation", for one of the m_s manifolds, the the energy splitting is solely determined by the nuclear quadrupole interactions. Furthermore, the nuclear quadrupole interaction is independent of the magnetic field strength, and direction.

For the other m_s manifold, the nuclear Zeeman and electron-nuclear superhyperfine interactions are additive, giving rise to the double quantum modulation, and corresponding line in the Fourier transform. The double quantum modulation, as demonstrated by Ohba et al.[89] is dependent on the magnetic field strength, and the microwave frequency.

ESEEM is capable of distinguishing the number of nuclei coupled to the metal, through the combination lines. The combinantion line arising from the double quantum modulation of two coupled ^{14}N, known as "double quantum harmonic", is sensitively

dependent on the orientation of the superhyperfine principal axis systems of the coupled ^{14}N. As depicted in the energy diagram, (Figure 2.2.5.1A), for a single ^{14}N, the double quantum transition is formed. When there are two ^{14}N, the transitions from each nucleus add together to produce the double quantum harmonic transition, $2\nu_{dq}$. This feature is expected to be approximately double the value of the double quantum frequency. Additionally, the $2\nu_{dq}$ lineshape can provide information on the relative orientation of the imidazole planes. As shown in Figure 2.2.5.1B-C, bis-Cu(II)-imidazole has two possible conformations, the bis-*trans* and bis-*cis*. The magnetic field configuration with respect to the studied system will be unique in each case. For the bis-*trans* (Figure 2.2.5.1B), the molecule will have both axes of the imidazole ligands aligned with the magnetic field. Whereas, for the bis-*cis* case (Figure 2.2.5.1C), there is only one of the imidazole ligands that aligns with the magnetic field.

ESEEM spectroscopy can be used to identify imidazole as a metal ligand in copper proteins, and to identify the number of imidazoles that are equatorially coordinated. In addition, the method is particularly useful for describing the structure of the local environment for the ^{14}N imidazole through the study of the nuclear quadrupole interactions and the superhyperfine terms.

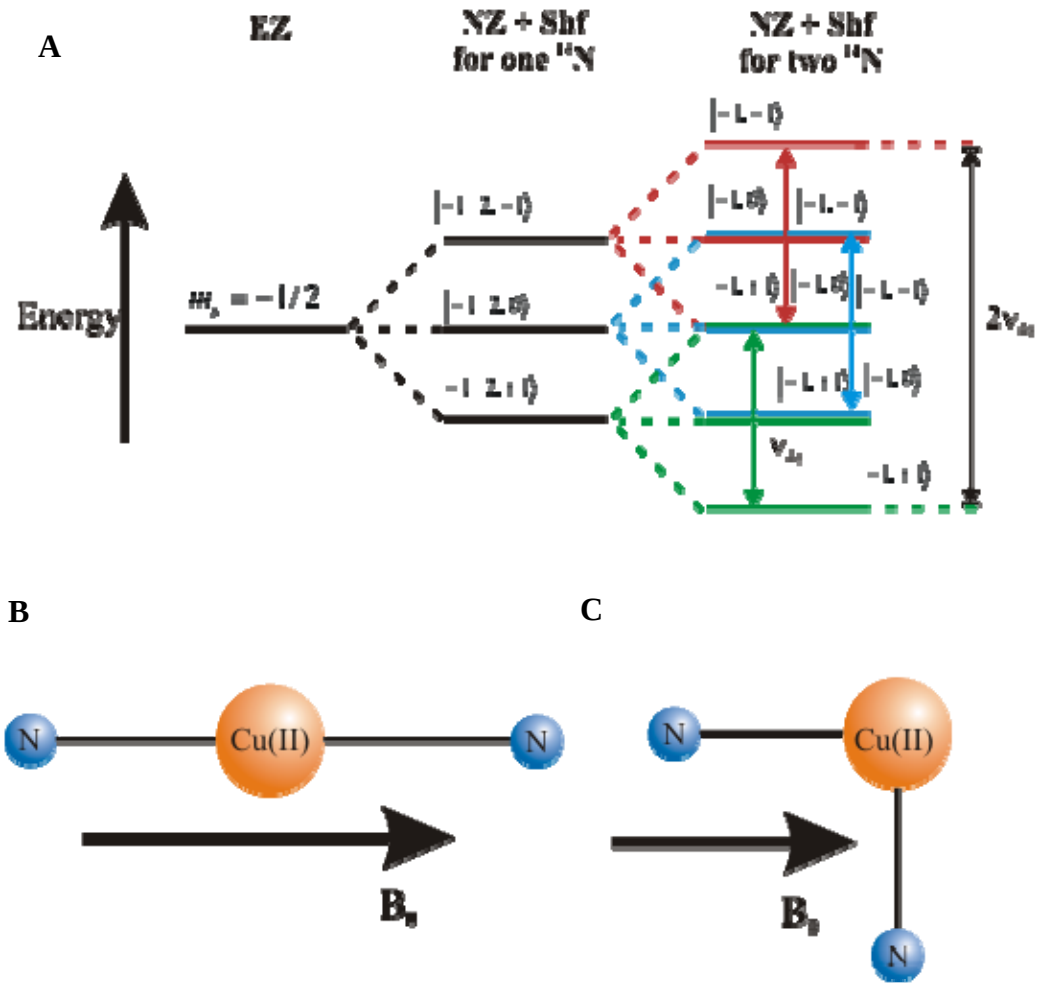

Figure 2.2.5.1 A. Electron spin energy level diagram for m_s=-1/2 of the ^{14}N manifolds. Origin of the double quantum harmonic feature. Alignment of the magnetic field for **B**. bis-*trans* and **C**. bis-*cis* conformation.

Chapter 3: Selection and synthesis of Cu(II) model complexes

3.1 Cu(II) model complexes

Three Cu(II) complexes have been prepared to serve as models for different Cu(II)-histidine imidazole coordination states in Aβ peptide: a single imidazole complex [Cu(II) diethylenetriamine 2-methylimidazole],[81] and two different bis-imidazole complexes: bis-*trans* imidazole [Cu(II)-bis-histamine-bis-nitrate],[96] and bis-*cis* imidazole, [Cu(II)-bis-(acetate)-bis-(2-methylimidazole)].[97] The X-ray crystallographic structure for each of the three Cu(II) complexes is shown in Figure 3.1.1. All chemicals used in the syntheses were obtained from commercial sources (Sigma-Aldrich or Fisher) and used without further purification.

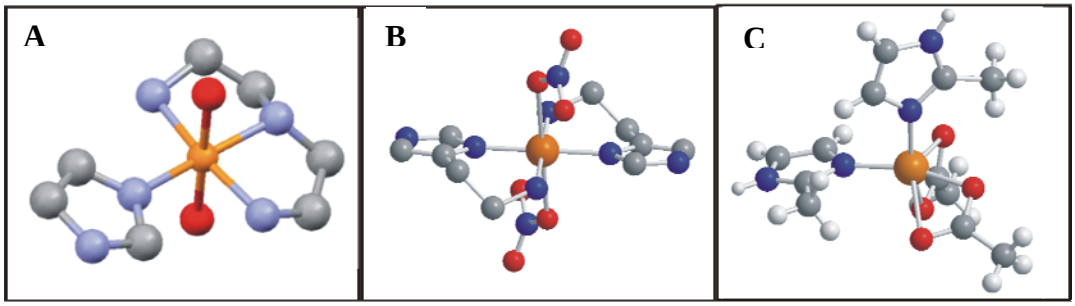

Figure 3.1.1 X-ray crystallographic structure of **A.** the single imidazole [Cu(II) diethylenetriamine 2-methylimidazole],[81] **B.** the bis-*trans* imidazole [Cu(II) $(Him)_2(NO_3)_2$],[96] **C.** the bis-*cis* imidazole [Cu(II)$(2\text{-MeIm})_2(OAc)_2$][97]

Single imidazole: Cu(II)(Dien)(2-MeIm). The Cu(II)(Dien)(2-MeIm) complex was prepared as described by McCracken et al.[81] Briefly, copper(II) diethylenetriamine acetate (2.6 mg), copper(II) acetate (5.0 mg), and 2-methylimidazole (41.0 mg) were

mixed in 5 ml of water at room temperature for one minute. One ml of the mixture was added to 1 ml of ethylene glycol to form a 1:1 ethylene glycol/water solution. The pH was adjusted to 8.0 by adding hydrochloric acid or/and potassium hydroxide. The solution was then frozen in liquid nitrogen to a glass in a 4 mm outer diameter quartz EPR tube, and stored in liquid nitrogen (77 K).

Bis-trans imidazole: $Cu(II)(Him)_2(NO_3)_2$. The $Cu(II)(Him)_2(NO_3)_2$ complex was prepared according to Zhang et al.[96] Briefly, 25.95 mg of histamine dichloride and 0.28 ml of 1 M sodium hydroxide dissolved in 2.72 ml of water was added to 3.93 ml of ethanol containing 0.07 ml of 1 M copper(II) nitrate 3-hydrate. The mixture was then added to 7 ml of ethylene glycol, placed in a 4 mm outer diameter quartz EPR tube, frozen in liquid nitrogen to a glass and stored at 77 K.

Bis-cis imidazole: $Cu(II)(2\text{-}MeIm)_2(OAc)_2$. The $Cu(II)(2\text{-}MeIm)_2(OAc)_2$ complex was prepared as described by Abuhijleh et al.[97] One gram of 2-methylimidazole and 0.5 g of Cu(II) acetate were dissolved in 10 ml of chloroform and 2.5 ml of methanol. The mixture was stirred for 30 min at 50 °C. The mixture was filtered, and 15 ml of ether was added to the filtrate. The filtrate was stirred again for 10 min, followed by the addition of 5 ml of ether. The solution was filtered under reduced pressure and washed with ether and chloroform. The solid was air dried, and recrystallized from methanol ether. The crystals were dissolved in 1:4 methanol/chloroform in a 4 mm outer diameter quartz EPR tube, then frozen in liquid nitrogen to a glass and stored at 77 K.

3.2 Aβ peptides

As previously mentioned in Chapter 1, Aβ is comprised of 39 to 43 residues, depending upon where the *β*- and *γ*- secretases cleave Aβ from the APP *in vivo*.[4,98] Most commonly, Aβ is constituted of either 40 or 42 residues. *In vivo*, Aβ molecules are organized into insoluble fibrils with a diameter of approximately 6-10 nm.[24] Similar amyloid fibrils are also formed by synthetic Aβ *in vitro*.[99] Structural studies of amyloid fibrils have focused primarily on truncated forms, as well as mutated versions of the truncated polypeptides.[36,38,57,100] These truncated versions of Aβ have provided novel insight into the mechanistic issues of amyloid formation, revealing that different truncated versions of peptides contain all of the necessary molecular information for forming typical amyloid fibrils.[101] Aβ(1-40) is capable of aggregating into different structures depending on the assembly conditions,[102] often making the analysis of this peptide difficult. Therefore, to simplify the study of Cu(II) binding to Aβ fibrils, different Aβ(13-21) complexes were prepared, because they form homogeneous fibrils. This truncated version, Aβ(13-21), was used because both hydrophilic and hydrophobic regions are present, which mimic the full length Aβ. Also, this truncated version has the segment that is responsible for aggregation (residues 17-21). Furthermore, in order to isolate His-13/14 as the sole metal binding site, the Lys16 was replaced with Ala, giving Aβ(13-21)K16A. Substitution of Lys16 with Ala not only eliminates possible binding interference, but also amplifies the hydropobicity and amphiphilicity of the peptide, which are important features for fibril formation.[25] Aβ(13-21) peptide assembles into

typical amyloid fibrils.[38-39] When Cu(II) binds to Aβ(13-21)K16A, the fibrils dissolve, suggesting that Cu(II) inhibits the assembly of the fibrils by forming a complex with the Aβ(13-21) momer, in which a backbone amide nitrogen is deprotonated.[38] Therefore, to prevent Cu(II) from binding intramolecularly, a peptide with an acetylated terminal amino group was designed. The Ac-Aβ(13-21)H14A was prepared, where removal of both His-14 and acetylation of the free amino group limits the ligands that are accessible to Cu(II) in each peptide molecule. Thus, Cu(II) is only able to bind to His-13. The characteristic β-sheet signature observed for Aβ(13-21)K16A, obtained by the CD spectra,[38] was similar for the Ac-Aβ(13-21)H14A peptide.

Another truncated version studied was Aβ(1-16). Damante et al. proposed that the N-terminus is the primary Cu(II) binding site by using potentiometric and spectroscopy data.[103] Therefore, this truncated peptide is a suitable model to study the interaction of transition metal ions with the Ab(1-40).[104] Studies have shown that the full-length peptide Aβ(1-40) and the C-terminal truncated versions, Aβ(1-16) and Aβ(1-28), all bind with a high affinity to Cu(II) with the same coordination environment.[63,105] Unlike Aβ(1-40), Aβ(1-16) does not fibrillize, because it does not have the core segment (residues 17-21) needed for fibrillization. Therefore, Aβ(1-16) makes an ideal model for high-resolution spectroscopic studies of the Cu(II) coordination environment.

The full length peptide, Aβ(1-40), was also studied. Aβ(1-40) is capable of aggregating in different structural forms depending on the assembly conditions.[102] However, careful manipulation of the peptide can control aggregation and heterogeneity

in the fibrils that are formed. The study of the Cu(II)-Aβ(1-40) interactions allows for a closer comparison to the *in vivo* conditions.

Synthesis of Aβ(13-21) peptides: The Aβ(13-21) peptides were obtained from Dr. Jijun Dong in the Chemistry Department at Emory University (Prof. David G. Lynn's laboratory). The Aβ(13-21) peptide was synthesized, as described by Dong et al.[38] The peptide was dissolved in buffer containing 25 mM HEPES and 10 mM NaCl (pH 7.2). After incubating the sample with no agitation for two weeks at room temperature, fibrils were produced, as verified by electron microscopy.[38] The Cu(II)/Ac-Aβ(13-21)H14A ratio was 2:1, where the fibrils were formed in the presence of Cu(II). Samples for EPR and ESEEM were mixed with an equal volume of ethylene glycol, transferred to a 4 mm outer diameter quartz EPR tube, then frozen in liquid nitrogen to a glass and stored in liquid nitrogen. The peptide Aβ(13-21)K16A was synthesized as described previously.[38] The peptide was dissolved in buffer containing 25 mM MES (pH 5.6), 10 mM NaCl and in the presence of Cu(II). The Cu(II)/ Aβ(13-21)K16A ratio was 1:1.

Synthesis of Aβ(1-40) peptide: The Aβ(1-40) peptide was synthesized by Dr. Jesse Karr in the Chemistry and Biochemistry Department at the University of Maryland (Prof. Veronika A. Szalai's Laboratory), following the protocol previously described by Karr et al.[43,57-58,63] The peptide was monomerized with hexafluoro-2-propanol (HFIP) and stored at – 80 °C in HFIP. Immediately prior to use of peptide, HFIP was removed using spin-vacuum system. The labeled peptide (^{13}C-^{15}N-H13 and ^{13}C-^{15}N-H14) was donated by Dr. Robert Tycko (National Institutes of Health, Bethesda, MD).

The soluble Aβ(1-40) was prepared by dissolving dried peptide in buffer containing 100 mM Tris, 150 mM NaCl, at a pH 7.4, and 50% glycerol (v/v). The peptide was resuspended in buffer, an aliquot of the sample was removed for peptide concentration determination. Afterwards, a Cu(II) stock solution in buffer was added to a ratio of 1:1. The sample was transferred to a 4 mm outer diameter quartz EPR tube, then frozen in liquid nitrogen to a glass and stored at 77 K.

For the fibrillar Aβ(1-40), the samples were prepared with the same protocol as the soluble peptide, and then incubated at 37 °C for 7-14 days without agitation and in the presence of Cu(II) (ratio of 1:1). Then, the samples were assayed for fibril formation by transmission electron microscopy and thioflavin T fluorescence. Samples for EPR and ESEEM were formed in 100 mM tris, 150 mM NaCl, at a pH 7.4 with 50% glycerol (v/v), and resuspended in 100 μL of the same buffer. The sample was transferred to a 4 mm outer diameter quartz EPR tube, then frozen in liquid nitrogen to a glass and stored at 77 K.

Synthesis of Aβ(1-16) peptide: The Aβ(1-16) peptide was synthesized by Dr. Karr in the Chemistry and Biochemistry Department at the University of Maryland (Prof. Veronika A. Szalai's Laboratory), following the same procedure described above for the Aβ(1-40).

Chapter 4: Applications of $2\nu_{dq}$, double quantum harmonic, analysis to Cu(II) model and Cu(II)-Aβ complexes

4.1 Motivation

A morphological hallmark of AD is the accumulation of the amyloid-β protein (Aβ) in plaques and neurofibrillary tangles in the human brain.[106] The divalent metal ions, Zn(II) and Cu(II), have been found at elevated concentrations (0.4 mM compared to 0.1 mM) in Alzheimer's plaques,[37,107] and the association of Aβ with metal ions has been correlated with AD.[107-109] Metal ions have also been shown to be correlated with amyloid aggregation in the neurodegenerative diseases, prion disease,[110-112] and Parkinson's disease.[113-114] *In vitro* studies have shown that Zn(II) and Cu(II) ions accelerate or arrest fibrillization, depending upon the length and amino acid sequence, in truncated and mutated Aβ peptides, and that the metal ions can alter the morphology of fibrils formed from these peptides.[115] Promotion of fibril formation by Cu(II) is correlated with the number of equatorial histidine imidazole (Im) ligands [Aβ(13-21)K16A, mono-Im; Ac-Aβ(13-21)H14A, bis-imidazole],[115] and Cu(II) bridging of β-strands in the β-sheets that combine to form the fibril has been proposed. Multiple Cu(II)-histidine Im coordination has been reported for other truncated Aβ and for full length Aβ[48,51,105,116–118] Therefore, revealing the molecular basis of fibrillization in Aβ(13-21) and other Aβ peptides requires a description of the structure of the equatorial Cu(II) coordination.

We have developed an approach using the electron spin echo envelope modulation (ESEEM) technique of pulsed-electron paramagnetic resonance (EPR) spectroscopy[71,119-120] to determine the three-dimensional geometry of Cu(II)-bis-histidine

imidazole coordination cryotrapped Cu(II) model and Aβ(13-21) complexes. As shown schematically in Figure 4.1.1, the structural information desired includes specification of bis-*cis* or bis-*trans* coordination, and the mutual orientation of the two imidazole rings.

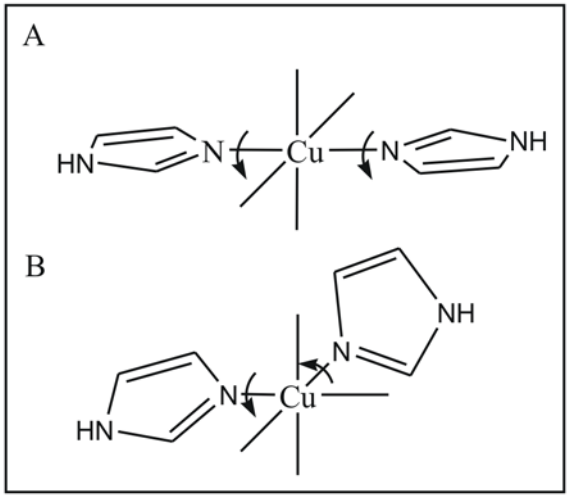

Figure 4.1.1 Depiction of the equatorial bis-*trans* and bis-*cis*-imidazole coordination of Cu(II) and rotational degrees of freedom of the imidazole group. A. Cu(II)-bis-*trans*-imidazole. B. Cu(II)-bis-*cis*-imidazole.

4.2 EPR Spectroscopy of Cu(II)-imidazole model complexes and Aβ peptides.

Figure 4.2.1 shows the continuous-wave X-band powder EPR spectra of Cu(II)(Dien)(2-MeIm), Cu(II)$(Him)_2(NO_3)_2$, Cu(II)$(2\text{-MeIm})_2(OAc)_2$, Cu^{2+}-Aβ(13-21)K16A, and Cu^{2+}-Aβ(13-21)H14A. The spectra are characteristic of a nominally square-planar Cu(II) complex, and show resolved copper hyperfine splitting, which is centered at $g_{||}$, from interaction of the unpaired electron spin with the I = 3/2 copper

nucleus.[69,121] The amplitudes of the powder EPR spectra are greatest around the $g_{\perp} \approx 2$ region. This corresponds to the position of the external magnetic field of 3030 Gauss that was used to achieve the maximum ESE amplitude in the ESEEM experiments.

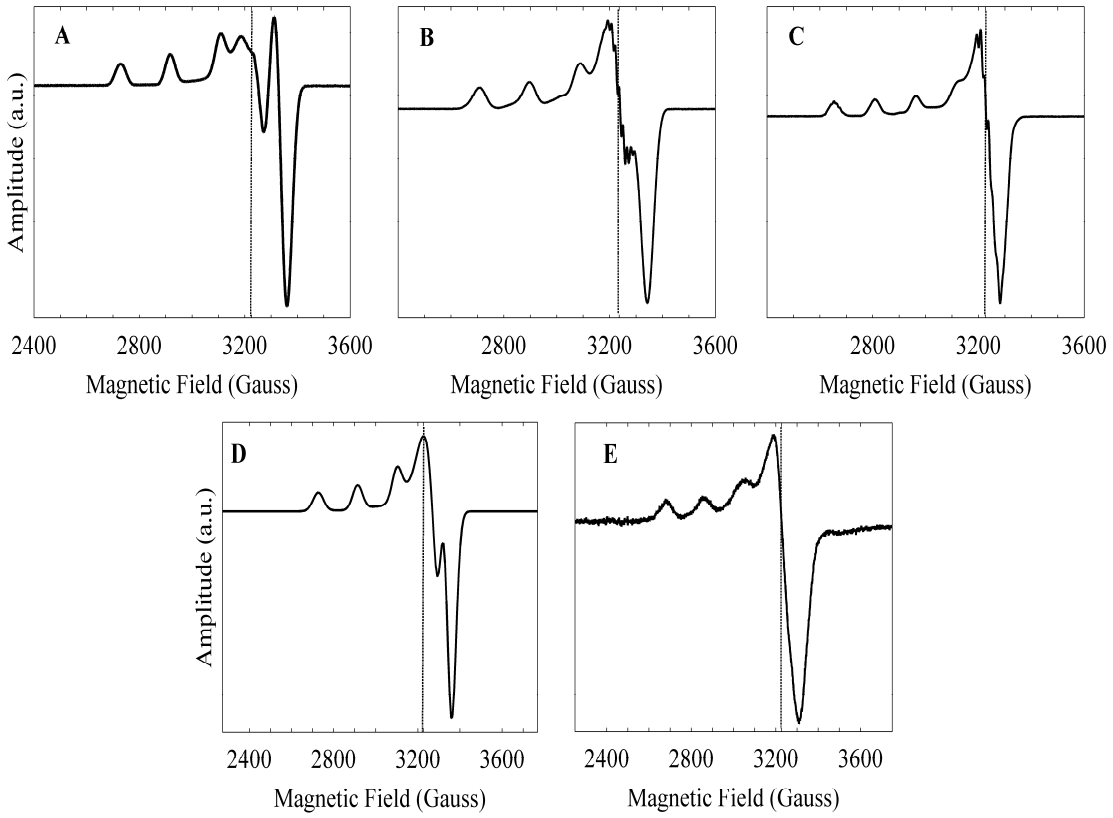

Figure 4.2.1 X-band continuous-wave EPR spectra of Cu(II)-imidazole model and Aβ(13-21) complexes. **A.** [Cu(II)(Dien)(2-MeIm)]. **B**. [Cu(II)$(Him)_2(NO_3)_2$] **C**. [Cu(II)$(2\text{-}MeIm)_2(OAc)_2$]. **D.** [Cu^{2+}-Aβ(13-21)K16A]. **E.** [Cu^{2+}-Aβ(13-21)H14A]. The vertical dashed line shows the position of the magnetic field that corresponds to the ESEEM collection, scaled for the different microwave frequencies used in the CW-EPR and ESEEM experiments. *Conditions*: microwave frequency, 9.3411 GHz; microwave power, 2 mW; microwave attenuation, 20 dB; magnetic field modulation 1.5 G; modulation frequency, 100 kHz; field sweep rate, 1.5 G s^{-1}; time constant, 2.56 ms; temperature, 120 K for model complexes and 165 K for Aβ(13-21) peptides; average of 12 sweeps, minus average of 12 baseline spectra.

4.3. ESEEM Spectroscopy

4.3.1 ESEEM results for Cu(II) model complexes.

Figure 4.3.1.1.1-2 shows the powder three-pulse ESEEM waveform and corresponding FT for the mono-imidazole complex, Cu(II)(dien)(2-MeIm), and the bis-*cis*-imidazole complex, Cu(II)(2-MeIm)$_2$(OAc)$_2$. The ESEEM was collected at the maximum ESE amplitude in the EPR spectrum, and at a τ value of 310 ns. ESEEM at different τ and microwave frequency/magnetic field values has previously been reported for the Cu(II)(dien)(2-MeIm) complex.[122] The ESEEM in Figure 4.3.1.1 exhibits a pattern of deep and sustained modulation in the time domain, and corresponding narrow lines in the frequency domain, which is characteristic of coupling to ^{14}N under the condition of exact cancellation, and specifically, to the remote nitrogen of imidazole.[123-124] The exact cancellation condition holds when the ^{14}N superhyperfine and ^{14}N nuclear Zeeman contributions approximately cancel for one electron spin manifold ($A/2 \approx \nu_N$, where ν_N is the free nuclear frequency), which creates a near zero-field condition in one electron spin manifold (the m_s=+1/2, or α-, manifold, for A_{iso}>0). The energy level separations in this manifold are dominated by the nuclear quadrupole interactions.

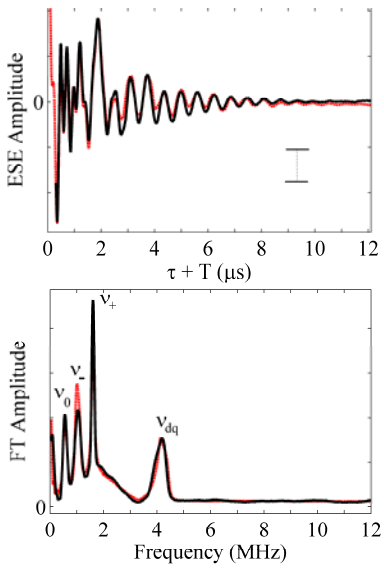

Figure 4.3.1.1 Experimental powder three-pulse ESEEM (upper panel) and Fourier transform (lower panel) for single imidazole [Cu(II)(Dien)(2-MeIm)], and overlaid simulation (red dashed curve). In the ESEEM spectrum (upper panel), the vertical scale bar corresponds to 25% of the constant echo amplitude at τ + T = 12μs. Simulation parameters are presented in Table 4.3.1. *Experimental conditions:* sample temperature, 6 K; microwave frequency, 8.772 GHz; magnetic field strength, 3030 Gauss; initial τ value -190 ns; τ increment, 20 ns; π/2 pulse width, 20 ns; pulse repetition rate, 120 Hz; 64 pulses per repetition; average of 2 accumulations as field noted.

The ESEEM FT for Cu(II)(dien)(2-MeIm) in Figure 4.3.1.1A shows three narrow lines positioned at 0.55, 1.04, and 1.61 MHz, which correspond to the ν_0, ν_-, and ν_+ nuclear quadrupole interaction frequencies, as shown by the close approximation to the expected relation, $\nu_0+\nu_-=\nu_+$. The broad feature, centered at 4.2 MHz, corresponds to the $\Delta m_I=\pm2$, or "double quantum" (ν_{dq}), splitting in the electron spin manifold in which the ^{14}N superhyperfine and nuclear Zeeman contributions are additive. The broadening of this feature arises from the dipolar superhyperfine coupling. The features corresponding to the $\Delta m_I=\pm1$ splittings, which overlap the ν_0, ν_-, and ν_+ features, are broadened by the

dipolar anisotropy, and are generally not resolved in exact cancellation ESEEM. There are no features at frequencies higher than ν_{dq}.

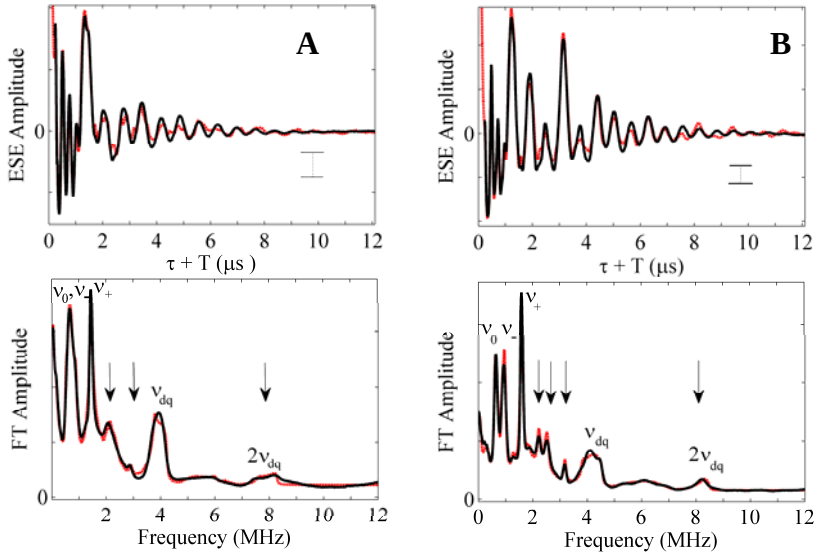

Figure 4.3.1.2 Experimental powder three-pulse ESEEM (upper panel) and Fourier transform (lower panel) for Cu(II)-bis- imidazole A. Bis-*trans* $[Cu(II)(Him)_2(NO_3)_2]$, and overlaid simulation (red dashed curve). B. Bis-*cis* $[Cu(II)(2\text{-}MeIm)_2(OAc)_2]$, and overlaid simulation (red dashed curve). In the ESEEM spectrum (upper panel), the vertical scale bar corresponds to 25% of the constant echo amplitude at $\tau + T = 12\mu s$. In the Fourier transform panel, arrows indicate combination lines that correspond to the labeled fundamental lines. Simulation parameters are presented in Table 4.3.1. *Experimental conditions for both samples:* sample temperature, 6 K; microwave frequency, 8.772 GHz; magnetic field strength, 3030 Gauss; initial τ value -190 ns; τ increment, 20 ns; $\pi/2$ pulse width, 20 ns; pulse repetition rate, 120 Hz; 64 pulses per repetition; average of 2 accumulations as field noted.

The powder three-pulse ESEEM waveform and FT for $Cu(II)(Him)_2(NO_3)_2$, collected at the maximum ESE amplitude in the EPR spectrum, and at a τ value of 310 ns, is shown in Figure 4.3.1.2.A. The ESEEM in Figure 4.3.1.2 shows the characteristic exact cancellation pattern of coupling to the remote ^{14}N of the two imidazole rings.[123-124] The ESEEM FT in Figure 4.3.2.A shows unresolved ν_0 and ν_- lines in a single feature at

0.65 MHz, and the ν_+ line at 1.42 MHz. The ν_{dq} feature has maximum amplitude at 3.86 MHz. The discrete character of the narrow nuclear quadrupole interaction fundamental features (line widths comparable to the corresponding features in Figure 4.3.1.1) indicates that the two remote ^{14}N nuclei have the same superhyperfine and nuclear quadrupole interaction couplings, to within the resolution of the ESEEM experiment.

In addition to these "fundamental" features, which are also found for the Cu(II)-mono-imidazole complex ESEEM in Figure 4.3.1.1, the Cu(II)-bis-imidazole ESEEM shows relatively low amplitude "combination" lines that are positioned at sums of the fundamental frequencies. The combination lines are marked by arrows in Figure 4.3.1.2. These combination features arise from relatively low-probability, simultaneous nuclear spin transitions among the two remote imidazole ^{14}N nuclear spin states. Prevalent features are observed at 2.09 MHz ($\nu_0/\nu_- + \nu_+$) and 2.90 MHz ($2\nu_+$). The weak feature from approximately 7.0 to 8.5 MHz represents the $2\nu_{dq}$, double quantum combination, which corresponds to the combination of the $\Delta m_I=\pm 2$ splittings in the non-cancellation electron spin manifold of each remote ^{14}N. The enhanced broadening, relative to the ν_{dq} feature, arises from the anisotropic component part superhyperfine coupling of both ^{14}N. Therefore, this feature contains information about the mutual orientation of the dipolar superhyperfine principal axis system of the remote ^{14}N.

ESEEM from $Cu(II)(Him)_2(NO_3)_2$ was collected at other τ values (156, 234, 388, 466, 542, 620 ns) in addition to 310 ns. These τ values correspond to τ-suppression[125] of the large free ^1H contribution to the ESEEM ($\tau = n/\nu_n$ where ν_n is the free proton nuclear Zeeman frequency, and n = 1, 2, 3, …). The $2\nu_{dq}$ feature achieved the largest amplitude

at τ values of 310 ns and 622 ns, but was near to, or within, the noise amplitude at the other τ values. The τ value of 310 ns was selected for analysis, because the shorter time period of the phase memory decay in the pulse-swapping sequence afforded the best signal-to-noise ratio, relative to $\tau = 622$ ns.

The powder three-pulse ESEEM waveform and FT for $Cu(II)(2\text{-}MeIm)_2(OAc)_2$, collected at the maximum ESE amplitude in the EPR spectrum, and at a τ value of 310 ns, is shown in Figure 4.3.1.2.B. The ESEEM in Figure 4.3.1.2.B also shows the characteristic exact cancellation pattern of coupling to the remote ^{14}N of the two imidazole rings.[123-124] The FT in Figure 4.3.1.2B shows the fundamental nuclear quadrupole interaction ν_0, ν_-, and ν_+ lines at 0.61, 0.91, and 1.57 MHz, respectively. The ν_{dq} feature has maximum amplitude at 4.08 MHz. The three nuclear quadrupole interactions and the ν_{dq} lines appear at positions that are different from those for the $Cu(II)(Him)_2(NO_3)_2$ complex, which shows a subtle difference in the electronic structure around the remote ^{14}N in the two complexes, as expected from the difference in position of the alkyl substitution on the Im ring. In Figure 4.3.1.2.B, the combination lines are observed at 2.20 ($\nu_0 + \nu_+$), 2.49 ($\nu_- + \nu_+$), and 3.16 ($2\nu_+$) MHz. The $2\nu_{dq}$, double quantum combination feature has a maximum amplitude at 8.29 MHz. Comparison of Figure 4.3.1.2.A and Figure 4.3.1.2.B shows that the lineshape of the $2\nu_{dq}$ features for the bis-Im complexes is distinctly different. This difference will be shown, in the analysis, to be caused by the different mutual orientations of the two ^{14}N principal axis system.

Table 4.3.1. ESEEM simulation parameters for the Cu(II)-imidazole model complexes. The best-fit values and the simultaneous confidence region at the 99% confidence level are shown for each adjustable parameter. In the column for each model complex, the best-fit value for each simulation parameter are shown in bold font, and the upper and lower limits of the simultaneous confidence regions for the parameters are given in the right column to the right.

Sample	Cu(II)(Dien)(2-MeIm)		Cu(II)(2-MeIm)$_2$(OAc)$_2$		Cu(II)(Him)$_2$(NO$_3$)$_2$	
A_x (MHz)	**2.41**	2.44 2.38	**2.43**	2.44 2.41	**2.13**	2.16 2.10
A_y (MHz)	**1.94**	1.98 1.88	**1.77**	1.85 1.70	**1.81**	1.85 1.77
A_z (MHz)	**1.42**	1.47 1.38	**1.40**	1.42 1.38	**0.85**	0.88 0.82
e^2qQ/h (MHz)	**1.71**	1.72 1.70	**1.64**	1.64 1.63	**1.51**	1.51 1.50
η	**0.64**	0.65 0.63	**0.72**	0.72 0.71	**0.67**	0.82 0.53
α_Q(°)	**64**	75 54	**20**	24 15	**7**	16 358
β_Q(°)	**22**	27 16	**18**	24 15	**351**	353 349
γ_Q(°)	**20**	32 9	**359**	3 353	**350**	5 335
α_A(°)			**25**	30 14	**177**	168 201
β_A(°)			**132**	143 112	**32**	35 29
γ_A(°)			**312**	320 302	**353**	342 16

4.3.2 ESEEM results for Cu(II)-Aβ complexes

Figure 4.3.2.1 shows the powder three-pulse ESEEM waveform and corresponding FT for the mono-imidazole complex, Cu(II)-Aβ(13-21)K16A. ESEEM at a different τ value (156 ns) has previously been reported for this complex.[115] The ESEEM in Figure 4.3.2.1 is characteristic of coupling to the remote nitrogen of imidazole under the condition of exact cancellation.[123-124] As expected for the mono-imidazole equatorial coordination in Cu(II)-Aβ(13-21)K16A, only the fundamental ESEEM features are observed.

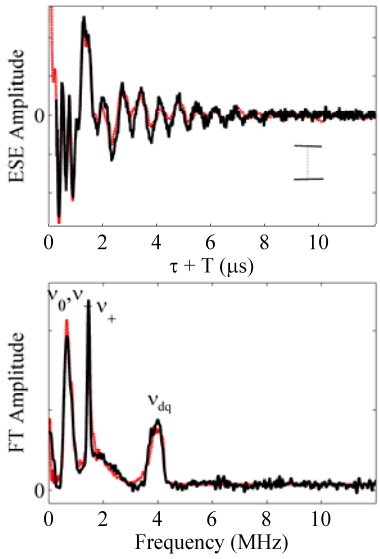

Figure 4.3.2.1 Experimental powder three-pulse ESEEM and Fourier transform for [Cu^{2+}-Aβ(13-21)K16A], and overlaid simulation (red dashed curve). In the ESEEM panel, the vertical scale bar corresponds to 25% of the constant echo amplitude at τ+T=12 μs. Simulation parameters are presented in Table 4.3.2. *Experimental conditions:* sample temperature 6 K; microwave frequency 8.831 GHz, magnetic field strength, 3050 Gauss; initial τ value -190 ns; τ increment, 20 ns; π/2 pulse width, 20 ns; pulse repetition rate, 120 Hz; 64 pulses per repetition; average of 2 accumulations.

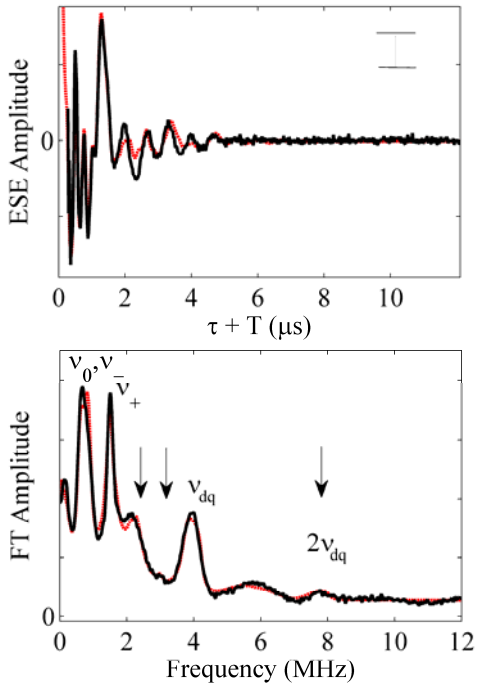

Figure 4.3.2.2 Experimental powder three-pulse ESEEM and Fourier transform for Cu^{2+}-Ac-Aβ(13-21)H14A, and the overlaid simulation (dashed red curve). In the ESEEM panel, the vertical scale bar corresponds to 25% of the constant echo amplitude at $\tau+T$=12 μs. In the Fourier transform panel, arrows indicate combination lines that correspond to the labelled fundamental lines. Simulation parameters are presented in Table 4.3.2. *Experimental conditions:* sample temperature, 6 K; microwave frequency, 8.831 GHz; magnetic field strength, 3050 Gauss; τ value, 310 ns; initial $\tau+T$ value, -190 ns; τ increment, 20 ns; π/2 pulse width, 20 ns; pulse repetition rate, 120 Hz; 64 pulses per repetition; 48 accumulation.

Figure 4.3.2.2 shows the powder three-pulse ESEEM waveform and corresponding FT for the bis-cis-imidazole complex, Cu(II)-Aβ(13-21)H14A. ESEEM at a different τ value (156 ns) has previously been reported for this complex.[115] In addition to the fundamental features, which show overlapping ν_0 and ν_- lines, weak combination lines are observed, which correspond to the ($\nu_0/\nu_- + \nu_+$) and ($2\nu_+$) frequencies, as expected for the previously assigned[115] equatorial bis-histidine imidazole coordination.

The nuclear quadrupole interactions combination features are significantly enhanced in relative amplitude at τ = 156 ns.[115] As shown in Figure 4.3.2.2, the Cu(II)-Aβ(13-21)H14A ESEEM also shows the $2\nu_{dq}$ feature, which has a maximum at approximately 7.8 MHz. The relatively narrow, single peak line shape of the $2\nu_{dq}$ feature is similar to the $2\nu_{dq}$ line shape for the Cu(II)(2-MeIm)$_2$(OAc)$_2$ equatorial bis-cis-imidazole complex, and distinct from the broader $2\nu_{dq}$ line shape of the Cu(II)(Him)$_2$(NO_3)$_2$ complex equatorial bis-trans-imidazole complex.

Table 4.3.2 ESEEM simulation parameters for the Cu(II)-Aβ(13-21) truncated and mutated peptide. The best-fit values and the simultaneous confidence region at the 99% confidence level are shown for each adjustable parameter. In the column for each Cu(II)-Aβ(13-21) peptide, the best-fit value for each simulation parameter are shown in bold font, and the upper and lower limits of the simultaneous confidence regions for the parameters are given in the right column to the right.

Sample	Cu(II)-Aβ(13-21)K16A		Cu(II)-Ac-Aβ(13-21)H14A	
A_x (MHz)	**2.12**	2.17 2.08	**2.12**	2.17 2.07
A_y (MHz)	**1.80**	1.88 1.73	**1.70**	1.76 1.62
A_z (MHz)	**0.90**	0.95 0.86	**1.23**	1.28 1.18
e^2qQ/h (MHz)	**1.51**	1.52 1.50	**1.55**	1.56 1.53
η	**0.71**	0.74 0.70	**0.73**	0.74 0.71
α_Q (°)	**228**	246 217	**59**	68 47
β_Q (°)	**9**	10 7	**22**	27 16
γ_Q (°)	**291**	306 285	**342**	348 334
α_A (°)			**354**	3 330
β_A (°)			**70**	85 59
γ_A (°)			**298**	315 280

4.3.3 ESEEM simulation

Numerical simulations of the ESEEM simulations were performed by using the Matlab-based code in the OPTESIM software package, which we have recently presented and described in detail.[126] The stationary-state spin Hamiltonian for treatment of the interaction of the electron spin (S=1/2) on Cu(II) with the remote ^{14}N nuclear spin (I=1) is formulated with a shf coupling term, a nuclear Zeeman term, and a nqi term, as follows:[127]

$$H = h\vec{S} \cdot A \cdot \vec{I} - g_N \beta_N \vec{B}_0 \cdot \vec{I} + \vec{I} \cdot Q \cdot \vec{I}' \qquad [4.3.3.1]$$

where $\beta_N, \vec{S}$, and $\vec{I}$ are the nuclear magneton, electron spin operator, and nuclear spin operator, respectively, g_N is the nuclear g-value, A is the shf coupling tensor, and Q is the nuclear quadrupole interaction tensor.[128] The I and I' indicate that the eigenfunctions of A and Q are, in general, different. The superhyperfine tensor has the principal components, $A_p = \lfloor A_{xx}\ A_{yy}\ A_{zz} \rfloor$, and is composed of an isotropic part, $A_{iso} = \frac{1}{3}\sum_i A_{ii}$, and a dipolar part, $A_P - A_{iso}$. The nqi tensor, **Q**, is defined by the nuclear quadrupole coupling constant, e^2qQ/h, and the efg asymmetry parameter, η.[129] In its PAS, the traceless nqi tensor $Q_p = \lfloor Q_{xx}\ Q_{yy}\ Q_{zz} \rfloor$ is related to e^2qQ/h and η by the following expressions:

$$Q_{zz} = \frac{e^2qQ}{2I(2I-1)h} \qquad [4.3.3.2]$$

$$\eta = \frac{(Q_{xx} - Q_{yy})}{Q_{zz}} \qquad [4.3.3.3]$$

where $|Q_{zz}| \geq |Q_{yy}| \geq |Q_{xx}|$. In OPTESIM, the orientation between the nuclear quadrupole interaction tensor principal axis system and the hyperfine tensor principal axis system is defined by the Euler angles, $[\alpha_Q \ \beta_Q \ \gamma_Q]$. In systems with more than one coupled nucleus (N>1), the orientation of the superhyperfine principal axis system of each nucleus relative to an arbitrary reference frame is defined by the Euler angles, $[\alpha_A \ \beta_A \ \gamma_A]$. For the two remote ^{14}N couplings in the Cu(II)-bis-imidazole complexes studied here, $[\alpha_A \ \beta_A \ \gamma_A]$ are chosen to define the mutual orientation of the two superhyperfine principal axis system.

The coupled electron – single ^{14}N system is therefore parameterized by using the following eight adjustable parameters: A_{xx}, A_{yy}, A_{zz}, α_Q, β_Q, γ_Q, e^2qQ/h, η. In the Cu(II)-bis-imidazole complexes, the eight parameters are assumed to be common among the two imidazole ^{14}N. The bis-imidazole complexes have α_A, β_A, and γ_A, as additional adjustable parameters. The method of calculation of the simultaneous confidence region for each adjustable parameters, at a specific confidence level (here, 99%), has been described in detail.[126]

The ESEEM calculation in OPTESIM incorporates the full density matrix diagonalization from the Mims density matrix treatment of ESEEM[127,130] for evaluation of the transition frequencies and intensities, but uses a computationally efficient numerical procedure[71-72,131] for constructing the three-pulse modulation. For the case of an isotropic g-tensor, which is well approximated by the nominally octahedral Cu(II)-bis-imidazole complexes near the $g_\perp$ position of the EPR spectrum,[69] a spherical average is calculated. Users of OPTESIM also have the option of simulating the more general case of orientation-selection ESEEM, by

specifying the range and weights of orientation vectors.[126] For more than one coupled nucleus (N>1), the computed spherical average in OPTESIM is performed by using a physical model which includes information about the particular arrangement of coupled nuclei relative to the paramagnet. This geometry is defined by the set of Euler angles, $[\alpha_A \ \beta_A \ \gamma_A]$, for each nucleus, which together specify the mutual orientation of the shf PAS. Therefore, the ESEEM is calculated and combined at each powder orientation. A physical model has been used previously to simulate ^{14}N ESEEM in a metal complex.[132] The three-pulse envelope modulation for the N=2 electron-nuclear couplings is combined separately for the α- and β- electron spin manifolds by using the following product rule:[133]

$$E_{tot}(\tau,T)=\prod_{i}^{N}E_{\alpha i}(\tau,T)+\prod_{i}^{N}E_{\beta i}(\tau,T) \qquad [4.3.3.4]$$

The automated optimization of the simulations used a genetic algorithm, followed by the Nelder-Mead simplex method. The genetic algorithm had a starting population of 300. The genetic algorithm converged after approximately 100 generations, and the best individual was selected as the starting point for the simplex method. Simulations were run in parallel on a collection of personal computers, which were tasked with subsets of the powder orientation sampling vectors, under the Java-RMI based distributed computational framework that is included in OPTESIM.[126].

4.3.4 Simulation of the ^{14}N ESEEM from the different Cu(II) complexes.

Simulations of the ESEEM in Figure 4.3.1.1-2 and Figure 4.3.2.1-2 are shown as dotted red curves. The best-fit simulation parameters, and the simultaneous confidence regions at the 99% confidence level, are presented in Table 4.1-2. Convergence to the global minimum was achieved by using an automated hybrid optimization (genetic algorithm, followed by simplex) approach in the OPTESIM software,[126] as described in section 4.3.3. The principal values of the superhyperfine tensor, and e^2qQ/h and η, for Cu(II)(Dien)(2-MeIm) are comparable to values previously reported.[81] The principal values of the shf tensor, and e^2qQ/h and η, for the two Aβ(13-21) peptides are also comparable to previously reported values, which were based on ESEEM with relatively large amplitude and spectra resolution of the fundamental features that are characteristic of relatively short τ values (for the previous study, of 156 ns).[115] The A_{iso} values for Cu(II)(Dien)(2-MeIm), $Cu(Him)_2(NO_3)_2$, $Cu(II)(2\text{-}MeIm)_2(OAc)_2$, Cu(II)-Aβ(13-21)H14A lie in the range of 1.8-1.9 MHz, and the principal values of the dipolar superhyperfine tensors for the complexes all approximate the [A 0.2A $-A$] form that is common among 2- and 4-alkyl-substituted imidazole ligands to Cu(II).[134-136] Therefore, the electronic structure of the imidazole ring and the coupling of the unpaired spin density with the remote ^{14}N, are relatively constant across the four complexes. The narrow confidence regions for the superhyperfine and nuclear quadrupole interaction parameters in Table 4.1-2 show a high relative certainty for the best-fit values, and indicate that the parameters are strong determinants of the experimental ESEEM (a wide confidence region indicates that the parameter is poorly constrained). The excellent

quality of the simulations and narrow confidence regions for the Cu(II)-bis-imidazole complexes also further support the assumption of comparable superhyperfine and nuclear quadrupole interaction parameters for the two remote ^{14}N in each complex.

4.3.5 Mutual Orientation of Imidazole Ligands in Cu(II) model complexes

4.3.5.1 Mutual Orientation of Imidazole Ligands in the Cu(II)(him)$_2$(NO$_3$)$_2$ Complex

Figure 4.3.5.1.A depicts the physical model of the relative orientation of the superhyperfine principal axis system for Cu(II)(him)$_2$(NO$_3$)$_2$ complex, which is constructed by using the Euler angles in Table 4.1.1. One superhyperfine principal axis system (blue) is fixed, and the other superhyperfine principal axis system (black) is rotated through the Euler angles, [α_A β_A γ_A]. The rotated superhyperfine principal axis system displays the simultaneous confidence intervals at the 99% confidence level. Figure 4.3.5.1.A shows that the *y*-axes are opposed to within the limits of the confidence region, and that the *x*- and *z*-axes deviate from anti-parallel and parallel, respectively, because of a 30° rotation about the *y*-axis. The X-ray crystallographic structure of the Cu(II)(him)$_2$(NO$_3$)$_2$ complex[137] is depicted in Chapter 3 Figure 3.1.1.B. The symmetry of the ESEEM-derived remote ^{14}N superhyperfine principal axis system mutual orientation is consistent with the bis-*trans*-imidazole coordination mode, and with the approximately coplanar orientation of the two imidazole ligand rings that is observed in the X-ray crystallographic structure. In order to quantify the match of the physical model and X-ray

crystallographic structure, we superposed the superhyperfine principal axis system onto the atomic coordinates of the X-ray structure,[137] by using the superhyperfine principal axis system –molecular principal axis system relation derived from the single crystal ESEEM studies.[134-135] The calculated model, shown in Figure 4.3.5.1.B, displays good agreement with the ESEEM-derived model in Figure 4.3.5.1.A. The deviations between the two models in Figure 4.3.5.1 are within the angular range of the confidence intervals for the Euler angles at the 0.99 confidence level (Table 4.1). Therefore, we cannot distinguish between the statistical error in the data, and a possible difference between the structure of the Cu(II)(him)$_2$(NO$_3$)$_2$ complex in the crystal and in the frozen glassy solution state.

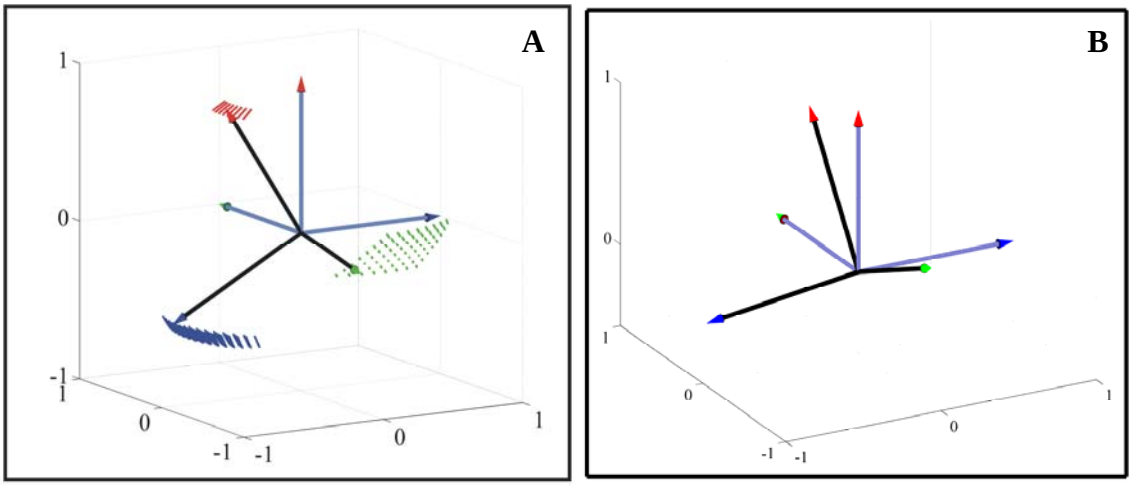

Figure 4.3.5.1 Physical model of the mutual orientation of the two remote ^{14}N shf PAS in [Cu(II)(Him)$_2$(NO$_3$)$_2$]. **A**. Model derived from the powder ^{14}N ESEEM. The hatched surface represents the simultaneous confidence interval at the 99% level of confidence. **B.** Calculated mutual orientation of the imidazole remote ^{14}N shf PAS in the complex, based on the X-ray crystallographic structure and the relation of the shf PAS to the imidazole molecular PAS, which was obtained in single crystal ESEEM studies. Axis color code: *x* (blue), *y* (green), *z* (red).

4.3.5.2 Mutual Orientation of Imidazole Ligands in the Cu(II)(2-MeIm)$_2$(OAc)$_2$ Complex

Figure 4.3.5.2.A shows our physical model of the imidazole remote ^{14}N superhyperfine principal axis system orientations in the Cu(II)(2-MeIm)$_2$(OAc)$_2$ complex, and the structure determined by X-ray crystallography.[138] The relation of the two superhyperfine principal axis system, predicted by using the X-ray crystallographic strucure[138] and the superhyperfine principal axis system –molecular principal axis system relation derived from the single crystal ESEEM studies,[134-135] is shown in Figure 4.3.5.2.B.

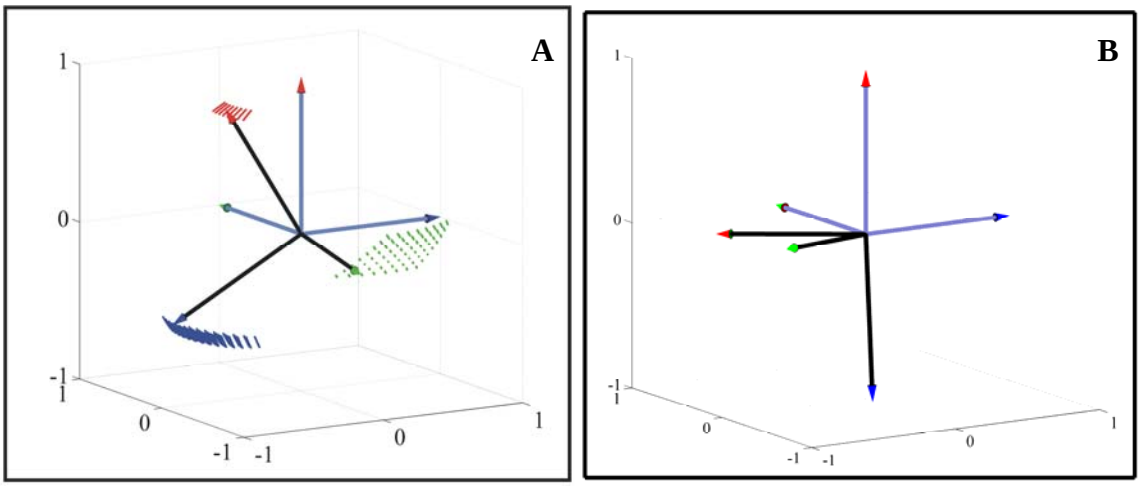

Figure 4.3.5.2 Physical model of the mutual orientation of the two remote ^{14}N shf PAS in [Cu(II)(2-MeIm)$_2$(OAc)$_2$]. **A.** Model derived from the powder ^{14}N ESEEM. The hatched surface represents the simultaneous confidence interval at the 99% level of confidence. **B.** Calculated mutual orientation of the imidazole remote ^{14}N shf PAS in the complex, based on the X-ray crystallographic structure and the relation of the shf PAS to the imidazole molecular PAS, which was obtained in single crystal ESEEM studies. Axis color code: *x* (blue), *y* (green), *z* (red).

Comparison of the Figure 4.3.5.2.A and Figure 4.3.5.2.B shows that the agreement between the ESEEM physical model and the predicted mutual orientation of the superhyperfine principal axis system is good. In particular, the *x*-axes in each model are approximately perpendicular, which is charateristic of the bis-*cis* coordination mode. The deviations from agreement of the ESEEM-derived and calculated structures, beyond the confidence regions of the angular parameters, are likely to be caused by differences between the crystal and solution structures of the complexes. Larger differences of the superhyperfine principal axis system orientations between the crystal and frozen glassy solution structures are expected for the Cu(II)(2-MeIm)$_2$(OAc)$_2$ complex, because rotation of the imidazole rings about the Cu(II)-ligand axis is less constrained, relative to the bidentate Cu(II)(him)$_2$ coordination. A difference in the imidazole rotamer states for the complexes in the crystal and frozen glassy solution is supported by the ability to rotate the two superhyperfine principal axis system in the physical model about the *x*-axes, which coincide with the proximal-N-Cu(II) bond direction, to achieve a very good match with the superhyperfine principal axis system determined for the X-ray crystallographic structure.

4.4 Assessment of the ESEEM Method of bis-Imidazole Coordination Geometry Determination in Cu(II) Complexes.

We have previously reported the physical model for the bis-*trans*-imidazole complex, $Cu(II)(him)_2(NO_3)_2$, and found excellent agreement of this model with the X-ray crystallographic structure. Figure 4.3.5.1.B shows the superposition of the superhyperfine principal axis system for $Cu(II)(him)_2(NO_3)_2$ onto the atomic coordinates of the X-ray structure for $Cu(II)(him)_2(NO_3)_2$,[137] in the manner of Figure 4.3.5.1.A, by using the superhyperfine principal axis system–molecular principal axis system relation derived from the single crystal ESEEM studies.[134-135] The calculated model displays excellent agreement with the ESEEM-derived model. In the case of the bis-*trans*-imidazole complex, the deviations between the two models are within the angular range of the confidence intervals for the Euler angles at the 0.99 confidence level. This is expected for the superhyperfine principal axis system orientations in the crystal and frozen glassy solution, because rotation of the imidazole rings about the Cu(II)-ligand axis is constrained by the bidentate coordination in the $Cu(II)(him)_2$ complex.

The reasonable agreement (within the limits expected for crystal versus glassy frozen solvent conditions) of the powder ESEEM-derived physical models for the mutual orientation of the imidazole remote ^{14}N principal axis system with the mutual orientation calculated from the combined single crystal ESEEM and X-ray crystallographic results demonstrates that the powder ^{14}N ESEEM experiment and numerical simulation approach, based on analysis of the $2\nu_{dq}$ line shape, is capable of accurately specifying the mutual orientation, to within the confidence intervals of the angular parameters.

In contrast, in the general case of a Cu(II)-bis-Im complex of unknown structure and unknown relation of the superhyperfine principal axis system to the imidazole molecular principal axis system, the cis- or trans- coordination mode cannot be uniquely determined. The finding of a rotation matrix with no eigenvalue of -1 does, however, introduce the constraint that the mode is not *trans*. For example, if the two superhyperfine principal axis system of the two imidazoles in a bis-*trans* configuration are related by a rotational matrix **R**, then there must exist a vector **v**, corresponding to the bonding direction of the proximal ^{14}N and Cu(II), such that, when rotated by **R**, becomes –**v**. The relationship, **Rv**=-**v**, requires **R** to have an eigenvalue of -1, corresponding to a 180° rotation about some reference axis. However, an eigenvalue of -1 is not sufficient for the assignment of bis-*trans* configuration. Information about the direction of the proximal ^{14}N-Cu(II) bond relative to the superhyperfine principal axis system is required.

In the case of a known relation of the superhyperfine principal axis system to the imidazole molecular principal axis system, the coordination mode can be uniquely determined, in addition to the mutual orientation of the imidazole molecular principal axis system. Therefore, with the inclusion of the superhyperfine principal axis system–molecular principal axis system correlation from the single crystal ESEEM studies,[134-135] the bis-*cis*- or bis-*trans*-imidazole coordination mode of the complex may be determined.

4.5 Mutual Orientation of Imidazole Ligands in the Cu(II)-Ac-Aβ(13-21)H14A Peptide.

Figure 4.5.1 depicts the physical model of the relative orientation of the superhyperfine principal axis system for Cu(II)-Ac-Aβ(13-21)H14A, which is based on the Euler angles presented in Table 4.3.2. The *x*-axes in the model are approximately perpendicular, as shown by the confidence region for the *x*-axes of 75° to 110°. Perpendicular *x*-axes are characteristic of the bis-*cis*–imidazole coordination mode, as demonstrated above for the $Cu(II)(2\text{-}MeIm)_2(OAc)_2$ complex. Therefore, we conclude that the Cu(II) in fibrils of Ac-Aβ(13-21)H14A is coordinated in the equatorial plane by two histidine imidazoles in the *cis* geometry. The ability to simulate the results by using a discrete model of Cu(II)-remote ^{14}N coupling (single set of superhyperfine, nuclear quadrupole interaction, and orientational simulation parameters), indicates a well-ordered and singular interaction of Cu(II) with the Ac-Aβ(13-21)H14A peptide in the fibril, on the molecular scale. This is consistent with the homogeneous fibril morphology on the mesoscale, which is shown by the EM studies.[115]

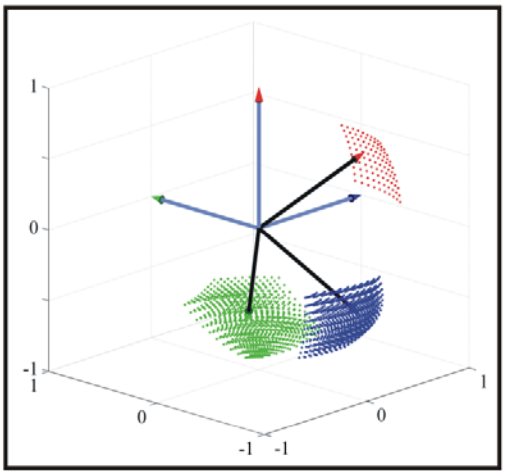

Figure 4.5.1 Physical model of the mutual orientation of the two remote ^{14}N shf PAS in [Cu^{2+}-Ac-Aβ(13-21)H14A], derived from the powder ^{14}N ESEEM. The hatched surface represents the simultaneous confidence interval at the 99% level of confidence. Axis color code: *x* (blue), *y* (green), *z* (red)

4.6 Structuring of Ac-Aβ(13-21)H14A Fibrils by Cu(II)

Figure 4.6.1 depicts the general features of our preliminary model for the coordination of Cu(II) in fibrils of Ac-Aβ(13-21)H14A, which was presented earlier.[38] The ESEEM results show equatorial bis-imidazole coordination, which indicates that the ligands are provided by the His14 side chains of two separate peptides. The His14 residue is present at the acetylated N-terminus of the peptide, and therefore, Cu(II) binds in the N-terminal region.

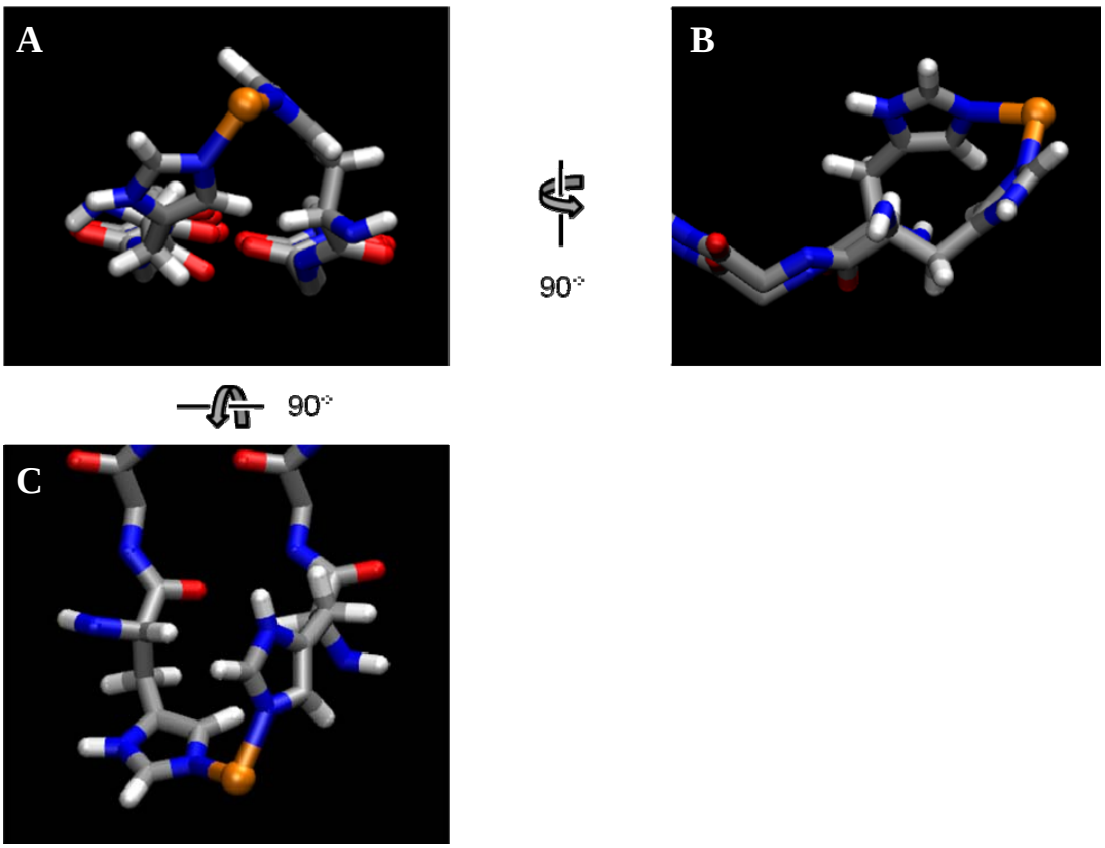

Figure 4.6.1 Three dimensional model portraying the Cu(II) binding to Aβ(13-21)H14A peptides in the fibril. Potential Cu(II)-binding site, between two β-strands within a sheet, perpendicular to the axis of fibril propagationAβ(13-21)H14A. **A.** View directed of two β-strands. **B.** View of two β-strands Cu(II)-Aβ(13-21)H14A rotated by 90° of the hydrogen bonding of the two β-strands. **C**.View of two β-strands Cu(II)-Aβ(13-21)H14A rotated by 90°along the fibril. Orange, Cu(II); Red, oxygen; blue, nitrogen, white, hydrogen.

Figure 4.6.1 shows a model for the Cu(II) coordination in the Ac-Aβ(13-21)H14A β-sheets, which is based on the analysis of the Cu(II)-H14 remote ^{14}N ESEEM double quantum harmonic component. The mutual orientation of the two imidazole rings is specified by the physical model (Figure 4.5.1), and the superhyperfine principal axis system-molecular principal axis system correspondence.[134-135] The angle between the proximal ^{14}N-Cu(II) bonds is assumed to be 93°, which corresponds to the confidence region center for the bis-*cis* coordination mode. The distance between the proximal

(directly coordinated) imidazole ^{14}N and Cu(II) is assumed to be 2.0 Å, which is characteristic of the ^{14}N-metal distance in Cu(II)-imidazole complexes, including the bis-*trans*- (2.03 Å) and bis-cis (1.97, 1.98 Å) imidazole complexes[137-138] used in the ESEEM studies. Thus, the N-Cu(II)-N triad forms a right isosceles triangle, with a hypotenuse of 2.8 Å. As shown in Figure 4.6.1 this unit is accommodated well in the context of the 5 Å intra-strand distance. Figure 4.6.1 shows that the bis-*cis*-imidazole coordination mode (relative to bis-*trans*) is obligatory for Cu(II) binding. Therefore, the presence of the bis-*cis*-imidazole coordination mode supports the model (Figure 4.6.1) of intra-sheet coordination of Cu(II). The structurally favourable and singular mode of alternating Cu(II) interactions with Ac-Aβ(13-21)H14A along the β-sheet N-terminal edge provides a partial rationale for the acceleration of Ac-Aβ(13-21)H14A fibrillization by Cu(II).

Figure 4.6.1 also shows that the Cu(II) binding introduces an asymmetry in the β-sheet, which is not present in the demetallated β-sheet. In order to coordinate the Cu(II), the two His14 side chains are recruited toward the Cu(II). This creates an alternating "vacancy" region along adjacent strands at the edge of the fibril, where Cu(II) binding is strongly disfavoured. This is the molecular origin of the Cu(II):peptide stoichiometry of approximately 0.5 in copper loaded fibrils of Ac-Aβ(13-21)H14A. This asymmetry may be an important feature in sheet assembly, sheet-sheet interactions en route to fibrils, or in higher order fibril structuring.

Chapter 5: Orientation selection ESEEM of Cu(II) model complexes

Continuous-wave (CW) EPR has been used extensively as a tool to determine the coordination geometry of Cu(II) in a number of proteins and model complexes.[70,139] When anisotropic interactions govern the EPR spectrum, orientation selection ESEEM can be used to provide additional information about the metal coordination environment. As introduced in Chapter 2, orientation selection ESEEM allows for the determination of the orientation of the principal axes of the quadrupole coupling tensor relative to the principal axes of the superhyperfine tensor for the remote ^{14}N, which governs the dispersion of the EPR spectrum in an orientationally disordered sample (i.e. powder sample).[140] The determination of the orientation of the quadrupole coupling tensor relative to the principal axes of Cu(II) can provide a means to ascertain the orientation of a ligand or functional group which contains the quadrupolar nucleus.[88] The superhyperfine tensor principal axis system, as depicted in Figure 5.1.1, along with the orientation of the tensor axis relative to g_z-tensor determines the geometry of the imidazole plane with respect to the g_z-tensor of Cu(II).[93]

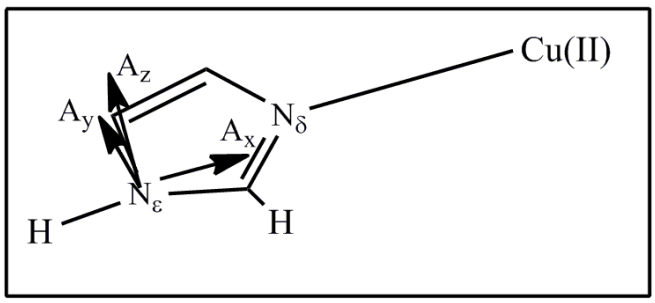

Figure 5.1.1 Depiction of the orientation of the remote ^{14}N superhyperfine coupling tensor with respect to the imidazole and Cu(II) geometries according to Colaneri et al.[93] The anisotropic components of the tensor, [*A, 0 , -A*], correspond to *A* to A_x, which is 13° off the direction of the N_δ-N_ε. The A_z corresponds to - *A*, and it is located 8° off the normal of the imidazole plane.

Several studies performed on Cu(II) using ESEEM spectroscopy have shown that the remote nitrogen of the imidazole ligand exhibits strong ESEEM modulations.[81,83,88,140-141] The double quantum, ν_{dq}, feature is strongly affected by changes in the nuclear quadrupole coupling and the superhyperfine tensor orientation with respect to the magnetic field.[89] The line shape and the position of the ν_{dq} feature can provide useful information about the coordination structure in the imidazole-type ligand coordination compounds. Additionally, the line shape of the double quantum harmonic, $2\nu_{dq}$, is dependent on the molecular structure of the molecule (see Chapters 2 and 4 for further details). Moreover, the $2\nu_{dq}$ feature is orientation selection dependent, so the orientation of the imidazole plane with respect to the Cu(II) can be determined.

Orientation selection was performed on three Cu(II) model complexes, (Cu(II)(Dien)(2-MeIm), Cu(II)$(Him)_2(NO_3)_2$, and Cu(II)$(2\text{-}MeIm)_2(OAc)_2$, and then applied to the Cu(II)-Aβ truncated/mutated complexes, Cu(II)-Aβ(13-21)K16A and Cu(II)/Ac- Aβ(13-21)H14A. The orientation of the imidazole ligands with respect to the Cu(II) *g*-principal axis system, was determined by the shift of the ν_{dq} as the magnetic field was varied. The results obtained from ESEEM were in accordance with the X-ray crystallographic structure for the Cu(II) complexes. These results were then compared to the Cu(II)-Aβ samples, in order to determine the orientation of the imidazole planes with respect to the *g*-tensor principal axis system.

For the bis-imidazole complexes (Cu(II)$(Him)_2(NO_3)_2$, and Cu(II)$(2\text{-}MeIm)_2(OAc)_2$), orientation selection was also applied to the $2\nu_{dq}$ feature. In Chapter 4, the $2\nu_{dq}$ line shape analysis provided information about the orientation of the two

imidazoles with respect to each other. In this chapter, the orientation of the imidazole plane with respect to the g-tensor will complement the determination of the molecular geometry of the Cu(II) model complexes. These results will then be expanded to the Cu(II)-Aβ(13-21) complexes to lead towards a greater understanding of the molecular coordination.

5.1 Orientation selection of ν_{dq} feature in Cu(II) model complexes

Orientation selection was performed on the Cu(II) model complexes through a series of ESEEM experiments that were performed at different central fields, ranging from 2580 Gauss to 3160 Gauss, by increments of approximately 130 Gauss. All other experimental parameters were unchanged. The simulated parameters are shown in Table 5.1.1

Table 5.1.1 ESEEM simulation parameters for the Cu(II)-imidazole model complexes, using orientation selection with $sin\theta d\theta$ weighting factor for $\tau = 234$ ns.

	single imidazole $Cu(II)(Dien)(2\text{-}MeIm)$	Bis-*trans* imidazole $Cu(II)(Him)_2(NO_3)_2$	Bis-*cis* imidazole $Cu(II)(2\text{-}MeIm)_2(OAc)_2$
A_{xx} (MHz)	2.15	2.09	2.39
A_{yy} (MHz)	1.95	1.64	2.01
A_{zz} (MHz)	1.60	1.40	1.31
A_{iso} (MHZ)	1.90	1.71	1.91
$A_{dip,x}$ (MHz)	0.25	0.38	0.48
$A_{dip,y}$ (MHz)	0.05	0.07	0.10
$A_{dip,z}$ (MHz)	-0.30	-0.24	-0.60
e^2qQ/h (MHz)	1.737	1.466	1.625
η	0.615	0.834	0.722
$\alpha_Q(°)$	23	293	325
$\beta_Q(°)$	138	320	205
$\gamma_Q(°)$	192	115	356
$\alpha_{A1}(°)$	215	51	0
$\beta_{A1}(°)$	216	344	44
$\gamma_{A1}(°)$	82	239	110
$\alpha_{A2}(°)$		263	99
$\beta_{A2}(°)$		291	6
$\gamma_A(°)$		61	0

5.1.1 Single Imidazole: Cu(II)(Dien)(2-MeIm)

For the single Cu(II)-imidazole complex, Figure 5.1.1.1, the Fourier Transform of the ESEEM spectrum was examined for each magnetic field. The ESEEM line shape of the Cu(II)(Dien)(2-MeIm) is characteristic of the $S = 1/2$ Cu(II) electron spin coupling with the $I = 1$ ^{14}N nucleus at exact cancellation of the hyperfine and Zeeman magnetic fields of the nucleus.[83]

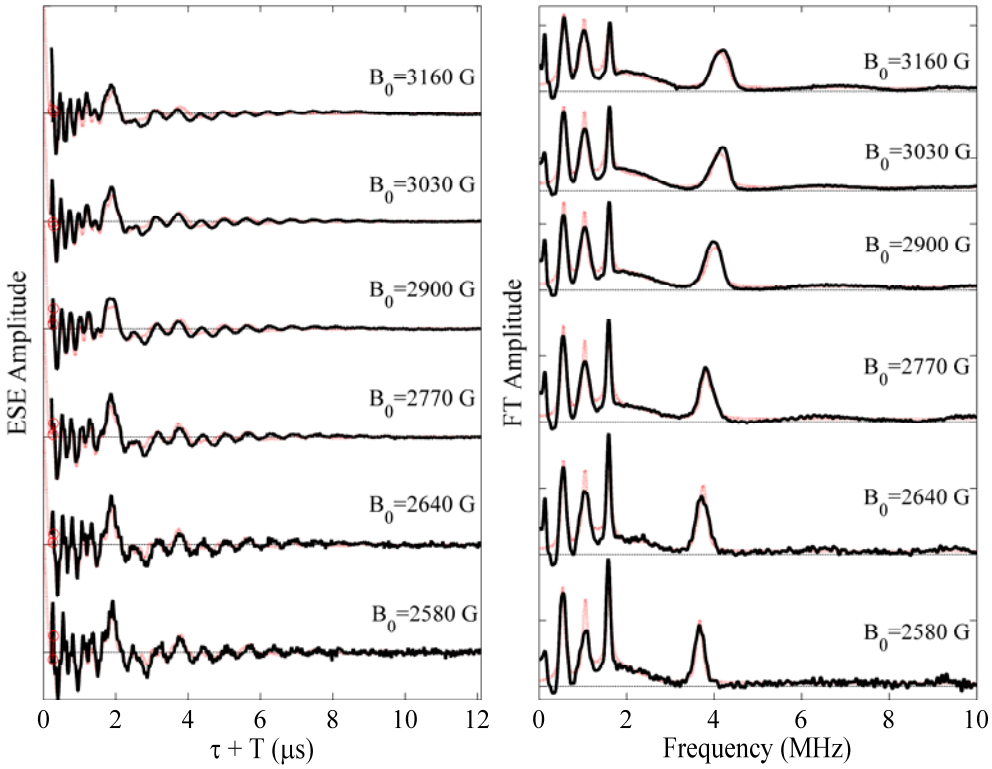

Figure 5.1.1.1 Orientation selection in three-pulse ESEEM experiment (left panel) and Fourier transform (right panel) for single imidazole [Cu(II)(Dien)(2-MeIm)], and overlaid simulation (red dashed curve). Simulation parameters are presented in Table 5.1.1. *Experimental conditions:* sample temperature, 6 K; microwave frequency, 8.772 GHz; initial τ value -114 ns; τ increment, 20 ns; $\pi/2$ pulse width, 20 ns; pulse repetition rate, 120 Hz; 32 pulses per repetition. One accumulation: 3160, 3030 Gauss; 2 accumulations: 2900, 2770, 2580 Gauss; 3 accumulations: 2640 Gauss.

As previously mentioned in Chapters 2, and 4, the three narrow lines at low frequency correspond to the ν_0, ν_-, and ν_+ nuclear quadrupole frequencies. The broad line near 4 MHz represents the $\Delta m_I = \pm 2$ energy level splitting in the electron spin manifold where the hyperfine and Zeeman magnetic fields add to produce a finite field. When the magnetic field is varied from 2580 Gauss to 3160 Gauss, three significant differences are observed as the magnetic field is increased: (1) the amplitude of the quadrupole features becomes relatively equal in magnitude, (2) the broad feature corresponding to the double quantum feature, ν_{dq}, around 4 MHz is broadened, and (3) the maximum of the ν_{dq} feature shifts to higher frequency from 2580 to 3030 Gauss, and then shifts to lower frequency at 3160 Gauss. The differences, in the ν_{dq} feature are more clearly shown in Figure 5.1.1.2 in which the ESEEM spectra were corrected for the nuclear Zeeman effect.

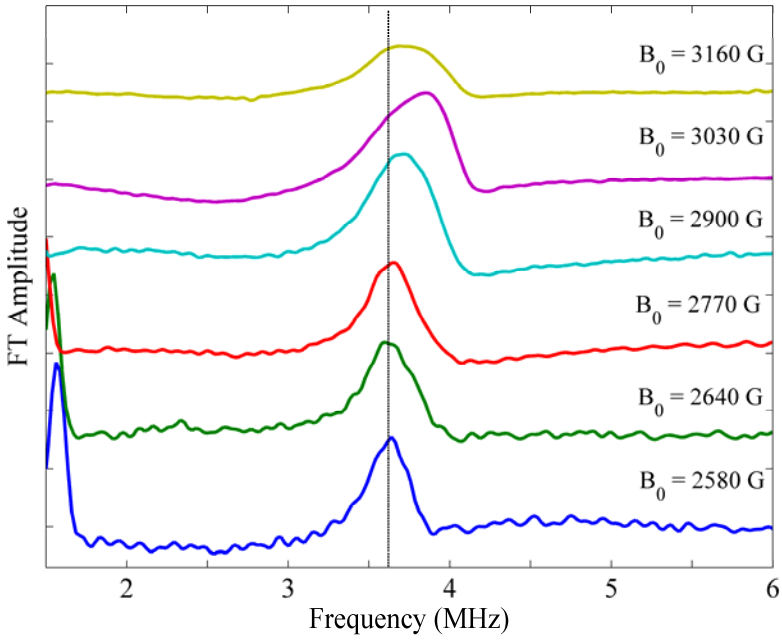

Figure 5.1.1.2 Orientation selection in three-pulse ESEEM experiment. Fourier transform for single imidazole [Cu(II)(Dien)(2-MeIm)], focus on the double quantum feature, ν_{dq}. The ν_{dq} shows magnetic field dependence after the nuclear Zeeman influence correction. *Experimental conditions* are the same as in Figure 5.1.1.1

The nuclear Zeeman term of the Hamiltonian (equation 2.2.3.1) shows that the magnetic field interacts with the nuclear spin term, thus ν_{dq} is dependent on the magnetic field. To properly analyze the data, the influence of the nuclear Zeeman term needs to subtracted from the hyperfine term at each magnetic field ($\nu_{^{14}N}$ = 3.075 MHz at B_0 = 10 KGauss). After correcting for this influence, any remaining dependence of the double quantum line shape on the magnetic field arises purely from the dipolar hyperfine anisotropy. The position of the nuclear quadrupole frequencies do not change significantly, because these features arise from the interaction of the ^{14}N nucleus with the surrounding electric field gradient, and are therefore independent of the magnetic field. The changes in the ν_{dq} feature that are mentioned above, show the principal orientation selection dependence of the system.

5.1.2 Bis-trans imidazole: Cu(II)(Him)$_2$(NO$_3$)$_2$

The line shape of the 3-pulse ESEEM spectra for the bis-*trans* imidazole complex, Cu(II)(Him)$_2$(NO$_3$)$_2$ (Figure 5.1.2.1), shows some spectral characteristics, that are similar to that of the single Cu(II)-imidazole complex. As seen in Chapter 4, the sharp features on the lower frequency range correspond to the nuclear quadrupole interactions, ν_0, ν_-, and ν_+. For this complex the linewidths of the ν_0 and ν_- features are broad and overlap, so they appear as a single feature. The line shape of the ν_{dq} feature shows orientation dependence on the magnetic field (Figures 5.1.2.1-2). As the magnetic field increases the ν_{dq} is slightly broadened, the amplitude increases relative to the amplitudes of the nuclear quadrupole interaction features, and the position of the

maximum of the ν_{dq} feature shifts to higher frequency, as shown in the nuclear Zeeman-corrected plot in Figure 5.1.2.2. The bis-*trans* imidazole displays a more noticeable shift of the ν_{dq} feature to higher frequency at increasing magnetic field, relative to the single-imidazole.

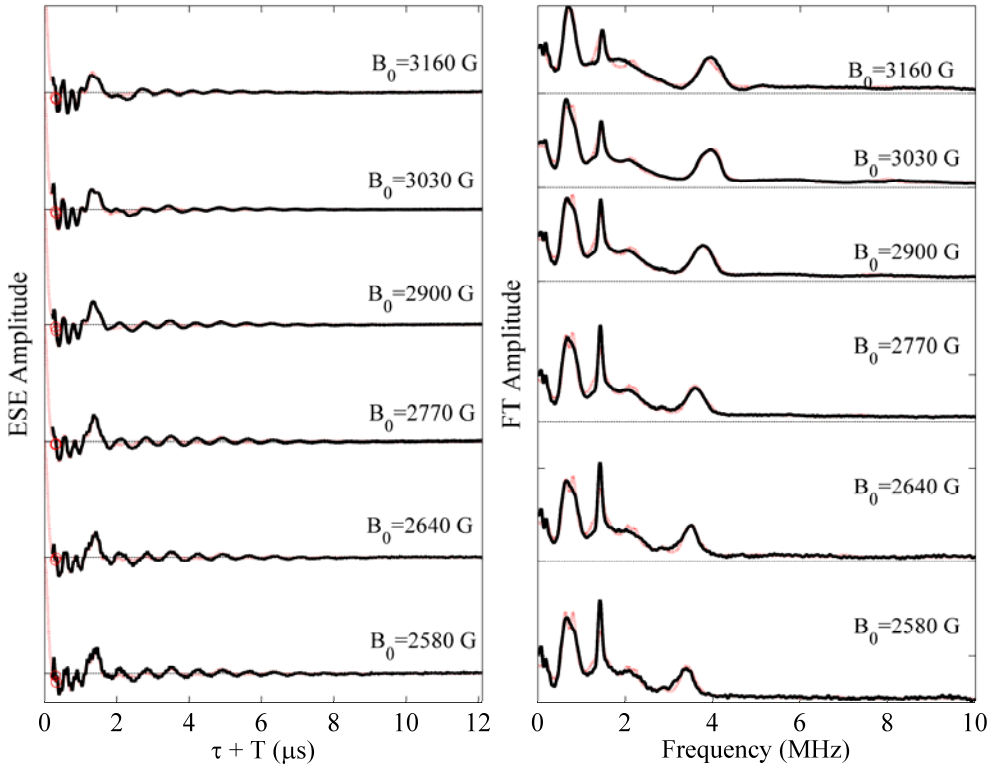

Figure 5.1.2.1 Orientation selection in three-pulse ESEEM experiment (left panel) and Fourier transform (right panel) for bis-*trans* imidazole [Cu(II)$(Him)_2(NO_3)_2$], and overlaid simulation (red dashed curve). Simulation parameters are presented in Table 5.1.1. *Experimental conditions:* sample temperature, 6 K; microwave frequency, 8.772 GHz; initial τ value -114 ns; τ increment, 20 ns; $\pi/2$ pulse width, 20 ns; pulse repetition rate, 120 Hz; 32 pulses per repetition. One accumulation: 3160, 3030, 2900 Gauss; 2 accumulations: 2770, Gauss; 4 accumulations: 2640, 2580 Gauss.

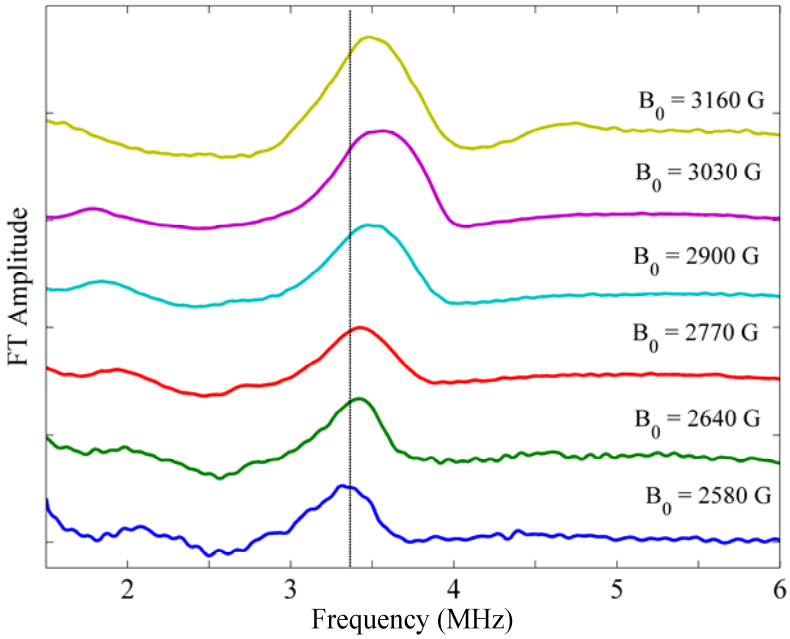

Figure 5.1.2.2 Orientation selection in three-pulse ESEEM experiment. Fourier transform for the bis-*trans* imidazole [Cu(II)$(Him)_2(NO_3)_2$], focus on the double quantum feature, ν_{dq}. The ν_{dq} shows magnetic field dependence after the nuclear Zeeman influence correction. *Experimental conditions* are the same as in Figure 5.1.2.1

5.1.3 Bis-cis imidazole: Cu(II)$(2\text{-MeIm})_2(OAc)_2$

Variations in the line shape of the 3-pulse ESEEM spectra for the bis-*cis* imidazole at the different magnetic field values are shown in Figure 5.1.3.1. As for the single-imidazole and the bis-*trans* complexes, the variations in the amplitude and positions of the nuclear quadrupole frequencies are minor, but there are significant changes in the line shape and relative position of ν_{dq} feature. The nuclear quadrupole frequencies, ν_0, ν_-, and ν_+ are all resolved, and additional features are observed in the FT ESEEM spectrum (between the nuclear quadrupole frequencies and the ν_{dq} frequencies). These small features correspond to the harmonic lines, which come from the interaction of the Cu(II) with two or more nuclei, as discussed in Chapters 2, and 4. An additional

harmonic line is observed around 8 MHz at 3030 Gauss, which corresponds to the double quantum harmonic, $2\nu_{dq.}$

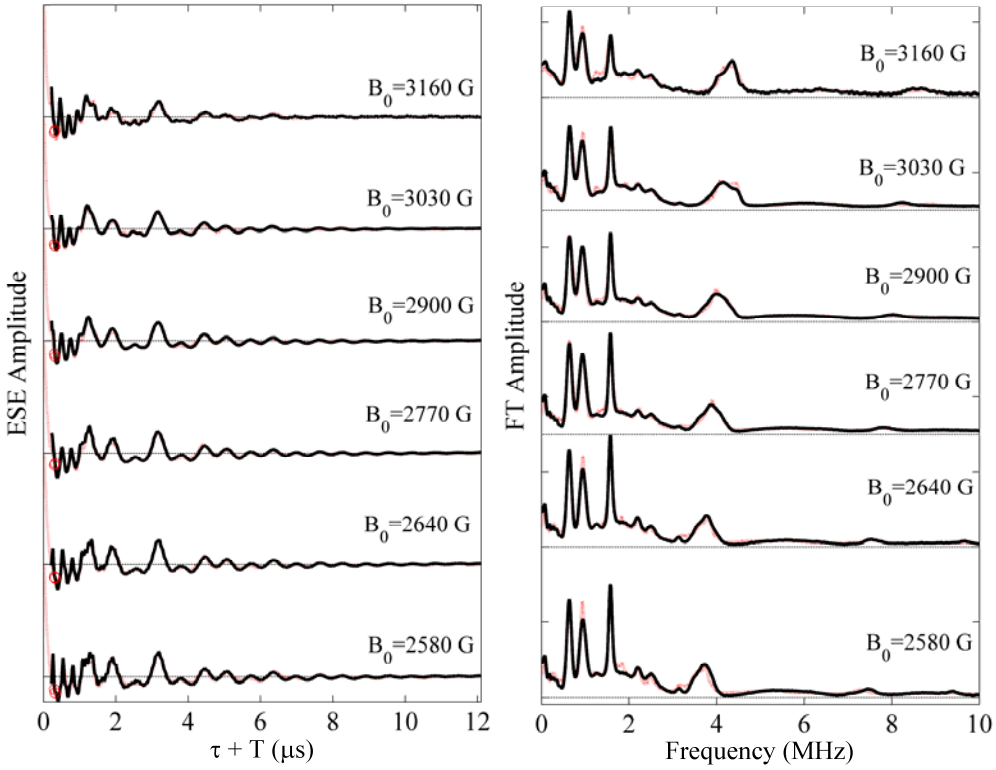

Figure 5.1.3.1 Orientation selection in three-pulse ESEEM experiment (left panel) and Fourier transform (right panel) for bis-*cis* imidazole [Cu(II)(2-MeIm)$_2$(OAc)$_2$], and overlaid simulation (red dashed curve). Simulation parameters are presented in Table 5.1.1. *Experimental conditions:* sample temperature, 6 K; microwave frequency, 8.772 GHz; initial τ value -114 ns; τ increment, 20 ns; $\pi/2$ pulse width, 20 ns; pulse repetition rate, 120 Hz; 64 pulses per repetition. 6 accumulations: 3160 Gauss; one accumulation 3030, 2900, 2770, 2640 Gauss;

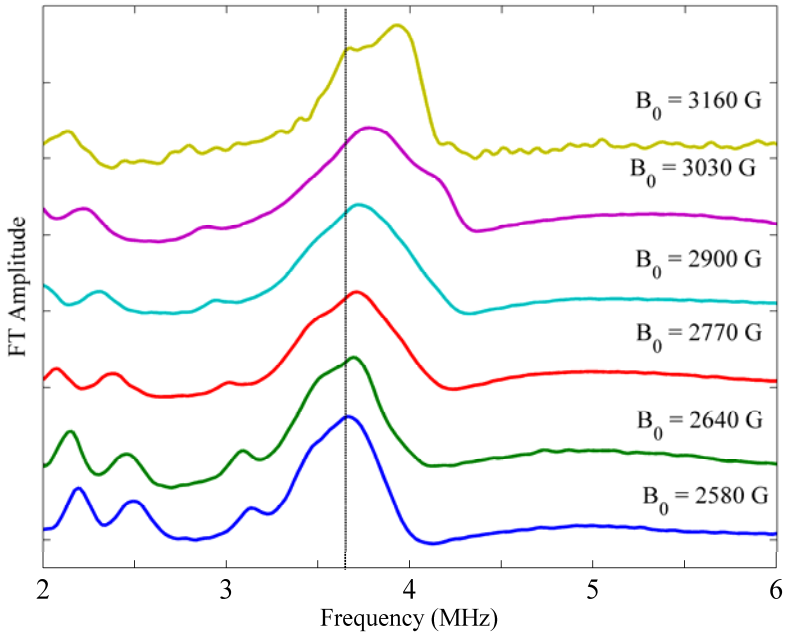

Figure 5.1.3.2 Orientation selection in three-pulse ESEEM experiment. Fourier transform for the bis-*cis* imidazole [Cu(II)(2-MeIm)$_2$(OAc)$_2$], focus on the double quantum feature, ν_{dq}. The ν_{dq} shows magnetic field dependence after the nuclear Zeeman influence correction. *Experimental conditions* are the same as in Figure 5.1.3.1

5.1.4 Qualitative Interpretation of the orientation dependence of the ν_{dq} feature

The orientation selection dependence for the Cu(II) model complexes is shown with the magnetic dependence of the ν_{dq} in Figures 5.1.1.1-5.1.3.2. The ν_{dq} feature shows changes in both line shape and position, as is expected for orientation selection dependence, because the magnetic field is set at different resonance position in the EPR spectrum. The general dependence of nuclear Zeeman corrected position and the line shape is comparable for all three Cu(II) model complexes. At 3030 Gauss, the ν_{dq} feature

has the approximate line shape of a powder average ν_{dq} feature (as described in Chapter 2), but it is narrower and skewed towards higher frequency. As the magnetic field is decreased from 3030 Gauss to 2580 Gauss, the line shape and maximum of the ν_{dq} feature is skewed to the lower frequency edge of the powder distribution. At 3160 Gauss, the line shape position displays a smaller shift to lower frequency (Figures 5.1.1.1-5.1.3.2).

Theoretical studies of copper histidine complexes have shown that the isotropic superhyperfine term, A_{iso} is positive.[142] The anisotropic superhyperfine tensor component for a Cu(II)-histidine single crystal has the approximate form of $[A, 0, -A]_{dip}$ (MHz).[92] As mentioned in previous chapters, the axis of the smallest component, - A, corresponds to the direction of 8° from the imidazole ring normal, and the largest component, A, lies approximately in the imidazole plane and is directed approximately along the directly coordinated ^{14}N, as depicted in Figure 5.1.1. The simulations of the complexes give the intrinsic superhyperfine tensor components: A_{xx}, A_{yy}, and A_{zz}. From these values, the isotropic A_{iso} and dipolar terms can be calculated, and are shown in Table 5.1.1. The calculated tensor forms agree with the results of the Cu(II) single crystal studies.[66,92-93]

The changes in the ν_{dq} line shape and position can be interpreted by the weighting factors that are explained in Chapter 2. For the bis-*trans* model complex, the probability of the different orientations, at the different magnetic fields is shown in Figure 5.1.4.1. These distributions are characteristic for all the Cu(II) model complexes. As the magnetic field is increased, a larger population of the electron spins is covered. From the results of the single crystal ESEEM experiments,[66,92-93] the z-axis of the ^{14}N nucleus is

normal to the plane of the imidazole, thus as the magnetic field is increased, the mean angle formed between the *z*-axis of the ^{14}N and the g-tensor of the Cu(II) approaches 90°.

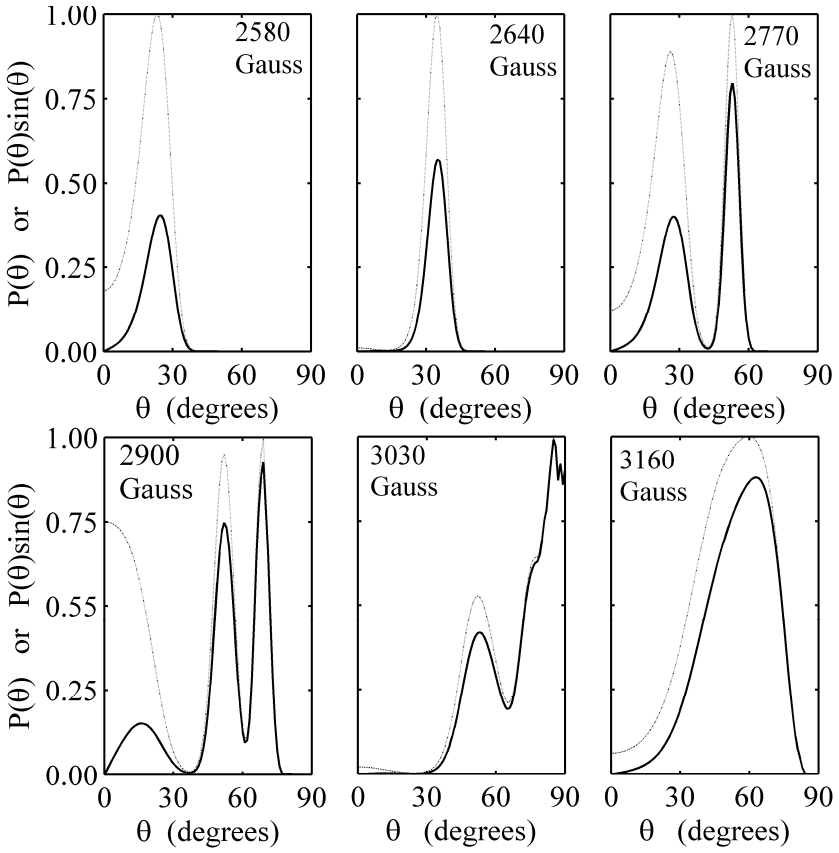

Figure 5.1.4.1 For single bis-*trans* imidazole $[Cu(II)(Him)_2(NO_3)_2]$, orientation of the magnetic field with respect to the principal axis of the *g*-tensor at six different magnetic fields, (2580, 2640, 2770, 2900, 3030 and 3160 G). The "powder position" corresponds to 3030 G, where all the spins orientations are excited by covering all the angles. The dotted curve shows an experimental EPR absorption line. The solid line corresponds to the experimental EPR absorption line multiplied by $sin\theta$ (corresponding to the angle weighting effect).

The angle of the magnetic field with respect to the superhyperfine tensor of the remote nitrogen can be inferred from the line shape of the double quantum feature. In Chapter 2, the intensity of absorption of observed transitions can be decided by the orientation of the

angle, θ. According to the dipole-dipole approximation, at low magnetic field where $\theta \approx$ 0°, the ν_{dq} feature will be resolved at higher frequency, and as the magnetic field increases, the ν_{dq} feature will migrate towards a lower frequency, as depicted in Figure 2.2.3.2C for the m_s = - 1/2 spin manifold. However, for the Cu(II)-imidazole complexes, the double quantum ν_{dq} feature shift to a lower frequency as the magnetic field is decreased. The reason for the opposite shift of the ν_{dq} feature is that the superhyperfine tensor is in the form [A 0 –A] instead of the dipole-dipole tensor form [- A - A +2A]. Therefore, the direction of the A_{zz}-axis of the dipole-dipole tensor is towards the directly coordinated ^{14}N, whereas for the single-crystal superhyperfine tensor, the A_{zz}-axis is 8° off the normal of the imidazole plane.

Considering the ideal case, where the imidazole planes are coplanar to the Cu(II) plane, at low magnetic field (2580 Gauss) only few electron spins are selected since θ is approximately 0°. Therefore, the superhyperfine A_{zz}-axis is considered to be parallel to the g_z-axis. When the magnetic field is increased, the ν_{dq} feature should shift to a higher frequency. This shift is observed for the bis-*trans* complex (Figure 5.1.2.2). This indicates that the imidazole plane is approximately coplanar to the equatorial plane of the Cu(II). Rotation of the imidazole planes are due to the 8° angle that A_{zz}-axis has off the normal to the imidazole plane. Furthermore, the amplitude of the ν_{dq} broadens as the magnetic field is increased. As seen in Figure 5.1.4.1, the population of electron spins covered increases as the magnetic field increases. At 3030 Gauss nearly all of the orientations of the electron spins are covered, which translates to a broader ν_{dq} feature. These results are consistent with the X-ray crystallographic structure for the bis-*trans*

Cu(II) complex (Figure 3.1.1b), which shows that the imidazole plane of the bis-*trans* is rotated approximately 20° out of the equatorial plane of the Cu(II).

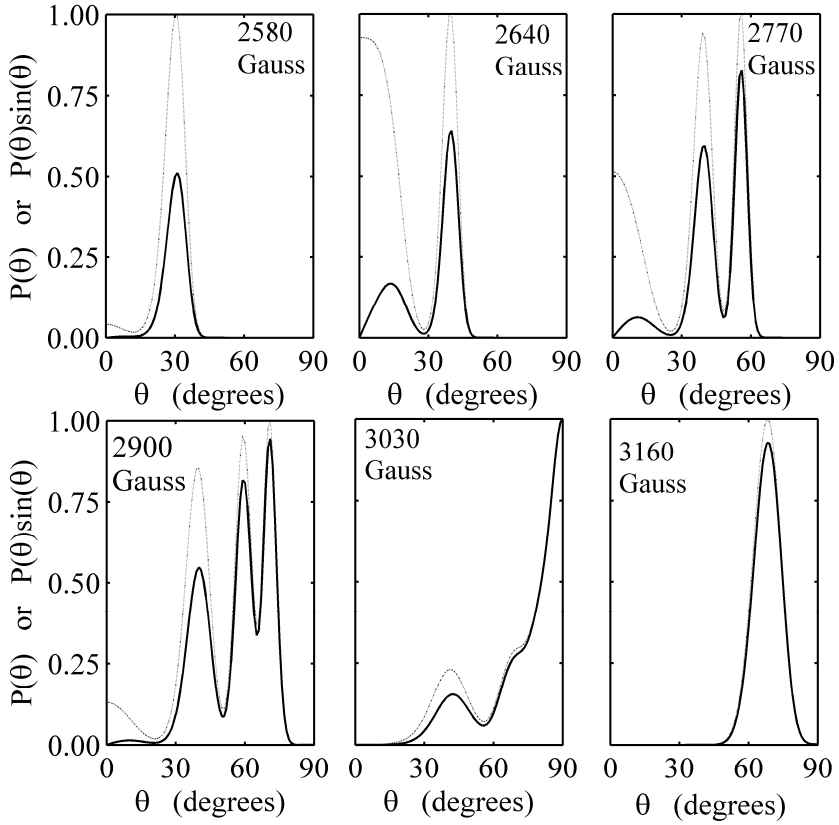

Figure 5.1.4.2 For single bis-*cis* imidazole [Cu(II)(2-MeIm)$_2$(OAc)$_2$], orientation of the magnetic field with respect to the principal axis of the *g*-tensor at six different magnetic fields, (2580, 2640, 2770, 2900, 3030 and 3160 G). The "powder position" corresponds to 3030 G, where all the spins orientations are excited by covering all the angles. The dotted curve shows an experimental EPR absorption line. The solid line corresponds to the experimental EPR absorption line multiplied by $sin\theta$ (corresponding to the angle weighting effect).

For the case of the bis-*cis* complex, both imidazole planes are separated from each other by 90° (i.e the imidazole coordinated ^{14}N ligand to the Cu(II) is 90° from the other ^{14}N coordinated ligand), and are rotated roughly 45° out of the equatorial plane of the

Cu(II). However, one imidazole is rotated 45° clockwise with respect to the immediately coordinated ^{14}N nucleus and the other is rotated counterclockwise. The magnetic field is at a 45° angle with the superhyperfine A_{zz}-axis (the axis 8° off the normal of the imidazole ring plane) at 2580 Gauss, when it is nearly parallel with the g_z axis. At 3030 Gauss, the magnetic field is also at 45° relative to the superhyperfine *z*-axis. The line shape of the ν_{dq} feature is centered at the frequency that corresponds to the 45° angle of θ. Therefore, as the magnetic field increases the position of the ν_{dq} feature remains the same, but the line shape has a shoulder at 3030 Gauss, as shown in Figure 5.1.4.2. This suggests that superhyperfine A_{zz}-axis of one of the imidazole is 225° off the g_z-axis of the Cu(II). At 3160 Gauss, the line shape of ν_{dq} feature has a higher amplitude at higher frequency, opposite to the line shape at powder position (3030 Gauss). This is expected based on the orientation of imidazole planes (45° of the equatorial plane of the Cu(II) and rotated 90° with respect to each other) as determined from X-ray crystallographic structure (Figure 3.1.1c).

The behavior for the ν_{dq} feature of the single imidazole is similar to the bis-*cis* samples. As the magnetic field is increased, the ν_{dq} feature does not shift until 2900 Gauss, as shown in Figure 5.1.2-3. The reason that the ν_{dq} does not shift in frequency at lower magnetic fields is because the ν_{dq} feature is centered at 45° from the magnetic field. From the population weighting plots (Figure 5.1.4.3), the low magnetic fields (i.e. 2580, 2640 and 2770 Gauss) cover similar angle orientations (approximately 30° angle). At 2770 the 60° angle is also included, which is shown in the broadness of the line shape of the ν_{dq} feature. At higher magnetic fields, a wider range of angles is covered. Therefore at higher magnetic fields, the ν_{dq} feature is shift towards higher frequencies,

and is broadened. In addition, the ν_{dq} feature shifts slightly to higher frequency, this indicates that the imidazole plane must be at approximately 45° angle from the equatorial plane of the Cu(II).

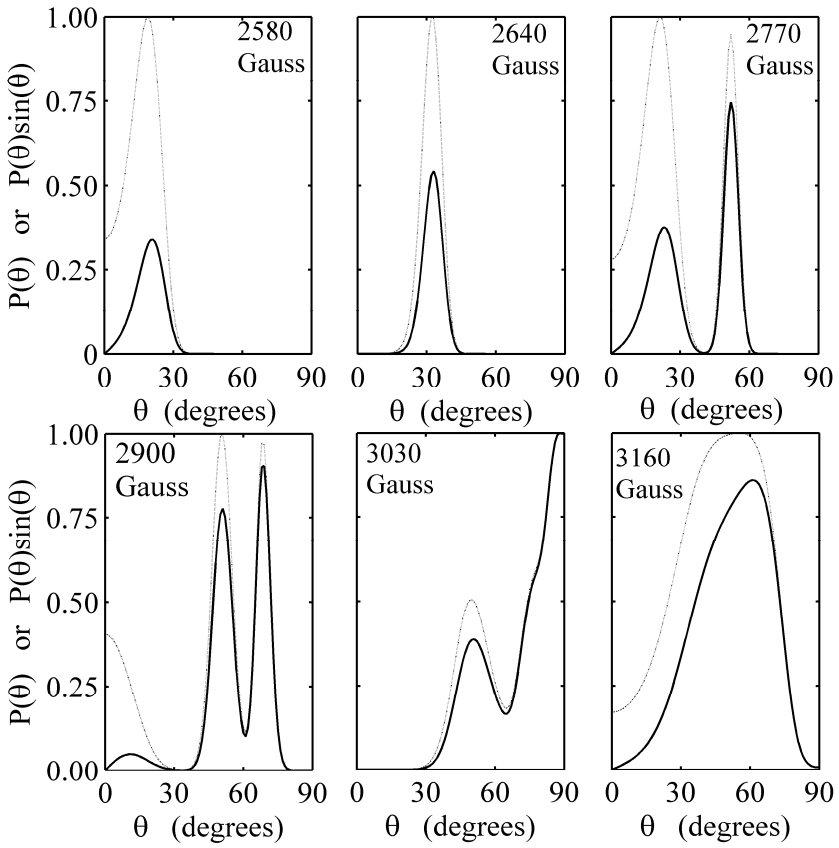

Figure 5.1.4.3 For single imidazole [Cu(II)(Dien)(2-MeIm)], orientation of the magnetic field with respect to the principal axis of the *g*-tensor at six different magnetic fields, (2580, 2640, 2770, 2900, 3030 and 3160 G). The "powder position" corresponds to 3030 G, where all the spins orientations are excited by covering all the angles. The dotted curve shows an experimental EPR absorption line. The solid line corresponds to the experimental EPR absorption line multiplied by $sin\theta$ (corresponding to the angle weighting effect).

5.2 Orientation selection of ν_{dq} feature in Cu(II)-Aβ complexes

5.2.1 Single Imidazole: Aβ(13-21)K16A

For the single imidazole complex, as shown above, the ESEEM Fourier transform is composed of the nuclear quadrupole frequencies, and the $\Delta m_I = \pm 2$ or ν_{dq} feature. The Aβ(13-21)K16A ESEEM spectrum (Figure 5.2.1.1) displays no harmonics, as is expected for a single imidazole complex. The line widths of the nuclear quadrupole frequencies, ν_0 and ν_-, are broadened, and appear as a single feature.

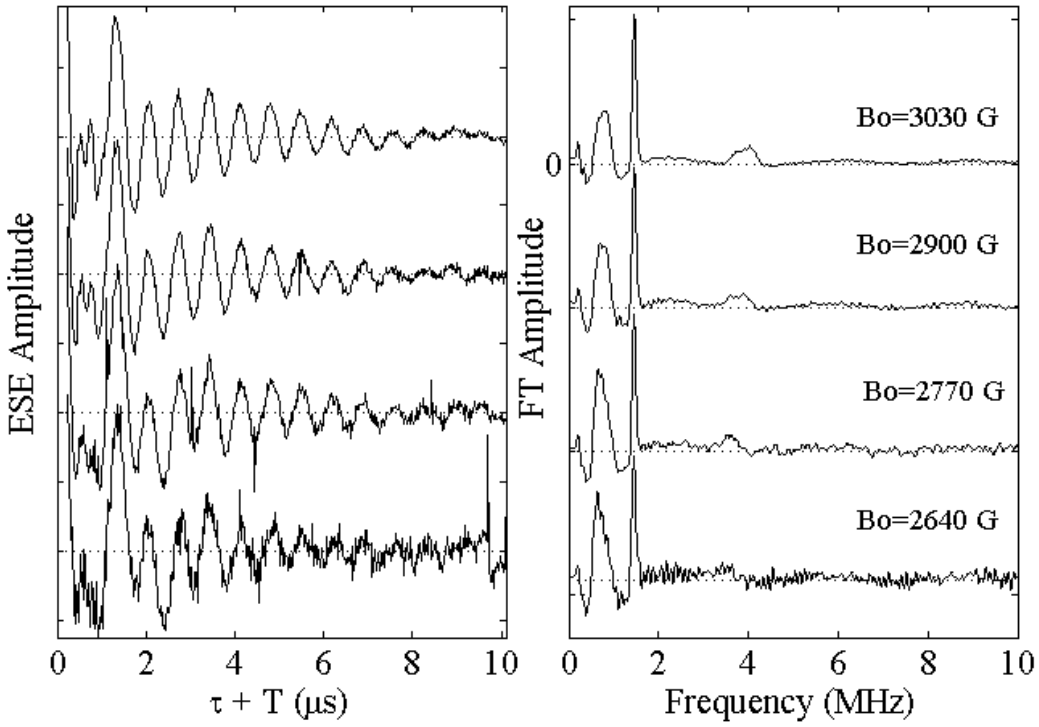

Figure 5.2.1.1 Orientation selection in three-pulse ESEEM experiment and Fourier transform for the Cu(II)-Aβ(13-21)K16A soluble complex. *Experimental conditions:* sample temperature, 6 K; microwave frequency, 8.772 GHz; initial τ value -36 ns; τ increment, 20 ns; π/2 pulse width, 20 ns; pulse repetition rate, 20 Hz; 20 pulses per repetition. One accumulation: 3030 Gauss; 5 accumulations: 2900 Gauss; 7 accumulations: 2770 Gauss; 12 accumulations: 2640 Gauss.

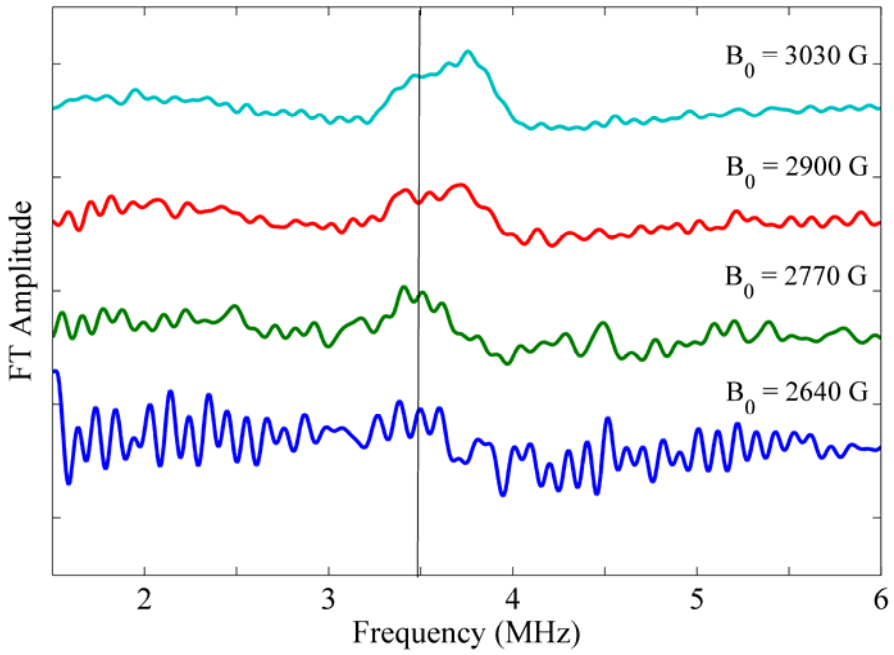

Figure 5.2.1.2 Orientation selection in three-pulse ESEEM experiment. Fourier transform for Cu(II)-Aβ(13-21)K16A soluble complex, focus on the double quantum feature, ν_{dq}. The ν_{dq} shows magnetic field dependence after the nuclear Zeeman influence correction. *Experimental conditions* are the same as in Figure 5.2.1.1

The ν_{dq} line of Aβ(13-21)K16A increases in amplitude, and shifts slightly to higher frequencies as the magnetic field is increased as shown in the nuclear Zeeman corrected Figure 5.2.1.2. As the magnetic field is varied from 2640 to 3030 Gauss the ν_{dq} feature increases in amplitude. At the lowest magnetic field (2640 Gauss), the ν_{dq} feature is difficult to resolve due to spectral noise. At a higher magnetic field (3030 Gauss), the ν_{dq} line shape is has a shoulder at higher frequency. The angle between the magnetic field and the superhyperfine tensor of the remote ^{14}N nuclei can be inferred from the shift of the ν_{dq} feature. If the plane of the imidazole is in the equatorial plane of the Cu(II), the displacement of the ν_{dq} feature would be towards a higher frequency, as the magnetic field value is increased. At lower magnetic fields, the angle of the magnetic fields with

the *z*-component of the superhyperfine tensor principal axis will approach to 0°, and the ν_{dq} feature will have much smaller amplitude. Therefore, the plane of the imidazole of Aβ(13-21)K16A is expected to be approximately in the equatorial plane of the Cu(II).

5.2.2 Bis-imidazole: Ac-Aβ(13-21)H14A

The ν_{dq} feature of the the bis-imidazole ligand Cu(II) sample, Ac-Aβ(13-21)H14A (Figures 5.2.2.1-2), shows orientation selection dependence on the magnetic field. The ESEEM Fourier transform spectrum shows the nuclear quadrupole frequencies, and the ν_{dq} feature. As wtih Aβ(13-21)K16A, the ν_0 and ν_- lines are broad, and appear as a single feature. In addition, the $\nu_0 + \nu_+$, $\nu_- + \nu_+$, and $2\nu_+$ harmonics, which are characteristic of two ^{14}N nuclei coupling to Cu(II), are resolved and seen at 2-3 MHz in the ESEEM spectra in Figure 5.2.2.1.

The ν_{dq} feature is dependent on the magnetic field, as the $\Delta m_I = \pm 2$ transition line shifts to higher frequency as the magnetic field increases (Figure 5.2.2.2). The $2\nu_{dq}$ line shape remains similar through the magnetic fields of 3030, 2900, 2770 and 2640 Gauss, and the position of the feature shows a smaller shift relative to the Cu(II) model complexes. This suggests that the imidazole plane is oriented at an angle of roughly 45° relative to the equatorial plane of the Cu(II). This phenomenon is similar to the bis-*cis* complex as explained previously. Therefore, the ν_{dq} feature would be centered at the frequency that corresponds to the 45° angle weighting at both 2640 Gauss and 3160 Gauss, and the ν_{dq} feature would be weighted more heavily towards the higher

frequencies at magnetic fields between the two extremes. A preliminary conclusion for the Cu(II)- Ac-Ab(13-21)H14A is that the imidazole ring plane's normal is oriented at an angle of 30-45° with respect to the g_z-axis, similar to the bis-*cis* complex.

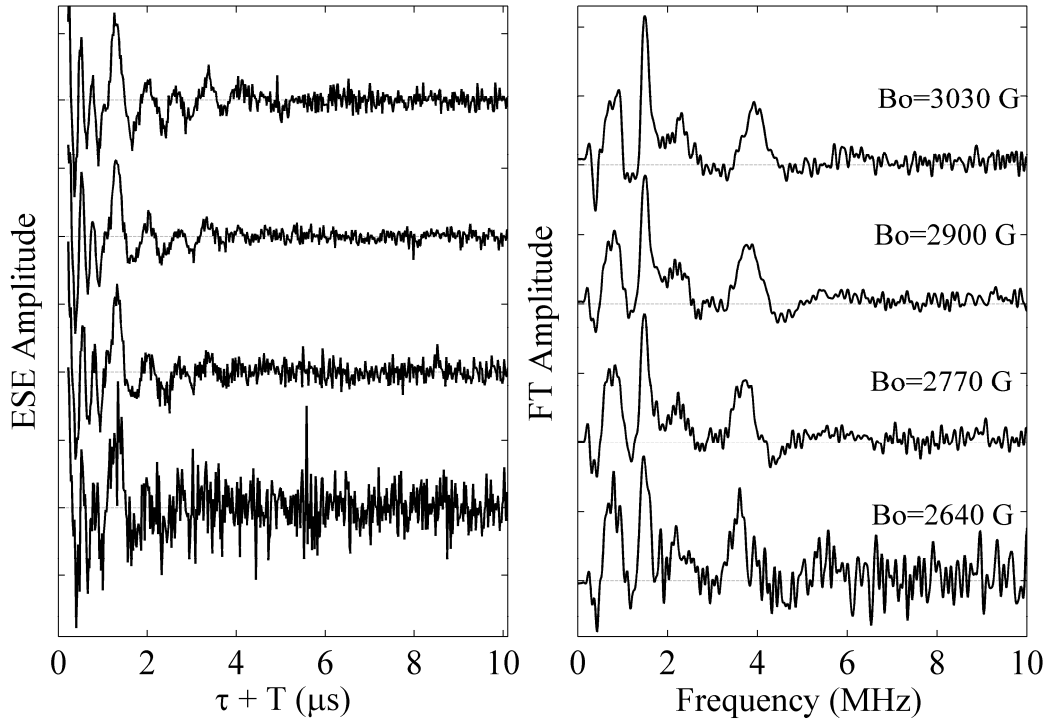

Figure 5.2.2.1 Orientation selection in three-pulse ESEEM experiment and Fourier transform for the Cu(II)-Ac-Aβ(13-21)H14A fibrillar complex. *Experimental conditions:* sample temperature, 6 K; microwave frequency, 8.772 GHz; initial τ value -36 ns; τ increment, 20 ns; π/2 pulse width, 20 ns; pulse repetition rate, 20 Hz; 20 pulses per repetition. One accumulation: 3030 Gauss; 7 accumulations: 2900, 2640 Gauss; 8 accumulations: 2770 Gauss.

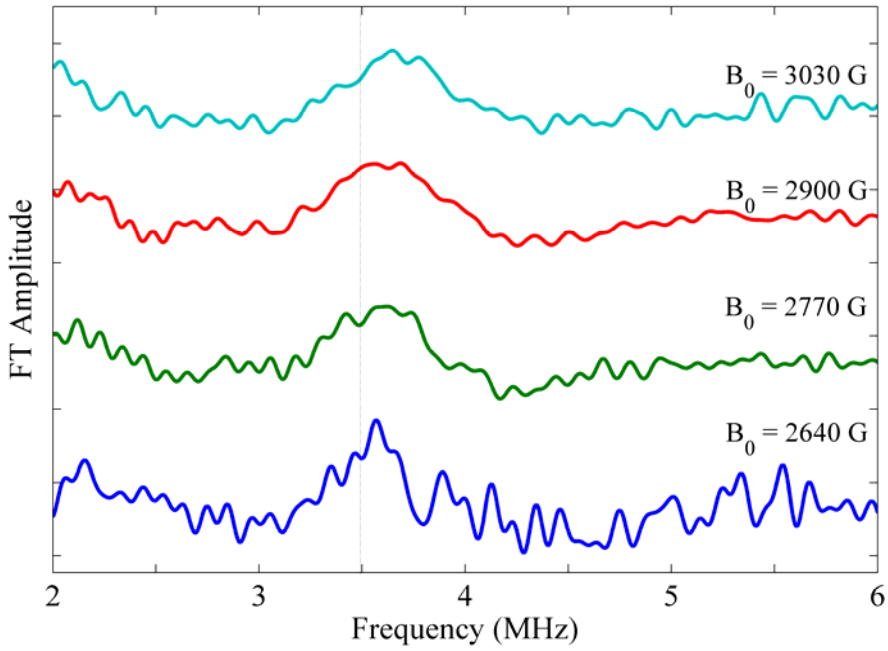

Figure 5.2.2.2 Orientation selection in three-pulse ESEEM experiment. Fourier transform for the Cu(II)-Ac-Aβ(13-21)H14A fibrillar complex, focus on the double quantum feature, ν_{dq}. The ν_{dq} shows magnetic field dependence after the nuclear Zeeman influence correction. *Experimental conditions* are the same as in Figure 5.2.2.1

5.3 Orientation selection of double quantum harmonic, $2\nu_{dq}$, feature in bis-imidazole Cu(II) models

The $\Delta m_I = \pm 2$ transition or double quantum line is orientation selection dependent, as shown in the preceding section. For Cu(II) bis-imidazole complexes, additional features are observed in the ESEEM spectra. These lines are commonly referred to as combination lines. As mentioned above and in chapters 2, and 4, the combination lines correspond to the nuclear quadrupole frequencies, $\nu_0 + \nu_+$, $\nu_- + \nu_+$, $2\nu_+$ and the double quantum frequency, $2\nu_{dq}$. These combination lines, commonly referred to

as harmonics,[81,143] display changes in amplitude depending on values of τ, (the time between the first and the second pulse). The τ values in the experiments are selected to suppress the undesired contribution of matrix (weakly coupled) protons to the spectra, and therefore correspond to integral multiples of the reciprocal of the free proton frequency ($\nu_N(^1H) = 12.9$ MHz at 3030 Gauss).[74,86] In the bis-imidazole complexes the double quantum harmonic ($2\nu_{dq}$) was best resolved by using $\tau = 310$ ns as can be seen in Figures 5.3.1 and 5.3.3. For the bis-*trans* complex, the harmonics (specially the $2\nu_{dq}$) are not well resolved at other τ-values, as observed in Figure 5.1.2.1. Harmonics for the bis-*cis* complex are resolved at other τ-values, but have maximal amplitude at $\tau = 310$ ns when compared to the lower τ-value ($\tau = 234$ ns).

The combination line for the $2\nu_{dq}$ feature is well resolved for both bis-imidazole complexes at $\tau = 310$ ns. Like the ν_{dq} feature, the $2\nu_{dq}$ harmonic is magnetic field dependent. As described in Chapters 4, the line shape of the $2\nu_{dq}$ feature allows for the specification of the equatorial coordination mode (*trans* or *cis*) and the relative orientation of the two imidazole rings.

Additionally, the position of the $2\nu_{dq}$ shows orientation selection (Figures 5.3.1-2). The position, amplitude and line shape provide information on the coordination of the complex. For the bis-*trans* complex, the line shape broadens from 3030 Gauss to 3160 Gauss, as shown in Figure 5.3.2. This broadening is expected because both superhyperfine *z*-axes are in the same direction. At a lower magnetic field, 2640 Gauss, the signal-to-noise is too poor to draw any conclusion with respect to the shift and the broadness of the $2\nu_{dq}$. The structure of the bis-*trans* complex has to be determined

through the analysis of the ν_{dq} feature, as explained previously, which is consistent with the X-ray crystallographic structure (Figure 3.1.1b).

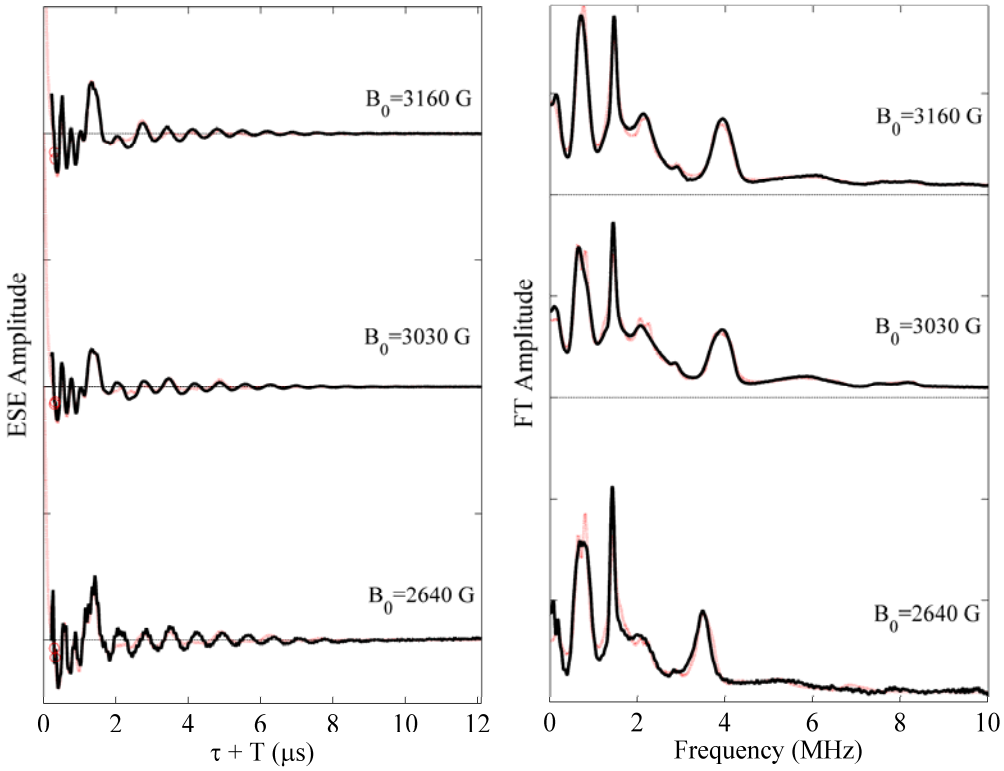

Figure 5.3.1 Orientation selection in three-pulse ESEEM experiment and Fourier transform for bis-*trans* imidazole [Cu(II)(Him)$_2$(NO$_3$)$_2$], and overlaid simulation (red dashed curve). Simulation parameters are presented in Table 5.3.1. *Experimental conditions:* sample temperature, 6 K; microwave frequency, 8.772 GHz; magnetic field strength, 3030 Gauss; τ = 310 ns; initial T value -190 ns; T increment, 20 ns; $\pi/2$ pulse width, 20 ns; pulse repetition rate, 120 Hz; 64 pulses per repetition. 2 accumulations: 3160 Gauss; one accumulation: 3030 Gauss; 3 accumulations: 2640 Gauss.

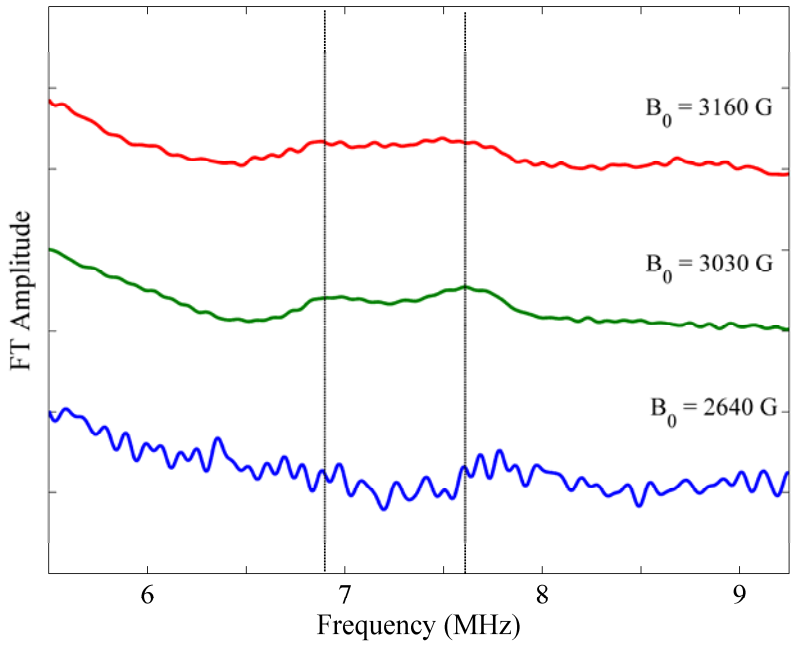

Figure 5.3.2 Orientation selection in three-pulse ESEEM experiment. Fourier transform for the bis-*trans* imidazole [Cu(II)(Him)$_2$(NO$_3$)$_2$], focus on the double quantum feature, $2\nu_{dq}$ at τ = 310 ns. The $2\nu_{dq}$ shows magnetic field dependence after the nuclear Zeeman influence correction. *Experimental conditions* are the same as in Figure 5.3.1

For the bis-*cis* complex, the $2\nu_{dq}$ is resolved at all of the magnetic fields (Figure 5.3.3). The $2\nu_{dq}$ line shape and amplitude are altered at different magnetic fields. The $2\nu_{dq}$ shifts from a lower frequency (from approximately 7.75 MHz) to a higher frequency field (8.25 MHz), as the magnetic increases from 2640 Gauss to 3030 Gauss, in the nuclear Zeeman corrected spectrum in Figure 5.3.4. This shift of the $2\nu_{dq}$ feature can be explained, as mentioned above, through the weighting factors. The position of the imidazole planes relative to each other are rotated by 90° and tilted 45° off of the equatorial plane of the Cu(II). If the complex is a single crystal, at a field of 2640 Gauss, the θ angle would be approximately 45°, and the magnetic field will be aligned with the

z-axis of the superhyperfine tensor principal axis, thus the $2\nu_{dq}$ will be resolved as a single line.

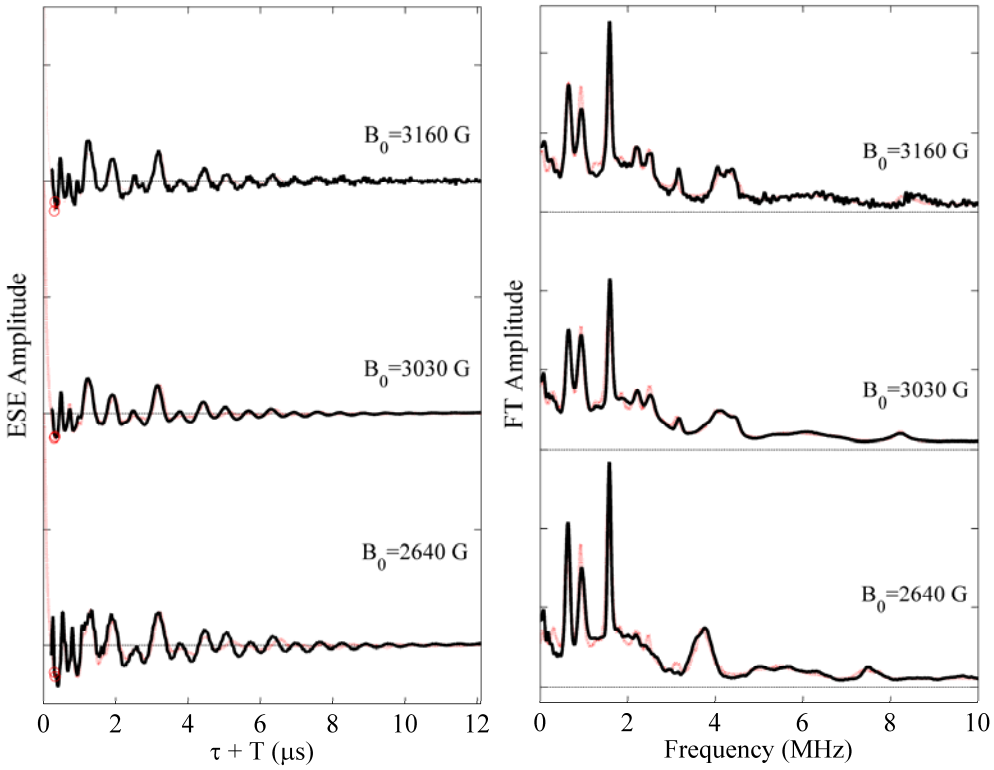

Figure 5.3.3 Orientation selection in three-pulse ESEEM experiment and Fourier transform for bis-*cis* imidazole [Cu(II)(2-MeIm)$_2$(OAc)$_2$], and overlaid simulation (red dashed curve). Simulation parameters are presented in Table 5.3.1. *Experimental conditions:* sample temperature, 6 K; microwave frequency, 8.772 GHz; magnetic field strength, 3030 Gauss; τ = 310 ns; initial *T* value -190 ns; *T* increment, 20 ns; $\pi/2$ pulse width, 20 ns; pulse repetition rate, 120 Hz; 64 pulses per repetition. 3 accumulations: 3160 Gauss; one accumulation: 3030 Gauss; 2 accumulations: 2640 Gauss.

In this case, the sample is randomly oriented (powder sample). Therefore, the $2\nu_{dq}$ line shape at 2640 Gauss is broadened. As the magnetic field is increased, fewer orientations that are aligned with the magnetic field are selected. The shift of the $2\nu_{dq}$ to

higher frequencies as the magnetic field is increased emphasized that the orientation of the imidazole plane are 45° out of the equatorial plane of the Cu(II). This result is consistent with the X-ray crystallographic structure (Figure 3.1.1c). The simulation parameters are shown in Table 5.3.1.

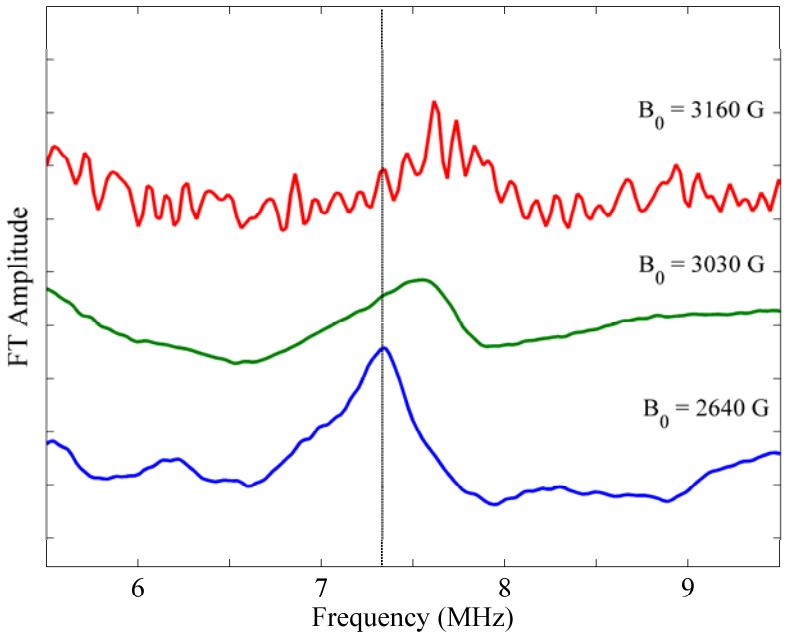

Figure 5.3.4 Orientation selection in three-pulse ESEEM experiment. Fourier transform for the bis-*cis* imidazole [Cu(II)(2-MeIm)$_2$(OAc)$_2$], focus on the double quantum feature, $2\nu_{dq}$. The $2\nu_{dq}$ shows magnetic field dependence after the nuclear Zeeman influence correction. *Experimental conditions* are the same as in Figure 5.3.3

Table 5.3.1 ESEEM simulation parameters for the Cu(II)-imidazole model complexes, using orientation selection with $sin\theta d\theta$ weighting factor at $\tau = 310$ ns.

	single imidazole Cu(II)(Dien)(2-MeIm)	Bis-*trans* imidazole $Cu(II)(Him)_2(NO_3)_2$	Bis-*cis* imidazole $Cu(II)(2\text{-}MeIm)_2(OAc)_2$
A_{xx} (MHz)	2.17	2.09	2.40
A_{yy} (MHz)	1.79	1.64	1.90
A_{zz} (MHz)	1.70	1.40	1.51
A_{iso} (MHZ)	1.89	1.71	1.94
$A_{dip,x}$ (MHz)	0.28	0.38	0.46
$A_{dip,y}$ (MHz)	0.10	0.07	0.04
$A_{dip,z}$ (MHz)	-0.19	-0.31	-0.43
e^2qQ/h (MHz)	1.745	1.479	1.615
η	0.631	0.818	0.728
α_Q(°)	74	321	217
β_Q(°)	297	212	128
γ_Q(°)	299	346	180
α_A(°)		89	231
β_A(°)		2	287
γ_A(°)		245	108
α_{A2}(°)		116	264
β_{A2}(°)		24	188
γ_A(°)		47	210

Chapter 6: Powder ESEEM of ^{15}N- and ^{13}C-labeled Cu(II)-Aβ complexes

6.1 Background

As mentioned in previous chapters, metal ions, in particular, Cu(II), play an important role in AD etiology.[44,116,144] While the exact role of Cu(II) has not yet been identified, two different opposing roles for Cu(II) have been proposed: (1) Cu(II) acts as a neuroprotectant, by preventing the formation of toxic species,[40,53,145-146] and (2) Cu(II) induces Aβ structures that are neurotoxic.[147-148] Therefore, characterizing the coordination environment of Cu(II) in Aβ oligomers is of particular importance for the understanding of AD.

Soluble Aβ has been shown to bind Cu(II) in a square planar coordination environment with predominantly nitrogen coordination.[51,117,144] However, the unambiguous identification of the Cu(II) ligands has remained elusive and, as of yet, no consensus has emerged in the literature.[52] Still, it is generally accepted that metal ions are bound to the hydrophilic, *N*-terminus portion of Aβ species (residues 1-16).[43-44,117] Several studies based on EPR and EXAFS measurements suggest that Cu(II) has a three nitrogen and one oxygen coordination environment in these soluble Aβ, including: Aβ(1-16)[63,105,149], Aβ(1-28)[44,105,117] and Aβ(1-40/42).[63,144,150] However, neither the use of the Peisach and Blumberg correlation,[151] nor the EXAFS studies, allow for a clear distinction between the number of oxygen and nitrogen ligands. EPR and EXAFS, also do not allow for the distinction of the type of nitrogen ligand (i.e amide nitrogen, terminal amino nitrogen, histidine imidazole nitrogen). The EPR line shape is sensitive to the geometry of the Cu(II)-ligand system, and slight tetrahedral distortions from the square-planar

geometry can induce significant changes in the electron Zeeman, hyperfine, quadrupole parameters. However, these changes do not allow for a differentiation between the three possible Cu(II) coordinations: 2N2O, 3N1O, and 4N.[52]

6.2 Using the ESEEM waveform as a tool for ligand identification

ESEEM spectroscopy is a technique for identifying and quantifying the number of interacting imidazoles at a Cu(II) metal center.[38,81-82,94,152] As mentioned in Chapter 2, at exact cancellation the amplitudes of the nuclear quadrupole harmonics allow for the determination of the number of coupled imidazoles thru analysis of the remote ^{14}N. The focus of this chapter is to determine the number of coupled imidazole remote ^{14}N nuclei within samples of Cu(II)-coordinated Aβ(1-16) and Aβ(1-40). The Aβ(1-16) shows no tendency to aggregate or to form fibrils since it does not contain the core hydrophobic sequence, (residues 17-21), which is crucial for Aβ assembly.[13,153] Furthermore, EPR spectroscopy has shown that the Cu(II) binding with Aβ(1-16) is the same as that of Cu(II) bound to Aβ(1-40).[57] Thus, Aβ(1-16) can be considered as a good model for soluble metallated Aβ peptides. Moreover, the histidine residues at positions, 6, 13, and 14 have been proposed to be involved for the metal-Aβ binding by circular dichroism, CW-EPR, UV-visible, potentiometric hyperfine sublevel correlation (HYSCORE) spectroscopic studies.[40,43-44,50,103,149] However, there is still a debate on which of the

histidines are involved in the Cu(II) coordination mode.[46,52] A detailed knowledge of the Cu(II)-Aβ coordination, can provide insight into the fibrillization process, and the role of metal ions, which can potentially aid in developing therapeutic approaches towards combating Alzheimer's disease.[154]

To unravel the ambiguity in the Cu(II) coordination site in Aβ(1-40), the polypeptide was uniformly ^{13}C, ^{15}N-labeled either on His13 or His14 . To observe the interaction between the Cu(II) and the particular possible binding combinations for the soluble and fibrils, four different uniformly ^{13}C, ^{15}N-labeled Aβ(1-40) peptide were prepared. As a result, the Larmor frequency of the Aβ(1-40) peptide will change. Therefore, instead of having the nuclear spin of $I = 1$, for ^{14}N, the nuclear spin is $I = 1/2$ for ^{15}N. For example, for ^{14}N, at 3030 G, the $\nu_N = 0.93$ MHz, whereas for ^{15}N, $\nu_N = 1.31$ MHz. The same is true for the ^{13}C-labeled (I = 1/2), where $\nu_N = 3.24$ MHz. The labeled Aβ(1-40) was studied in its two possible forms, soluble and fibrillar. Furthermore, the soluble unlabeled Aβ(1-40), and Aβ(1-16) served as the control samples..

In previous Chapters, the Fourier transform (i.e. the frequency spectra) of the ESEEM allowed for a qualitative analysis of the number of ^{14}N nuclei coupled to Cu(II). However, in the ESEEM waveform, the decay time of the modulation is fast, causing an artifact in the FT; especially, where the nuclear quadrupole harmonics are expected to be for all 6 samples. Therefore, the analysis was done only on the ESEEM waveforms, as they do not suffer from truncation, phase-matching and rescaling artifacts, which are sometimes present in the FT spectra.

The ESEEM waveforms for each sample were simulated by considering the five possible ^{14}N coordination's to Cu(II): 1 ^{14}N nucleus, 2, 3 and 4 homogeneous ^{14}N nuclei, and 4 heterogeneous nuclei. Here, "homogenous ^{14}N nuclei" refers to identical properties of electron Zeeman, nuclear Zeeman, hyperfine, quadrupole parameters, for all nuclei. The heterogeneous nuclei refer to a sample where different proportions of the 1, 2, 3 and 4 homogenous nuclei were present within the same sample. These simulations are shown in Figures 6.1-6. Through visual comparisons of the experimental and calculated ESEEM waveforms a preliminary assignment of the number of His ligands coordinated to the Cu(II) was made.

For example, for Aβ(1-40) with labeled ^{13}C-^{15}N-His14, the ESEEM spectrum shows a sustained modulation, and at early time points (from 0.1-1 μs) the waveform has two features which are relatively narrow compared to the modulation at longer $\tau + T$. As can be seen in the calculated waveforms, and from literature results,[81-82] the relative amplitudes of these peaks depend on the number of coordinated nuclei.[81-82]

As observed in our Cu(II) model complexes, (Chapter 4 and 6), these two sharp feactures have the same amplitude in the ESEEM waveform for the single imidazole (Figure 4.2). This result matches the ESEEM results obtained by Jiang et al.[82] The waveform for their complex (Cu(II)-dienthylenetriamine imidazole) sample, shows the two narrow features with the same amplitude. The ESEEM waveform for the Cu(II) bis-imidazole samples show these features with different amplitudes (Figure 4.3-4). The amplitude of these two features increases with the number of bound ligands. As shown by McCracken et al.,[81] with their Cu(II) tetrakis(2-methylimidazole) complex, the ESEEM waveform has the first sharp feature (around 4 μs) with an amplitude twice as

large as the second peak (at 7 μs). Therefore, these results allow us to use the ESEEM waveform to make a qualitative determination of the number of nuclei bound to Cu(II).

6.2.1 Labeled Aβ(1-40)-^{13}C-^{15}N samples

As discussed previously, the ESEEM waveform can provide information on the number of bound nuclei. For the labeled fibril samples, Figures 6.2.1.1 and 6.2.1.2, the two sharp features, that represent the number of coordinated nuclei, show little change for 2 or 3 bound nuclei. In order to de-convolute these results, the other features of the ESEEM waveform need to be considered. These include a small feature around 1 μs and the time decay of the modulation. The small feature at 1 μs is apparent in four scenarios: 4 different nuclei, 2,3 and 4 identical ^{14}N. However, the decrease of the modulation was comparably different for each of those possible cases.

The modulation for each labeled fibril sample decreased until approximately 5 μs, but at longer times the signal to noise was too poor to resolve any further modulation (as shown in Figures 6.2.1.1 and 6.2.1.2). Therefore, the best comparison obtained from the simulation for each of the labeled Aβ(1-40) fibril samples corresponds to 2 identical ^{14}N nuclei bound to the metal center, which has a sustained decrease in modulation for a longer time compared to the other possible cases.

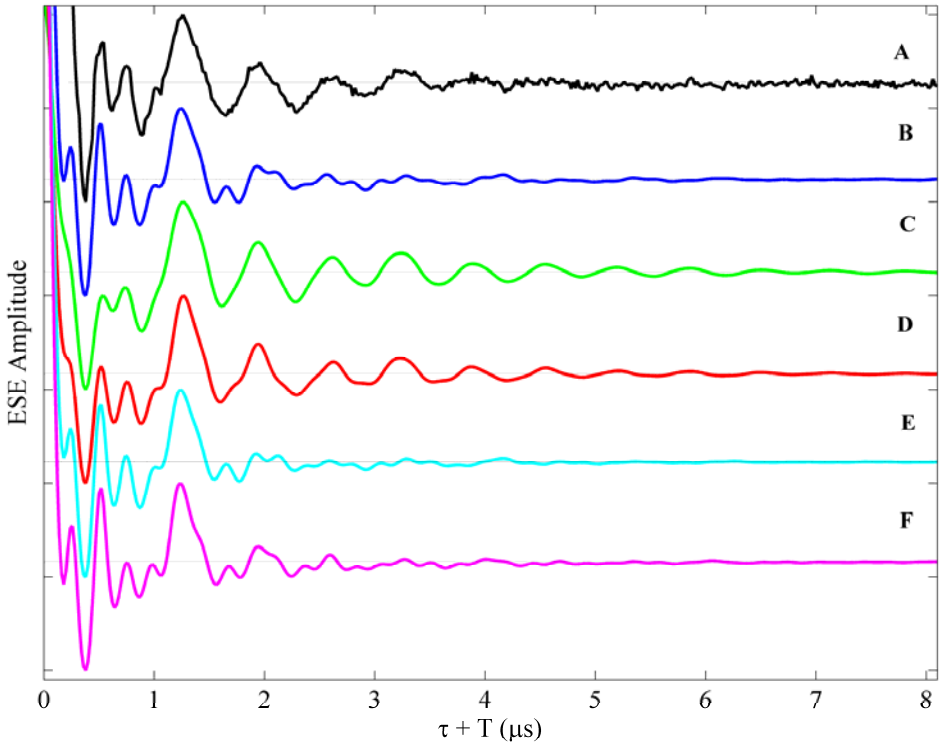

Figure 6.2.1.1 Experimental powder three-pulse ESEEM for determining Cu(II)-Aβ(1-40) fibrillar complex coordination environment. Fibrils were uniformly ^{15}N, ^{13}C – labeled at H13. **A**. Experimental spectrum. Waveform simulations for **B.** 4 different ^{14}N nuclei coupled; **C**. one ^{14}N nucleus coupled to Cu(II); **D**. 2 identical nuclei coupled; **E.** 3 identical nuclei coupled; **F.** 4 identical ^{14}N nuclei coupled. Simulation parameters are given in Table 6.2.1.1 *Experimental Conditions:* sample temperature, 6 K; microwave frequency, 8.772 GHz; magnetic field strength, 3030 Gauss; τ value 156 ns; initial τ + T value, -36 ns; *T* increment, 20 ns; π/2 pulse width, 20 ns; pulse repetition rate 120 Hz; 64 pulse per repetition; average of 3 accumulations as noted.

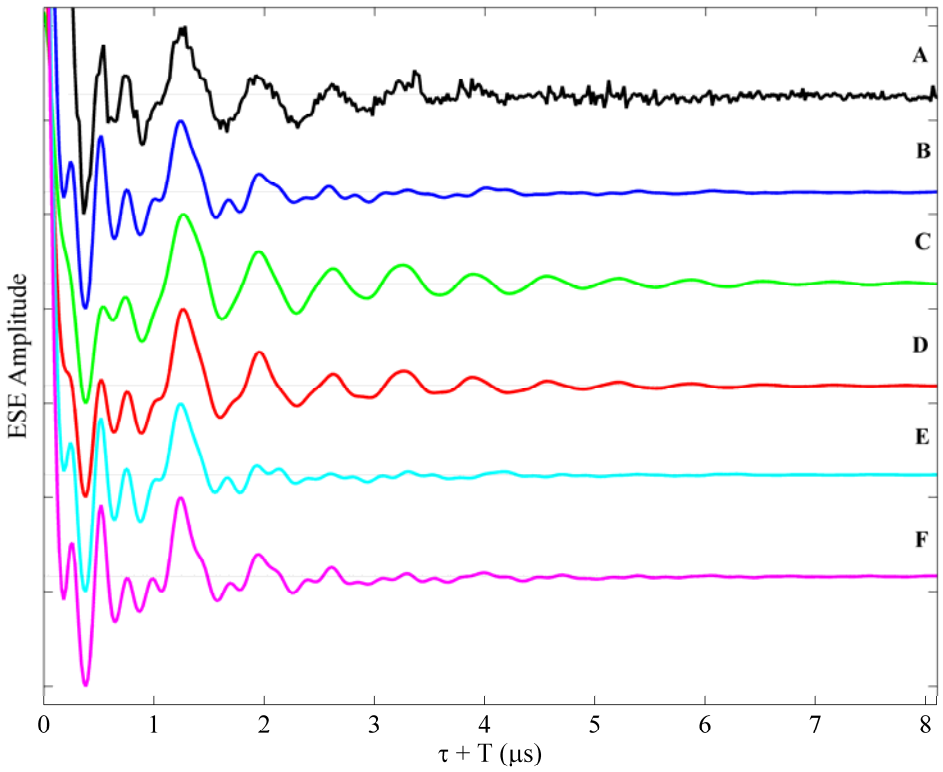

Figure 6.2.1.2 Experimental powder three -pulse ESEEM for determining Cu(II)-Aβ(1-40) fibrillar complex coordination environment. Fibrils were uniformly ^{15}N, ^{13}C – labeled at H14. **A**. Experimental spectrum. Waveform simulations for **B.** 4 different ^{14}N nuclei coupled; **C**. one ^{14}N nucleus coupled to Cu(II); **D**. 2 identical nuclei coupled; **E.** 3 identical nuclei coupled; **F.** 4 identical ^{14}N nuclei coupled. Simulation parameters are given in Table 6.2.1.1. *Experimental Conditions:* sample temperature, 6 K; microwave frequency, 8.772 GHz; magnetic field strength, 3030 Gauss; τ value 156 ns; initial τ + T value, -36 ns; *T* increment, 20 ns; π/2 pulse width, 20 ns; pulse repetition rate 120 Hz; 64 pulse per repetition; average of 3 accumulation as noted.

Table 6.2.1.1 Three-pulse ESEEM simulation parameters for the uniformly labeled fibrils Aβ40 + Cu(II) ^{13}C-^{15}N-His13 peptide complexes

	fibrils Aβ40 + Cu(II) ^{13}C-^{15}N-His13				
	4 sites	**1: ^{14}N**	**2: ^{14}N**	**3: ^{14}N**	**4: ^{14}N**
A_{xx} **(MHz)**	0.82	1.23	1.41	0.72	0.82
A_{yy} **(MHz)**	1.59	1.41	1.20	1.64	1.38
A_{zz} **(MHz)**	2.26	2.13	2.11	2.24	2.23
e^2qQ **(MHz)**	1.56	1.56	1.56	1.56	1.55
η	0.59	0.80	0.80	0.58	0.65
α_Q **(°)**	180	84	0	0	0
β_Q **(°)**	270	270	270	90	90
γ_Q **(°)**	0	180	0	0	180

Table 6.2.1.2 Three-pulse ESEEM simulation parameters for the uniformly labeled fibrils Aβ40 + Cu(II) ^{13}C-^{15}N-His14 peptide complexes

	fibrils Aβ40 + Cu(II) ^{13}C-^{15}N-His14				
	4 sites	**1: ^{14}N**	**2: ^{14}N**	**3: ^{14}N**	**4: ^{14}N**
A_{xx} **(MHz)**	0.84	1.23	1.33	1.62	0.87
A_{yy} **(MHz)**	1.50	1.38	1.23	0.72	1.31
A_{zz} **(MHz)**	2.22	2.12	2.11	2.22	2.21
e^2qQ **(MHz)**	1.57	1.56	1.56	1.56	1.55
η	0.60	0.79	0.76	0.58	0.65
α_Q **(°)**	0	90	204	272	180
β_Q **(°)**	270	90	90	270	90
γ_Q **(°)**	0	180	0	0	0

The labeled Aβ(1-40) soluble sample, Aβ(1-40)-^{13}C-^{15}N-His13, has an ESEEM waveform which is comparable to either 2 or 3 identical ^{14}N nuclei (Figure 6.2.1.3 A, D and E). The signal-to-noise is poor, which makes it difficult to distinguish between the two cases.

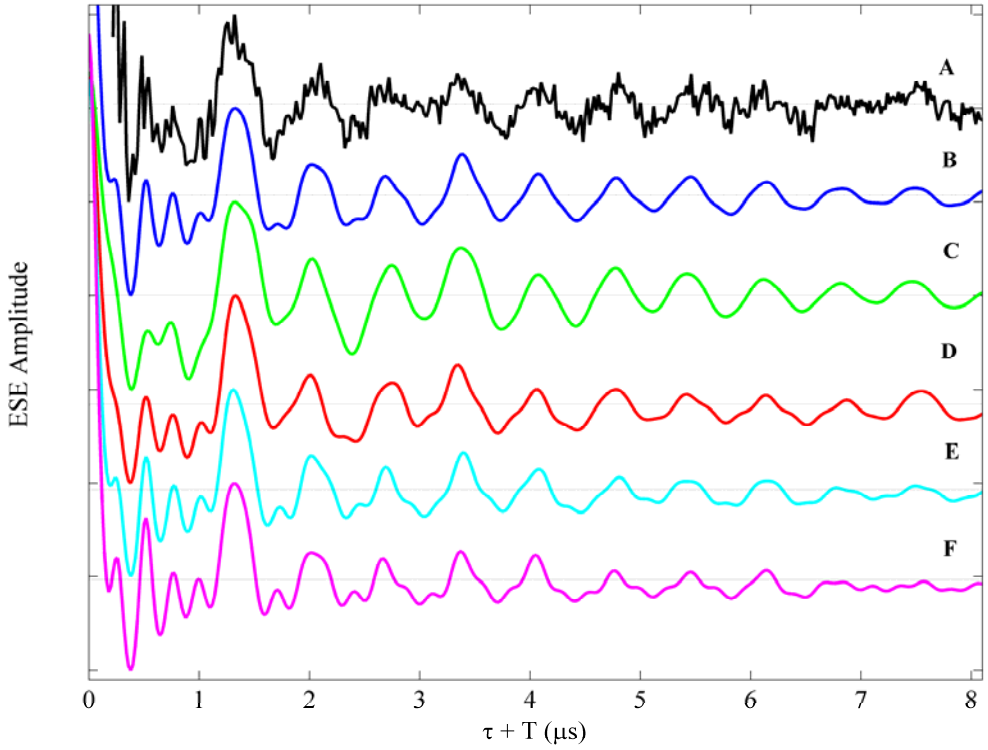

Figure 6.2.1.3 Experimental powder three -pulse ESEEM for determining Cu(II)-Aβ(1-40) soluble complex coordination environment. The soluble complex was uniformly ^{15}N, ^{13}C – labeled at H13. **A**. Experimental spectrum. Waveform simulations for **B.** 4 different ^{14}N nuclei coupled; **C**. one ^{14}N nucleus coupled to Cu(II); **D**. 2 identical nuclei coupled; **E.** 3 identical nuclei coupled; **F.** 4 identical ^{14}N nuclei coupled. Simulation parameters are given in Table 6.2.1.3 *Experimental Conditions:* sample temperature, 6 K; microwave frequency, 8.772 GHz; magnetic field strength, 3030 Gauss; τ value 156 ns; initial τ + T value, -36 ns; *T* increment, 20 ns; $\pi/2$ pulse width, 20 ns; pulse repetition rate 120 Hz; 64 pulse per repetition; average of 2 accumulations as noted.

The decay of the modulation after 2 μs decreases slowly for the two possible cases, 2 or 3 identical ^{14}N nuclei. The modulation for 3 identical ^{14}N nuclei presents certain heterogeneity. This heterogeneity could be the result of certain ^{14}N nuclei relaxing faster than others, suggesting that the samples might have some aggregates. Nevertheless, any heterogeneity in the ESEEM waveform would not be apparent due to the poor signal-to-noise ratio of the ESEEM time-domain spectra. Therefore, the soluble labeled samples cannot be uniquely assigned as either 2 or 3 identical ^{14}N nuclei.

The labeled soluble Aβ(1-40)-^{13}C-^{15}N-His14 sample has poorest signal/noise ratio, as shown in Figure 6.2.1.4. Thus, no assignment of the coordination can be made for this soluble peptide.

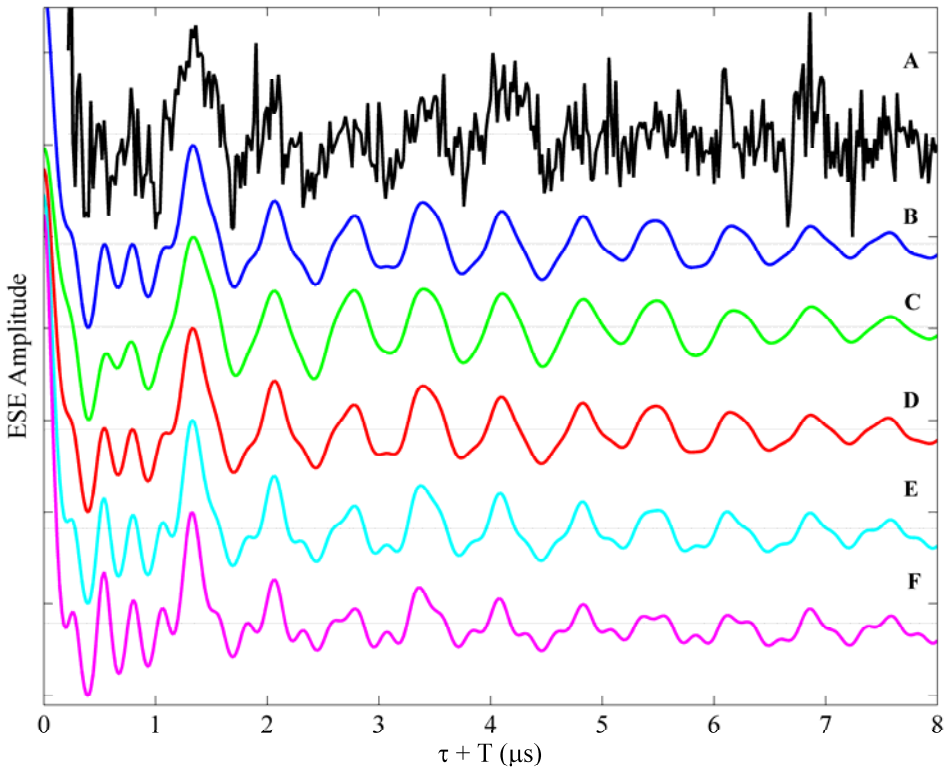

Figure 6.2.1.4 Experimental powder three -pulse ESEEM determining Cu(II)-Aβ(1-40) soluble complex coordination environment. The soluble complex was uniformly ^{15}N, ^{13}C – labeled at H14. **A.** Experimental spectrum. Waveform simulations for **B.** 4 different ^{14}N nuclei coupled; **C**. one ^{14}N nucleus coupled to Cu(II); **D**. 2 identical nuclei coupled; **E.** 3 identical nuclei coupled; **F.** 4 identical ^{14}N nuclei coupled. Simulation parameters are given in Table 6.2.1.4 *Experimental Conditions:* sample temperature, 6 K; microwave frequency, 8.772 GHz; magnetic field strength, 3030 Gauss; τ value 156 ns; initial τ + T value, -36 ns; *T* increment, 20 ns; π/2 pulse width, 20 ns; pulse repetition rate 120 Hz; 64 pulse per repetition; one accumulation as noted.

Table 6.2.1.3 Three-pulse ESEEM simulation parameters for the soluble Aβ40 + Cu(II) ^{13}C-^{15}N-His13

	soluble Aβ40 + Cu(II) ^{13}C-^{15}N-His13				
	4 sites	**1: ^{14}N**	**2: ^{14}N**	**3: ^{14}N**	**4: ^{14}N**
A_{xx} **(MHz)**	1.41	1.29	1.05	1.38	1.17
A_{yy} **(MHz)**	1.24	1.82	1.79	1.15	1.27
A_{zz} **(MHz)**	2.13	2.26	2.20	2.08	2.16
e^2qQ **(MHz)**	1.50	1.49	1.47	1.50	1.49
η	0.77	0.83	0.88	0.76	0.74
α_Q (^{0})	323	180	53	49	177
β_Q (^{0})	91	18	37	84	271
γ_Q (^{0})	179	90	219	177	177

Table 6.2.1.4 Three-pulse ESEEM simulation parameters for the soluble Aβ40 + Cu(II) ^{13}C-^{15}N-His14

	soluble Aβ40 + Cu(II) ^{13}C-^{15}N-His14				
	4 sites	**1: ^{14}N**	**2: ^{14}N**	**3: ^{14}N**	**4: ^{14}N**
A_{xx} **(MHz)**	1.27	1.43	1.37	1.40	1.44
A_{yy} **(MHz)**	1.85	1.23	1.28	1.21	1.13
A_{zz} **(MHz)**	1.39	1.86	1.86	1.86	1.85
e^2qQ **(MHz)**	1.49	1.47	1.49	1.50	1.50
η	0.80	0.83	0.78	0.78	0.78
α_Q (^{0})	340	13	193	210	36
β_Q (^{0})	353	90	92	88	80
γ_Q (^{0})	294	180	357	2	178

6.2.2 Unlabeled Aβ(1-40) and Aβ(1-16)

For the unlabeled samples, Aβ(1-40) and Aβ(1-16), the ESEEM waveform shows two features at the lower end of the $\tau + T$ domain, which allows for the determination of the number of ^{14}N bound to Cu(II). Through inspection of the spectra for the unlabeled sample, Aβ(1-40), the difference in amplitude for the two sharp features corresponds to the 3 identical ^{14}N nuclei (as shown in Figure 6.2.2.1). However, the modulation is present until 5 μs, which does not correspond to the modulation for the 3 identical ^{14}N nuclei, which decays more rapidly. The longer modulation decay correlates with 2 identical ^{14}N nuclei. Therefore, the polypeptide sample could be binding through 2 or 3 identical ^{14}N nuclei.

The same ambiguity arises for the soluble Aβ(1-16) sample. As shown in Figure 6.2.2.2, the two sharp features, which have been used as the determinant factor for the number of nuclei binding, have different amplitudes. The first feature has a larger amplitude when compared to the second feature. The difference in amplitude from both features corresponds to a coordination of 3 identical ^{14}N nuclei. However, the ESEEM modulation compares well to both 2 or 3 identical ^{14}N. The simulated modulation for the 3 identical ^{14}N nuclei, shows some heterogeneity, but the experimental data signal-to-noise does not allow these heterogeneities to be observed. Thus, we cannot definitively assign the Cu(II) coordination to be either two or three histidine ligands.

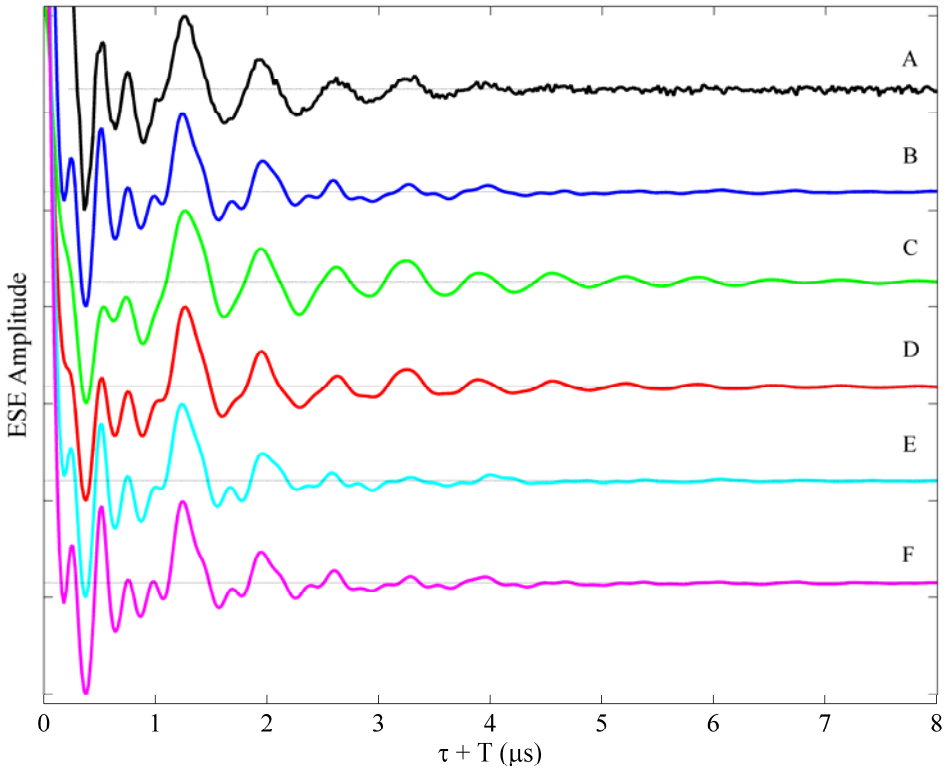

Figure 6.2.2.1. Experimental powder three -pulse ESEEM for determining Cu(II)-Aβ(1-40) soluble complex coordination environment. **A**. Experimental spectrum. Waveform simulations for **B.** 4 different ^{14}N nuclei coupled; **C**. one ^{14}N nucleus coupled to Cu(II); **D**. 2 identical nuclei coupled; **E.** 3 identical nuclei coupled; **F.** 4 identical ^{14}N nuclei coupled. Simulation parameters are given in Table 6.2.2.1. *Experimental Conditions:* sample temperature, 6 K; microwave frequency, 8.772 GHz; magnetic field strength, 3030 Gauss; τ value 156 ns; initial τ + T value, -36 ns; *T* increment, 20 ns; π/2 pulse width, 20 ns; pulse repetition rate 120 Hz; 64 pulse per repetition; average of 2 accumulations as noted.

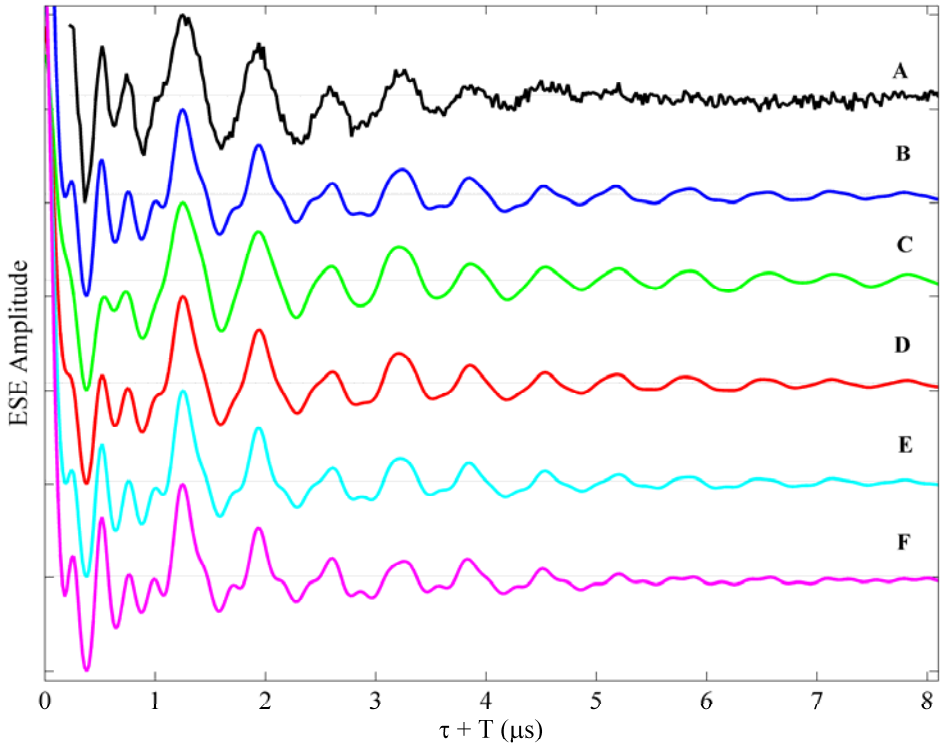

Figure 6.2.2.2 Experimental powder three -pulse ESEEM for determining Cu(II)- Aβ(1-16) soluble complex coordination environment. **A.** Experimental spectrum. Waveform simulations for **B.** 4 different ^{14}N nuclei coupled; **C**. one ^{14}N nucleus coupled to Cu(II); **D**. 2 identical nuclei coupled; **E.** 3 identical nuclei coupled; **F.** 4 identical ^{14}N nuclei coupled. Simulation parameters are given in Table 6.2.2.2. *Experimental Conditions:* sample temperature, 6 K; microwave frequency, 8.772 GHz; magnetic field strength, 3030 Gauss; τ value 156 ns; initial τ + T value, -36 ns; *T* increment, 20 ns; $\pi/2$ pulse width, 20 ns; pulse repetition rate 120 Hz; 64 pulse per repetition; average of 7 accumulation as noted.

Table 6.2.2.1 Three-pulse ESEEM simulation parameters for soluble Cu(II)-Aβ(1-40) peptide complexes

	Aβ40 soluble + Cu(II)				
	4 sites	**1: ^{14}N**	**2: ^{14}N**	**3: ^{14}N**	**4: ^{14}N**
A_{xx} **(MHz)**	1.38	1.24	1.38	0.90	1.28
A_{yy} **(MHz)**	0.98	1.42	1.24	1.49	0.98
A_{zz} **(MHz)**	2.23	2.13	2.11	2.24	2.21
e^2qQ **(MHz)**	1.57	1.56	1.57	1.58	1.56
η	0.63	0.77	0.77	0.59	0.66
α_Q (^{0})	270	270	172	179	270
β_Q (^{0})	90	270	90	90	270
γ_Q (^{0})	0	0	0	0	180

Table 6.2.2.2 Three-pulse ESEEM simulation parameters for soluble Cu(II)-Aβ(1-16) peptide complexes

	Aβ16 soluble + Cu(II)				
	4 sites	**1: ^{14}N**	**2: ^{14}N**	**3: ^{14}N**	**4: ^{14}N**
A_{xx} **(MHz)**	1.13	1.50	1.12	1.35	1.19
A_{yy} **(MHz)**	1.39	1.05	1.43	1.11	1.12
A_{zz} **(MHz)**	2.15	2.13	2.11	2.13	2.15
e^2qQ **(MHz)**	1.59	1.59	1.59	1.58	1.57
η	0.72	0.75	0.73	0.73	0.72
α_Q (^{0})	319	140	47	40	84
β_Q (^{0})	95	90	89	81	259
γ_Q (^{0})	181	180	179	184	358

6.3 Literature review for the conundrum of the number of histidines involved on the Cu(II)-Aβ(1-16/40) binding site

As shown above, the Cu(II)-coordination site in the Aβ protein is still uncertain. The current assignment of two or three histidines coordinating to the Aβ complexes studied represents a dichotomy in the fits shown in both the early and later times of the modulation. These results agree with the conundrum found in the literature. Using a variety of techniques, such as advanced EPR spectroscopy techniques (HYSCORE, ESEEM), UV-visible spectra, and circular dichroism, have suggested that Cu(II) binds to either two,[46,103,155-157] or three[40,48,50,63,117-118,149,158] histidine residues. The only agreement which has been reached is that the N-terminus region of the peptide contains the major metal binding site.[44,105,117,158-159] While, most of the studies suggest a coordination involving all the three histidines (His6, His13, and His14) the manner in which they coordinate, and the potential involvement of the N-terminal amino nitrogen (N_a), and the side-chain carboxylate oxygen (O_c) Asp1, Glu3, Asp7, and Glu11 remains unknown. A pH-dependence of Aβ/Cu(II) has shown that two distinct species can be formed.[105,117,160] At low pH (<5), Kowalik-Jankowska and co-workers, using potentiometric and spectroscopic date (UV-visible, CD, EPR), showed that the Cu(II) coordination involved all three histidines, and at physiological pH (7.4), they suggested a 2 histidine Cu(II) coordination involving Asp1 (N_a, O_c), His13 and His14 .[105] Viles and co-workers, assigned all three histidines (His6, His13 and His14) as being involved in the Cu(II)-Aβ coordination at pH = 7.4 through their results obtained from UV-visible, CD, EPR and NMR spectroscopic data.[117] However, Shearer and Szalai hypothesized that at

physiological pH, only His13 and His14 are involved on the Cu(II)-Aβ coordination, based on their EXAFS results for Cu(II)-Aβ.[156] Using a wide range of EPR methods, including CW-EPR, ESEEM, and 4-pulse HYSCORE, Dorlet and co-workers suggested a two histidine coordination mode of Cu(II) involving Asp1, His6 and either His13 or His14.[157]

The Cu(II) coordination to Aβ has been of interest for more than a decade, and there are still ambiguities on the number of histidines involved in the Cu(II)/Aβ binding. As shown in the ESEEM waveforms for the ^{13}C, ^{15}N-labeled Aβ(1-40) samples, the differences between two or three coordinate imidazole are subtle. This ambiguity between two or three imidazoles present in the Cu(II)-binding could possibly be discerned by studying an unlabeled fibril Aβ(1-40), which will serve as a control. This control will allow for direct comparaison to the current results. In addition, the residue His6 could also be labeled to quantitatively determine the residues which are responsible for the metal binding.

Chapter 7: Conclusions and future directions

For more than a century, Alzheimer's disease (AD) has been known to be a fatal and progressive disease affecting roughly 26 million people worldwide,[161] with no known cure. As mentioned previously, AD is associated with the aggregation and fibrillization of the amyloid-β protein (Aβ). The association of Aβ with metal ions, such as Cu(II) and Zn(II) has been correlated with AD.[35-37] *In vitro* studies have shown that the Cu(II) ions either accelerate or arrest fibrillization, depending upon the peptide length and amino acid sequence in truncated and mutated Aβ peptides. The presence of Cu(II) has also been shown to affect the morphology of the fibril structure.[38] In order to gain insight into the factors that govern fibrillization, the molecular structure of the Cu(II)-histidine imidazole coordination was examined in cryotrapped soluble and fibrillar forms of Aβ peptides, [Aβ(1-40), Aβ(1-16), Aβ(13-21)] and the following model complexes: a single imidazole [Cu(II)-diethylenetriamine 2-methylimidazole], and two different bis-imidazole complexes: bis-*trans* imidazole [Cu(II)-bis-histamine-bis-nitrate], bis-*cis* imidazole [Cu(II)-bis-(acetate)-bis-(2-methylimidazole)]. All of the model complexes were synthesized and studied by X-band continuous-wave electron paramagnetic resonance (EPR) and electron spin echo envelope modulation (ESEEM) spectroscopies.

The results from our hybrid optimization-based OPTESIM simulation software[162] were in accordance with the literature results for the Cu(II)-model complexes. The dipolar superhyperfine tensor (shf) for the single imidazole was [A_{xx} A_{yy} A_{zz}] = [0.49 0.02 -0.5] MHz. The dipolar shf tensor for the bis-*trans* complex was [0.53 0.21 -0.75] MHz, and for the bis-*cis* complex was [0.56 -0.10 -0.47] MHz. Therefore, the distinction

between bis-*trans* and -*cis* can be made with the inclusion of the shf principal axis system (PAS)-molecular PAS correlation from the single-crystal ESEEM simulation.[66,92-93] The technique has been applied Aβ(13-21)H14A, and the dipolar shf tensor is $[A_{xx}\ A_{yy}\ A_{zz}]$ = [0.44 0.02 -0.45] MHz. A physical model for the Aβ(13-21)H14A was created using the shf Euler angles $[\alpha_A, \beta_A, \gamma_A]$ = [354 70 298] and the coordination mode is assigned as bis-*cis*. This physical model for Aβ(13-21)H14A shows the unique coordination of Cu(II) binding to the Aβ peptide and its role in β-sheet formation. The bis-*cis* conformation forces the Cu(II) coordination to distort the N-terminus of Aβ(13-21)H14A, which is in agreement with previously proposed models.[25,30] The Aβ(13-21)H14A is a good mimic for the Aβ(1-40) peptide since it has both hydrophilic and hydrophobic termini, but also has similar toxicity as Aβ(1-40) when Cu(II) is present. Therefore, these results provide important information towards the understanding of metal binding and β-sheet formation in amyloid plaques, and will lead to a better understanding of the fibrillization process.

Orientation selection was performed on the Cu(II) model complexes and the Aβ(13-21) peptides, allowing the *z*-axis of shf PAS to be related to the g_z-axis of the tensor of the Cu(II). From the orientation of the *z*-axis of shf PAS and the g_z-axis of the tensor of the Cu(II), the orientation of the imidazole planes with respect to the g_z-axis of the Cu(II) was determined. The precise arrangement of the individual peptides in Aβ peptide fibrils has been elusive. Therefore, these results compliment the $2\nu_{dq}$ analysis by adding another constraint on the possible conformation of the Cu(II) binding to the Aβ peptide through the determination of the histidines coordination with the metal ion. The difference in

structures when Cu(II) is bound to Aβ will be explained by these results, showing that the conformation of Cu(II) with Aβ is restricted and forcing the β-sheet to have different structure compared to the Aβ with no metal, as shown in the AFM images of the Aβ(13-21)H14A peptides.[38]

For the full length of Aβ(1-40), two distinct ways in which the metal ion can bind the peptide have been suggested,[44,158] which are commonly referred to as inter- and intra-molecular modes. The inter-molecular mode correspond to the cross-linking between β-strands with Cu(II) in between (i.e. Aβ-Cu(II)-Aβ), while in the intra-molecular mode the atoms participating in the metal coordination all belong to the same peptide. Different structural models have been proposed in which different numbers of histidine residues (either two or three) are involved in the metal coordination,[50] but no consensus have been set on the number of histidines being responsible for this metal coordination. The number of coordinated histidine imidazoles in Cu(II)-Aβ(1-40) is addressed by ESEEM of ^{15}N-His13 or ^{15}N-His14 peptides. The modulation showed distinct features that depend on the number of imidazoles bound to Cu(II). For the labeled fibrils, two ^{14}N were involved in the Cu(II) binding. Soluble samples showed either two or three ^{14}N nuclei bound. These results were consistent with the conundrum found in the literature, where different groups suggested that Cu(II) binds to either two[46,103,155-157] or three[40,48,50,63,117-118,149,158] histidine residues. While most of the studies suggest a coordination involving three histidines (His6, His13, and His14) the manner in which they coordinate and the potential involvement of the N-terminal amino nitrogen (N_a), and the side-chain carboxylate oxygen (O_c) from residues Asp1, Glu3, Asp7 and Glu11 remains unknown. Also, the environment in which the Aβ peptide is present (i.e. pH,

buffer conditions, solubility of Aβ form, temperature) affects the metal binding coordination,[52] permitting both two and three histidine residues to coordinate with Cu(II). The differences between two or three ^{14}N nuclei coordinated imidazoles are subtle in the ESEEM waveform, and our experiments require higher signal-to-noise to resolve these subtleties. Also, a control sample, Aβ(1-40) fibril unlabelled, will allow for a direct comparison to the current results for the ^{15}N-labeled Aβ(1-40). In addition, studies of two different Cu(II)-imidazole model complexes (e.g. bis- and tris-imidazole respectively) can be used to resolve the differences in the ESEEM waveform in a quantitative manner. The signal-to-noise will be significant lower compared to the Aβ peptides complexes, and simulations can be performed giving quantitative results on the values of the superhyperfine, nuclear quadrupole and the superhyperfine euler angles, which can then serve as models for the results of the Aβ peptide, and potentially resolve the conundrum of two or three identical remote ^{14}N imidazole nuclei in the histidine ligands.

The results presented in this dissertation show the power of ESEEM as a tool for the determination of the molecular structure in Aβ proteins. The powder ESEEM analysis of the $2\nu_{dq}$ line shape can provide information about the relative orientation of the remote ^{14}N shf PAS, and is capable of distinguishing *trans* and *cis* imidazole coordination. Furthermore, the orientation of the shf PAS with the *g*-tensor PAS of the Cu(II) can be determined through orientation selection, allowing more constraints to be set on the coordination of the Cu(II)-Aβ binding to gain insight into the fibrillization process. Finally, the ESEEM waveform provides information on the number of ^{14}N bound to the metal ion.

The methods presented can be expanded to future work on determining the molecular structure of a tris-imidazole Cu(II) model complex, in order to get a quantitative comparison between two and three ^{14}N nuclei coordinated to Cu(II). The Cu(II)-imidazole model can then be applied to the Aβ peptide, and a quantitative analysis will allow for the determination of the molecular structure of different congeners of Aβ peptides. Literature results have shown that the 1-16 residue domain is generally considered the binding region for Cu(II) in Aβ peptides.[105,163-165] This short peptide, Aβ(1-16) serves as a good model for determining which histidines are responsible for the metal binding in Aβ peptides. For the Aβ(1-40) fibrils, the methodology and results of Aβ(13-21)H14A can be useful for discerning the fibrillization process in the full length peptide. Both soluble and fibrillar forms of Aβ peptides are present *in vivo*.[37] Therefore, understanding the physical and chemical proterties of each individual amino acid interaction with Cu(II) will open a door for determining the activity governing the assembly and toxicity of the whole fibrils, and the role that Cu(II) plays in Aβ peptide aggregation and Alzheimer's disease.

Bibliography:

(1) Ziegler-Graham, K.; Brookmeyer, R.; Johnson, E.; Arrighi, H. M. *Alzheimers Dement* **2008**, *4*, 316.

(2) Wisniewski, T.; Ghiso, J.; Frangione, B. *Neurobiol Dis* **1997**, *4*, 313.

(3) Masters, C. L.; Simms, G.; Weinman, N. A.; Multhaup, G.; Mcdonald, B. L.; Beyreuther, K. *P Natl Acad Sci USA* **1985**, *82*, 4245.

(4) Glenner, G. G.; Wong, C. W. *Biochem Bioph Res Co* **1984**, *120*, 885.

(5) Nunan, J.; Small, D. H. *Febs Lett* **2000**, *483*, 6.

(6) Seubert, P.; Vigopelfrey, C.; Esch, F.; Lee, M.; Dovey, H.; Davis, D.; Sinha, S.; Schlossmacher, M.; Whaley, J.; Swindlehurst, C.; Mccormack, R.; Wolfert, R.; Selkoe, D.; Lieberburg, I.; Schenk, D. *Nature* **1992**, *359*, 325.

(7) Selkoe, D. J.; Citron, M.; Yamazaki, T.; Teplow, D. B.; Haass, C. *Neurobiol Aging* **1994**, *15*, S69.

(8) Haass, C.; Schlossmacher, M. G.; Hung, A. Y.; Vigopelfrey, C.; Mellon, A.; Ostaszewski, B. L.; Lieberburg, I.; Koo, E. H.; Schenk, D.; Teplow, D. B.; Selkoe, D. J. *Nature* **1992**, *359*, 322.

(9) Walsh, D. M.; Tseng, B. P.; Rydel, R. E.; Podlisny, M. B.; Selkoe, D. J. *Biochemistry-Us* **2000**, *39*, 10831.

(10) Geula, C.; Wu, C. K.; Saroff, D.; Lorenzo, A.; Yuan, M. L.; Yankner, B. A. *Nat Med* **1998**, *4*, 827.

(11) Findeis, M. A. *Pharmacol Therapeut* **2007**, *116*, 266.

(12) Spoelgen, R.; von Arnim, C. A. F.; Thomas, A. V.; Peltan, I. D.; Koker, M.; Deng, A.; Irizarry, M. C.; Andersen, O. M.; Willnow, T. E.; Hyman, B. T. *J Neurosci* **2006**, *26*, 418.

(13) Benzinger, T. L. S.; Gregory, D. M.; Burkoth, T. S.; Miller-Auer, H.; Lynn, D. G.; Botto, R. E.; Meredith, S. C. *P Natl Acad Sci USA* **1998**, *95*, 13407.

(14) Tycko, R. *Biochemistry-Us* **2003**, *42*, 3151.

(15) Tamaoka, A.; Odaka, A.; Ishibashi, Y.; Usami, M.; Suzuki, N.; Sahara, N.; Sawamura, N.; Shoji, S.; Mori, H. *J Neurochem* **1995**, *65*, S75.

(16) Roher, A. E.; Lowenson, J. D.; Clarke, S.; Woods, A. S.; Cotter, R. J.; Gowing, E.; Ball, M. J. *P Natl Acad Sci USA* **1993**, *90*, 10836.

(17) Verdier, Y.; Penke, B. *Curr Protein Pept Sc* **2004**, *5*, 19.

(18) Verdier, Y.; Zarandi, M.; Penke, B. *J Pept Sci* **2004**, *10*, 229.

(19) Chaney, M. O.; Stine, W. B.; Kokjohn, T. A.; Kuo, Y. M.; Esh, C.; Rahman, A.; Luehrs, D. C.; Schmidt, A. M.; Stern, D.; Yan, S. D.; Roher, A. E. *Bba-Mol Basis Dis* **2005**, *1741*, 199.

(20) Di Carlo, M. *Eur Biophys J Biophy* **2010**, *39*, 877.

(21) Walsh, D. M.; Lomakin, A.; Benedek, G. B.; Condron, M. M.; Teplow, D. B. *J Biol Chem* **1997**, *272*, 22364.

(22) Kheterpal, I.; Zhou, S.; Cook, K. D.; Wetzel, R. *P Natl Acad Sci USA* **2000**, *97*, 13597.

(23) Makin, O. S.; Atkins, E.; Sikorski, P.; Johansson, J.; Serpell, L. C. *P Natl Acad Sci USA* **2005**, *102*, 315.

(24) Paravastu, A. K.; Leapman, R. D.; Yau, W. M.; Tycko, R. *P Natl Acad Sci USA* **2008**, *105*, 18349.

(25) Burkoth, T. S.; Benzinger, T. L. S.; Urban, V.; Morgan, D. M.; Gregory, D. M.; Thiyagarajan, P.; Botto, R. E.; Meredith, S. C.; Lynn, D. G. *J Am Chem Soc* **2000**, *122*, 7883.

(26) Petkova, A. T.; Yau, W. M.; Tycko, R. *Biochemistry-Us* **2006**, *45*, 498.

(27) Waxman, E. A.; Mazzulli, J. R.; Giasson, B. I. *Biochemistry-Us* **2009**, *48*, 9427.

(28) Davies, P.; Brown, D. R. *Biochem J* **2008**, *410*, 237.

(29) Mehta, A. K.; Lu, K.; Childers, W. S.; Liang, Y.; Dublin, S. N.; Dong, J. J.; Snyder, J. P.; Pingali, S. V.; Thiyagarajan, P.; Lynn, D. G. *J Am Chem Soc* **2008**, *130*, 9829.

(30) Petkova, A. T.; Ishii, Y.; Balbach, J. J.; Antzutkin, O. N.; Leapman, R. D.; Delaglio, F.; Tycko, R. *P Natl Acad Sci USA* **2002**, *99*, 16742.

(31) Paravastu, A. K.; Qahwash, I.; Leapman, R. D.; Meredith, S. C.; Tycko, R. *P Natl Acad Sci USA* **2009**, *106*, 7443.

(32) Balbach, J. J.; Ishii, Y.; Antzutkin, O. N.; Leapman, R. D.; Rizzo, N. W.; Dyda, F.; Reed, J.; Tycko, R. *Biochemistry-Us* **2000**, *39*, 13748.

(33) Lambert, M. P.; Barlow, A. K.; Chromy, B. A.; Edwards, C.; Freed, R.; Liosatos, M.; Morgan, T. E.; Rozovsky, I.; Trommer, B.; Viola, K. L.; Wals, P.; Zhang, C.; Finch, C. E.; Krafft, G. A.; Klein, W. L. *P Natl Acad Sci USA* **1998**, *95*, 6448.

(34) Vigopelfrey, C.; Lee, D.; Keim, P.; Lieberburg, I.; Schenk, D. B. *J Neurochem* **1993**, *61*, 1965.

(35) Bush, A. I. *Alz Dis Assoc Dis* **2003**, *17*, 147.

(36) Morgan, D. M.; Dong, J. J.; Jacob, J.; Lu, K.; Apkarian, R. P.; Thiyagarajan, P.; Lynn, D. G. *J Am Chem Soc* **2002**, *124*, 12644.

(37) Lovell, M. A.; Robertson, J. D.; Teesdale, W. J.; Campbell, J. L.; Markesbery, W. R. *J Neurol Sci* **1998**, *158*, 47.

(38) Dong, J.; Canfield, J. M.; Mehta, A. K.; Shokes, J. E.; Tian, B.; Childers, W. S.; Simmons, J. A.; Mao, Z.; Scott, R. A.; Warncke, K.; Lynn, D. G. *P Natl Acad Sci USA* **2007**, *104*, 13313.

(39) Dong, J. J.; Shokes, J. E.; Scott, R. A.; Lynn, D. G. *J Am Chem Soc* **2006**, *128*, 3540.

(40) Hou, L. M.; Zagorski, M. G. *J Am Chem Soc* **2006**, *128*, 9260.

(41) Kowalik-Jankowska, T.; Ruta-Dolejsz, M.; Wisniewska, K.; Lankiewicz, L.; Kozlowski, H. *Environ Health Persp* **2002**, *110*, 869.

(42) Cherny, R. A.; Legg, J. T.; McLean, C. A.; Fairlie, D. P.; Huang, X. D.; Atwood, C. S.; Beyreuther, K.; Tanzi, R. E.; Masters, C. L.; Bush, A. I. *J Biol Chem* **1999**, *274*, 23223.

(43) Karr, J. W.; Kaupp, L. J.; Szalai, V. A. *J Am Chem Soc* **2004**, *126*, 13534.

(44) Curtain, C. C.; Ali, F.; Volitakis, I.; Cherny, R. A.; Norton, R. S.; Beyreuther, K.; Barrow, C. J.; Masters, C. L.; Bush, A. I.; Barnham, K. J. *J Biol Chem* **2001**, *276*, 20466.

(45) Caragounis, A.; Du, T.; Fi, G. F.; Laughton, K. M.; Volitakis, I.; Sharples, R. A.; Cherny, R. A.; Masters, C. L.; Drew, S. C.; Hill, A. F.; Li, Q. X.; Crouch, P. J.; Barnham, K. J.; White, A. R. *Biochem J* **2007**, *407*, 435.

(46) Drew, S. C.; Noble, C. J.; Masters, C. L.; Hanson, G. R.; Barnham, K. J. *J Am Chem Soc* **2009**, *131*, 1195.

(47) Balbach, J. J.; Petkova, A. T.; Oyler, N. A.; Antzutkin, O. N.; Gordon, D. J.; Meredith, S. C.; Tycko, R. *Biophys J* **2002**, *83*, 1205.

(48) Ma, Q. F.; Hu, J.; Wu, W. H.; Liu, H. D.; Du, J. T.; Fu, Y.; Wu, Y. W.; Lei, P.; Zhao, Y. F.; Li, Y. M. *Biopolymers* **2006**, *83*, 20.

(49) Atwood, C. S.; Obrenovich, M. E.; Liu, T. B.; Chan, H.; Perry, G.; Smith, M. A.; Martins, R. N. *Brain Res Rev* **2003**, *43*, 1.

(50) Stellato, F.; Menestrina, G.; Dalla Serra, M.; Potrich, C.; Tomazzolli, R.; Meyer-Klaucke, W.; Morante, S. *Eur Biophys J Biophy* **2006**, *35*, 340.

(51) Dong, J.; Atwood, C. S.; Anderson, V. E.; Siedlak, S. L.; Smith, M. A.; Perry, G.; Carey, P. R. *Biochemistry-Us* **2003**, *42*, 2768.

(52) Faller, P.; Hureau, C. *Dalton T* **2009**, 1080.

(53) Zou, J.; Kajita, K.; Sugimoto, N. *Angew Chem Int Edit* **2001**, *40*, 2274.

(54) Zou, J.; Sugimoto, N. *J Chem Soc Perk T 2* **2000**, 2135.

(55) Atwood, C. S.; Perry, G.; Zeng, H.; Kato, Y.; Jones, W. D.; Ling, K. Q.; Huang, X. D.; Moir, R. D.; Wang, D. D.; Sayre, L. M.; Smith, M. A.; Chen, S. G.; Bush, A. I. *Biochemistry-Us* **2004**, *43*, 560.

(56) Tickler, A. K.; Smith, D. G.; Ciccotosto, G. D.; Tew, D. J.; Curtain, C. C.; Carrington, D.; Masters, C. L.; Bush, A. I.; Cherny, R. A.; Cappai, R.; Wade, J. D.; Barnham, K. J. *J Biol Chem* **2005**, *280*, 13355.

(57) Karr, J. W.; Szalai, V. A. *J Am Chem Soc* **2007**, *129*, 3796.

(58) Karr, J. W.; Szalai, V. A. *Biochemistry-Us* **2008**, *47*, 5006.

(59) Zavoisky, E. *J Phys-Ussr* **1944**, *8*, 377.

(60) Blumberg, W. E.; Peisach, J. *Arch Biochem Biophys* **1974**, *162*, 502.

(61) Peisach, J.; Mims, W. B.; Graziani, M. T.; Mondovi, B. *Biophys J* **1977**, *17*, A58.

(62) Sykes, A. G. *Adv Inorg Chem Rad* **1991**, *36*, 377.

(63) Karr, J. W.; Akintoye, H.; Kaupp, L. J.; Szalai, V. A. *Biochemistry-Us* **2005**, *44*, 5478.

(64) Wertz, J. E.; Bolton, J. R. *Electron spin resonance : elementary theory and practical applications*; Chapman and Hall: New York, 1986.

(65) Slichter, C. P. *Principles of magnetic resonance*; 3rd enl. and updated ed.; Springer-Verlag: Berlin ; New York, 1990.

(66) Colaneri, M. J.; Potenza, J. A.; Schugar, H. J.; Peisach, J. *J Am Chem Soc* **1990**, *112*, 9451.

(67) Que, L. *Physical methods in bioinorganic chemistry : spectroscopy and magnetism*; University Science Books: Sausalito, Calif., 2000.

(68) Lippard, S. J.; Berg, J. M. *Principles of bioinorganic chemistry*; University Science Books: Mill Valley, Calif., 1994.

(69) Weltner, W. *Magnetic atoms and molecules*; Scientific and Academic Editions: New York, 1983.

(70) Spiro, T. G. *Copper proteins*; Wiley: New York, 1981.

(71) Dikanov, S. A.; Tsvetkov, Y. D. *Electron spin echo envelope modulation (ESEEM) spectroscopy*; CRC Press: Boca Raton, 1992.
(72) Schweiger, A.; Jeschke, G. *Principles of pulse electron paramagnetic resonance*; Oxford University Press: Oxford, UK ; New York, 2001.
(73) Blumberg, W. E.; Mims, W. B.; Zuckerma.D *Rev Sci Instrum* **1973**, *44*, 546.
(74) Hoff, A. J. *Advanced EPR : applications in biology and biochemistry*; Elsevier ;
Distributors for the U.S. and Canada, Elsevier Science Pub. Co.: Amsterdam ; New York New York, NY, U.S.A., 1989.
(75) Karlin, K. D.; Tyeklár, Z. *Bioinorganic chemistry of copper*; Chapman & Hall: New York, 1993.
(76) Shulman, R. G. *Biological applications of magnetic resonance*; Academic Press: New York, 1979.
(77) Mims, W. B.; Peisach, J. *Biochemistry-Us* **1976**, *15*, 3863.
(78) Mims, W. B.; Peisach, J. *J Biol Chem* **1979**, *254*, 4321.
(79) Mims, W. B.; Peisach, J.; Shaw, R. W.; Beinert, H. *J Biol Chem* **1980**, *255*, 6843.
(80) Kosman, D. J.; Peisach, J.; Mims, W. B. *Biochemistry-Us* **1980**, *19*, 1304.
(81) Mccracken, J.; Pember, S.; Benkovic, S. J.; Villafranca, J. J.; Miller, R. J.; Peisach, J. *J Am Chem Soc* **1988**, *110*, 1069.
(82) Jiang, F.; Mccracken, J.; Peisach, J. *J Am Chem Soc* **1990**, *112*, 9035.
(83) Mims, W. B.; Peisach, J. *J Chem Phys* **1978**, *69*, 4921.
(84) Rowan, L. G.; Hahn, E. L.; Mims, W. B. *Phys Rev* **1965**, *137*, A61.
(85) Mims, W. B. *Phys Rev B* **1972**, *5*, 2409.
(86) Mims, W. B. *Phys Rev B* **1972**, *6*, 3543.
(87) Peisach, J. *Fed Proc* **1981**, *40*, 1857.
(88) Flanagan, H. L.; Singel, D. J. *J Chem Phys* **1987**, *87*, 5606.
(89) Ohba, Y.; Yoshida, Y.; Iwaizumi, M. *Appl Magn Reson* **1994**, *6*, 107.
(90) Jiang, F.; Peisach, J. *Inorg Chem* **1994**, *33*, 1348.
(91) Cornelius, J. B.; Mccracken, J.; Clarkson, R. B.; Belford, R. L.; Peisach, J. *J Phys Chem-Us* **1990**, *94*, 6977.
(92) Colaneri, M. J.; Peisach, J. *J Am Chem Soc* **1992**, *114*, 5335.
(93) Colaneri, M. J.; Peisach, J. *J Am Chem Soc* **1995**, *117*, 6308.
(94) Feng, J.; Karlin, K. D.; Peisach, J. *Inorg Chem* **1993**, *32*, 2576.
(95) Goldfarb, D.; Fauth, J. M.; Tor, Y.; Shanzer, A. *J Am Chem Soc* **1991**, *113*, 1941.
(96) Zhang, C. G.; Duan, C. Y.; Hu, Q.; Yan, D. Y. *J Chem Crystallogr* **1999**, *29*, 1153.
(97) Abuhijleh, A. L.; Woods, C.; Ahmed, I. Y. *Inorg Chim Acta* **1991**, *190*, 11.
(98) Iwatsubo, T.; Odaka, A.; Suzuki, N.; Mizusawa, H.; Nukina, N.; Ihara, Y. *Neuron* **1994**, *13*, 45.
(99) Castano, E. M.; Prelli, F.; Soto, C.; Beavis, R.; Matsubara, E.; Shoji, M.; Frangione, B. *J Biol Chem* **1996**, *271*, 32185.

(100) Morgan, D. M.; Lakdawala, A.; Snyder, J. P.; Liotta, D. C.; Lynn, D. G. *Abstr Pap Am Chem S* **2002**, *223*, C21.

(101) Makin, O. S.; Serpell, L. C. *Febs J* **2005**, *272*, 5950.

(102) Petkova, A. T.; Leapman, R. D.; Guo, Z. H.; Yau, W. M.; Mattson, M. P.; Tycko, R. *Science* **2005**, *307*, 262.

(103) Damante, C. A.; Osz, K.; Nagy, Z.; Papalardo, G.; Grasso, G.; Impellizzeri, G.; Rizzarelli, E.; Sovago, I. *Inorg Chem* **2008**, *47*, 9669.

(104) Gaggelli, E.; Kozlowski, H.; Valensin, D.; Valensin, G. *Chem Rev* **2006**, *106*, 1995.

(105) Kowalik-Jankowska, T.; Ruta, M.; Wisniewska, K.; Lankiewicz, L. *J Inorg Biochem* **2003**, *95*, 270.

(106) Selkoe, D. J. *Science* **2002**, *298*, 789.

(107) Mantyh, P. W.; Ghilardi, J. R.; Rogers, S.; Demaster, E.; Allen, C. J.; Stimson, E. R.; Maggio, J. E. *J. Neurochem.* **1993**, *61*, 1171.

(108) Bush, A. I.; Pettingell, W. H.; Multhaup, G.; Paradis, M. D.; Vonsattel, J. P.; Gusella, J. F.; Beyreuther, K.; Masters, C. L.; Tanzi, R. E. *Science* **1994**, *265*, 1464.

(109) Allsop, D.; Mayes, J.; Moore, S.; Masad, A.; Tabner, B. J. *Biochem. Soc. Trans.* **2008**, *36*, 1293.

(110) Brown, D. R.; Hafiz, F.; Glasssmith, L. L.; Wong, B. S.; Jones, I. M.; Clive, C.; Haswell, S. J. *Embo Journal* **2000**, *19*, 1180.

(111) Chattopadhyay, M.; Walter, E. D.; Newell, D. J.; Jackson, P. J.; Aronoff-Spencer, E.; Peisach, J.; Gerfen, G. J.; Bennett, B.; Antholine, W. E.; Millhauser, G. L. *J. Am. Chem. Soc.* **2005**, *127*, 12647.

(112) Riihimaki, E. S.; Martinez, J. M.; Kloo, L. *Phys. Chem. Chem. Phys.* **2008**, *10*, 2488.

(113) Rasia, R. M.; Bertoncini, C. W.; Marsh, D.; Hoyer, W.; Cherny, D.; Zweckstetter, M.; Griesinger, C.; Jovin, T. M.; Fernandez, C. O. *Proc. Natl. Acad. Sci. U.S.A.* **2005**, *102*, 4294.

(114) Binolfi, A.; Lamberto, G. R.; Duran, R.; Quintanar, L.; Bertoncini, C. W.; Souza, J. M.; Cervenansky, C.; Zweckstetter, M.; Griesinger, C.; Fernandez, C. O. *J. Am. Chem. Soc.* **2008**, *130*, 11801.

(115) Dong, J.; Canfield, J. M.; Mehta, A. K.; Shokes, J. E.; Tian, B.; Childers, W. S.; Simmons, J. A.; Mao, Z.; Scott, R. A.; Warncke, K.; Lynn, D. G. *Proc. Natl. Acad. Sci. U.S.A.* **2007**, *104*, 13313.

(116) Atwood, C. S.; Moir, R. D.; Huang, X. D.; Scarpa, R. C.; Bacarra, N. M. E.; Romano, D. M.; Hartshorn, M. K.; Tanzi, R. E.; Bush, A. I. *J Biol Chem* **1998**, *273*, 12817.

(117) Syme, C. D.; Nadal, R. C.; Rigby, S. E. J.; Viles, J. H. *J Biol Chem* **2004**, *279*, 18169.

(118) Smith, D. P.; Smith, D. G.; Curtain, C. C.; Boas, J. F.; Pilbrow, J. R.; Ciccotosto, G. D.; Lau, T. L.; Tew, D. J.; Perez, K.; Wade, J. D.; Bush, A. I.; Drew, S. C.; Separovic, F.; Masters, C. L.; Cappai, R.; Barnham, K. J. *J Biol Chem* **2006**, *281*, 15145.

(119) Kevan, L.; Bowman, M. K. *Modern pulsed and continuous-wave electron spin resonance*; Wiley: New York, 1990.

(120) Schweiger, A. *Angew. Chem., Int. Ed. Engl.* **1991**, *30*, 265.

(121) PasenkiewiczGierula, M.; Subczynski, W. K.; Antholine, W. E. *J. Phys. Chem. B* **1997**, *101*, 5596.

(122) Mccracken, J.; Pember, S.; Benkovic, S. J.; Villafranca, J. J.; Miller, R. J.; Peisach, J. *J. Am. Chem. Soc.* **1988**, *110*, 1069.

(123) Mims, W. B.; Peisach, J. *J. Chem. Phys.* **1978**, *69*, 4921.

(124) Flanagan, H. L.; Singel, D. J. *J. Chem. Phys.* **1987**, *87*, 5606.

(125) Peisach, J.; Mims, W. B.; Davis, J. L. *J. Biol. Chem.* **1979**, *254*, 2379.

(126) Sun, L.; Hernandez-Guzman, J.; Warncke, K. *J. Magn. Reson.* **2009** doi:10.1016/j.jmr.2009.05.012.

(127) Mims, W. B. *Phys. Rev. B* **1972**, *5*, 2409.

(128) Wertz, J. E.; Bolton, J. R. *Electron spin resonance; elementary theory and practical applications*; McGraw-Hill: New York, 1972.

(129) Lucken, E. A. C. *Nuclear quadrupole coupling constants*; Academic P.: London, New York, 1969.

(130) Mims, W. B. *Phys. Rev. B* **1972**, *6*, 3543.

(131) Stoll, S.; Schweiger, A. *J. Magn. Reson.* **2003**, *163*, 248.

(132) Reijerse, E. J.; Tyryshkin, A. M.; Dikanov, S. A. *J. Magn. Reson.* **1998**, *131*, 295.

(133) Dikanov, S. A.; Shubin, A. A.; Parmon, V. N. *J. Magn. Reson.* **1981**, *42*, 474.

(134) Colaneri, M. J.; Peisach, J. *J. Am. Chem. Soc.* **1992**, *114*, 5335.

(135) Colaneri, M. J.; Peisach, J. *J. Am. Chem. Soc.* **1995**, *117*, 6308.

(136) Colaneri, M. J.; Potenza, J. A.; Schugar, H. J.; Peisach, J. *J. Am. Chem. Soc.* **1990**, *112*, 9451.

(137) Zhang, C. G.; Duan, C. Y.; Hu, Q.; Yan, D. Y. *J. Chem. Crystallogr.* **1999**, *29*, 1153.

(138) Abuhijleh, A. L.; Woods, C.; Ahmed, I. Y. *Inorg. Chim. Acta* **1991**, *190*, 11.

(139) Hathaway, B. J.; Billing, D. E. *Coordin Chem Rev* **1970**, *5*, 143.

(140) Flanagan, H. L.; Gerfen, G. J.; Lai, A.; Singel, D. J. *J Chem Phys* **1988**, *88*, 2162.

(141) Mims, W. B.; Peisach, J.; Davis, J. L. *J Chem Phys* **1977**, *66*, 5536.

(142) Baute, D.; Arieli, D.; Neese, F.; Zimmermann, H.; Weckhuysen, B. M.; Goldfarb, D. *J Am Chem Soc* **2004**, *126*, 11733.

(143) Warncke, K.; Mccracken, J. *J Chem Phys* **1994**, *101*, 1832.

(144) Huang, X. D.; Cuajungco, M. P.; Atwood, C. S.; Hartshorn, M. A.; Tyndall, J. D. A.; Hanson, G. R.; Stokes, K. C.; Leopold, M.; Multhaup, G.; Goldstein, L. E.; Scarpa, R. C.; Saunders, A. J.; Lim, J.; Moir, R. D.; Glabe, C.; Bowden, E. F.; Masters, C. L.; Fairlie, D. P.; Tanzi, R. E.; Bush, A. I. *J Biol Chem* **1999**, *274*, 37111.

(145) Yoshiike, Y.; Tanemura, K.; Murayama, O.; Akagi, T.; Murayama, M.; Sato, S.; Sun, X. Y.; Tanaka, N.; Takashima, A. *J Biol Chem* **2001**, *276*, 32293.

(146) Zou, K.; Gong, J. S.; Yanagisawa, K.; Michikawa, M. *J Neurosci* **2002**, *22*, 4833.

(147) Simmons, L. K.; May, P. C.; Tomaselli, K. J.; Rydel, R. E.; Fuson, K. S.; Brigham, E. F.; Wright, S.; Lieberburg, I.; Becker, G. W.; Brems, D. N.; Li, W. Y. *Mol Pharmacol* **1994**, *45*, 373.

(148) Kirkitadze, M. D.; Bitan, G.; Teplow, D. B. *J Neurosci Res* **2002**, *69*, 567.
(149) Shin, B. K.; Saxena, S. *Biochemistry-Us* **2008**, *47*, 9117.
(150) Jun, S.; Saxena, S. *Angew Chem Int Edit* **2007**, *46*, 5263.
(151) Peisach, J.; Blumberg, W. E. *Arch Biochem Biophys* **1974**, *165*, 691.
(152) Jun, S.; Gillespie, J. R.; Shin, B. K.; Saxena, S. *Biochemistry-Us* **2009**, *48*, 10724.
(153) Lu, K.; Jacob, J.; Thiyagarajan, P.; Conticello, V. P.; Lynn, D. G. *J Am Chem Soc* **2003**, *125*, 6391.
(154) Bush, A. I. *Neurobiol Aging* **2002**, *23*, 1031.
(155) Atwood, C. S.; Scarpa, R. C.; Huang, X. D.; Moir, R. D.; Jones, W. D.; Fairlie, D. P.; Tanzi, R. E.; Bush, A. I. *J Neurochem* **2000**, *75*, 1219.
(156) Shearer, J.; Szalai, V. A. *J Am Chem Soc* **2008**, *130*, 17826.
(157) Dorlet, P.; Gambarelli, S.; Faller, P.; Hureau, C. *Angew Chem Int Edit* **2009**, *48*, 9273.
(158) Miura, T.; Suzuki, K.; Kohata, N.; Takeuchi, H. *Biochemistry-Us* **2000**, *39*, 7024.
(159) Damante, C.; Osz, K.; Nagy, Z.; Pappalardo, G.; Grasso, G.; Impellizzeri, G.; Rizzarelli, E.; Sovago, I. *J Pept Sci* **2008**, *14*, 87.
(160) Guilloreau, L.; Damian, L.; Coppel, Y.; Mazarguil, H.; Winterhalter, M.; Faller, P. *J Biol Inorg Chem* **2006**, *11*, 1024.
(161) Corrada, M. M.; Brookmeyer, R.; Paganini-Hill, A.; Berlau, D.; Kawas, C. H. *Ann Neurol* **2010**, *67*, 114.
(162) Sun, L.; Hernandez-Guzman, J.; Warncke, K. *J Magn Reson* **2009**, *200*, 21.
(163) Kowalik-Jankowska, T.; Ruta-Dolejsz, M.; Wisniewska, K.; Lankiewicz, L.; Kozlowski, H. *J Chem Soc Dalton* **2000**, 4511.
(164) Kowalik-Jankowska, T.; Ruta-Dolejsz, M.; Wisniewska, K.; Lankiewicz, L. *J Inorg Biochem* **2001**, *86*, 535.
(165) Kowalik-Jankowska, T.; Ruta-Dolejsz, M.; Wisniewska, K.; Lankiewicz, L. *J Inorg Biochem* **2002**, *92*, 1.